



Dissertation

Yefei Yin

New generation of quantum Hall resistance standards based on *n*- and *p*-type epitaxial graphene



ISSN 2941-1297
ISBN 978-3-944659-43-5

DOI 10.7795/110.20250327

Physikalisch-Technische Bundesanstalt

Dissertationen

PTB-Diss-11

Braunschweig, April 2025

Yefei Yin,

New generation of quantum Hall resistance standards based on *n*- and *p*-type epitaxial graphene

ISSN 2941-1297

ISBN 978-3-944659-43-5

DOI 10.7795/110.20250327

Empfohlene Zitierweise/recommended citation

Yin, Y., 2025. *New generation of quantum Hall resistance standards based on n- and p-type epitaxial graphene*. Dissertation, Gottfried Wilhelm Leibniz Universität Hannover. Braunschweig: Physikalisch-Technische Bundesanstalt. PTB-Bericht Diss-11. ISBN 978-3-944659-43-5.
Verfügbar unter: <https://doi.org/10.7795/110.20250327>

Herausgeber:

Physikalisch-Technische Bundesanstalt
ISNI: 0000 0001 2186 1887

Presse und Öffentlichkeitsarbeit

Bundesallee 100
38116 Braunschweig

Telefon: (05 31) 592-93 21
Telefax: (05 31) 592-92 92
www.ptb.de

New generation of quantum Hall resistance standards based on n - and p - type epitaxial graphene

Von der Fakultät für Mathematik und Physik
der Gottfried Wilhelm Leibniz Universität Hannover

zur Erlangung des Grades
Doktor der Naturwissenschaften
— Dr. rer. nat. —

genehmigte Dissertation von

M.Sc. Yefei Yin

2024

Referent Prof. Dr. Rolf J. Haug
Gottfried Wilhelm Leibniz Universität Hannover

Korreferent PD Dr. Hans Werner Schumacher
Physikalisch-Technische Bundesanstalt, Braunschweig

Korreferent Prof. Dr. Christoph Tegenkamp
Technische Universität Chemnitz

Tag der Abgabe 26. 06. 2024

Tag der Promotion 30. 08. 2024

Abstract

Electrical quantum standards, e.g., quantum resistance, current, and voltage, have played a decisive role in modern metrology, particularly since the International System of Units (SI) revision in 2019. The SI unit of electrical resistance, the ohm, is implemented by a quantum Hall resistance (QHR) based on the quantum Hall effect. Furthermore, other SI units, such as the farad, the ampere, and the kilogram (realized by Kibble balance), essentially require QHR standards in their traceability route to realize their SI units. Therefore, QHR standards play an essential role in implementing the new SI. Conventional GaAs heterostructure QHR standards with the quantized resistance value of $R_H = h/2e^2$ (filling factor $\nu = 2$) are operating under the extreme conditions of high magnetic flux density $B > 10$ T, limited current $I < 50$ μ A, and low temperature $T < 1.5$ K. These extreme operating conditions significantly hinder the dissemination of primary resistance standards, let alone the commercialization of quantum resistance standards. Simplifying the operation conditions of QHR standards can shorten the calibration chain from primary resistance standards to the final product, resulting in higher accuracy for the end users in science, technology, and industry. Moreover, the other SI units correlated with the unit ohm can also benefit from the improved QHR standard in their traceability route. Developing a new generation of QHR standards that can operate under relaxed conditions of the lower B (< 6 T), higher I (> 100 μ A), and higher T (≥ 4.2 K) is the cornerstone of the electrical quantum standards.

In the past decade, epitaxial graphene on SiC has emerged as a promising alternative to GaAs heterostructures for primary QHR standards with a 10^{-9} accuracy ($n\Omega/\Omega$) because epitaxial graphene is promising to realize the SI unit of resistance under relaxed conditions of B , I , and T . In this study, large-scale, high-quality single-layer epitaxial graphene is grown on semi-insulating SiC substrates. A simple, efficient, and cost-effective fabrication process based on optical lithography is successfully developed to fabricate twelve identical graphene QHR devices into a centimeter graphene chip. The intrinsic high carrier density of the as-grown epitaxial graphene is reduced and tailored by F4-TCNQ molecular doping. By precisely adjusting the F4-TCNQ dopant concentration, the carrier density is tuned to the desired values spanning from intrinsic n -type to the p -type regimes for developing QHR standards. A physical model in terms of the energy band diagram is established to explain the electron transfer mechanism between the F4-TCNQ and epitaxial graphene/SiC surface.

Furthermore, the *n*- and *p*-type epitaxial graphene is used to successfully develop the primary QHR standards, which can operate under relaxed conditions. The *n*-type graphene QHR standards achieved a high accuracy of less than $2 \text{ n}\Omega/\Omega$ (two parts per billion, $k = 2$) at a moderate magnetic flux density of $B = 4.5 \text{ T}$, high current of $I = 232.5 \text{ }\mu\text{A}$, and easier to access temperature of $T = 4.2 \text{ K}$, simultaneously. To our knowledge, this is the best performance of graphene QHR standards achieved in literature so far. The graphene QHR standards have maintained the $2 \text{ n}\Omega/\Omega$ accuracy in terms of time over 2.5 years, multiple cool-down cycles over fifteen times, and long-distance shipment over 800 km between two metrology institutes. More importantly, this dissertation first systematically demonstrated that *p*-type epitaxial graphene can also be used for primary resistance standards, as accurate (10^{-9} accuracy) as GaAs and *n*-type graphene counterparts for realizing the SI unit ohm in quantum resistance metrology. Furthermore, a contour plot of graphene QHR standards is proposed to reveal the correlation of the quantization regime (10^{-9} accuracy) with magnetic field and carrier density. The contour plots serve to benchmark the graphene QHR device according to end users' specifications. When implemented, graphene QHR standards may lead to broader dissemination of primary resistance standards beyond national metrology institutes, extending to commercial calibration laboratories and industry on-site.

Keywords: epitaxial graphene on SiC, quantum Hall resistance standard, quantum resistance metrology, F4-TCNQ molecular doping, unit of resistance

Table of Contents

Abstract	iii
Table of Contents	v
List of Constants.....	viii
List of Symbols	viii
List of Abbreviations.....	x
Chapter 1. Introduction	1
1.1 The history of graphene	1
1.2 Epitaxial graphene by sublimation growth on SiC.....	4
1.3 QHR standards based on epitaxial graphene on SiC	6
1.4 Contributions and Scope.....	8
Chapter 2. Theory and concepts.....	11
2.1 Crystal and electronic structure	11
2.2 Low-energy spectrum	14
2.3 Magnetotransport in graphene	16
2.3.1 Classical Hall effect	16
2.3.2 Integer Quantum Hall effect	17
2.3.3 Landau level.....	19
Chapter 3. Experimental techniques and instruments.....	23
3.1 Epitaxial graphene growth.....	23
3.1.1 Growth setup.....	23
3.1.2 Polymer-assisted sublimation growth method	25
3.2 Surface characterization techniques	26
3.2.1 Laser scanning confocal microscopy	26
3.2.2 Atomic force microscopy.....	28
3.3 Device fabrication.....	29
3.3.1 Optical Lithography	29

3.3.2 F4-TCNQ molecular doping technique	32
3.4 Magnetotransport measurement at low temperatures	34
3.4.1 Cryogenic and electronic setup	35
3.4.2 Ohmic contact resistance	36
3.4.3 Hall measurements	37
3.5 High-accuracy measurements	37
3.5.1 Principle of current-reversal measurement	37
3.5.2 Principle of the CCC bridge	39
3.5.3 High-accuracy measurements	41
3.5.4 Definition of deviation regime and quantization regime	42
Chapter 4. F4-TCNQ Molecular doping in epitaxial graphene	45
4.1 Introduction	45
4.2 Concentration-dependent F4-TCNQ doped epitaxial graphene	47
4.3 Decisive influence of graphene's initial charge carrier density	51
4.4 Different doping stacks for the molecular doping	53
4.5 Transport scattering mechanism in epitaxial graphene	54
4.5.1 High mobility of epitaxial graphene doped by F4-TCNQ	54
4.5.2 Long-range and short-range scattering in epitaxial graphene	55
4.5.3 Temperature-dependent mobility	57
4.6 Doping model for F4-TCNQ molecular doped epitaxial graphene on SiC	59
4.6.1 Electron wave function and charge density distribution	60
4.6.2 Energy band alignment in graphene/F4-TCNQ charge transfer complex	63
4.6.3 Exclusion of double ionized state F4-TCNQ ⁻² and charge transfer to PMMA	65
Chapter 5. Epitaxial graphene quantum Hall resistance standard	67
5.1 Graphene QHR standards	67
5.2 <i>n</i> -type graphene QHR standards	69
5.2.1 <i>n</i> -type QHR standard with different electron densities	70
5.2.2 <i>n</i> -type QHR standards with different doping stacks	73

5.2.3 Comparison to commercial QHR device	75
5.3 Contour plot of the quantization regime of the <i>n</i> -type graphene QHR standards	77
5.4 <i>p</i> -type graphene QHR standards	80
5.4.1 Magnetotransport of <i>p</i> -type QHR standards	81
5.4.2 High-accuracy measurement of <i>p</i> -type QHR standards.....	83
5.4.3 Contour plot of <i>p</i> -type QHR standards	85
5.5 Temperature-dependent QHE in high magnetic fields	87
Chapter 6. Realization of the unit ohm under relaxed experimental conditions.....	91
6.1 Introduction	91
6.2 Homogeneity of electron density and robustness of graphene QHR standard	93
6.3 Long-term temporal stability of carrier density.....	96
6.4 Long-term temporal stability of $n\Omega/\Omega$ -level quantization.....	98
6.5 Realization of the SI ohm under relaxed conditions of <i>B</i> , <i>I</i> , and <i>T</i> simultaneously	102
6.6 Limits of quantization as a function of electron density	104
6.7 Current-dependent measurement by the current reversal technique	106
6.8 Conclusion	108
Chapter 7. Summary and outlook	109
7.1 Summary.....	109
7.2 Outlook	112
Appendix	117
Bibliography.....	125
Curriculum vitae.....	141
List of Publications.....	143
Acknowledgment	145

List of Constants

e	Elementary charge: $1.602\,176\,634 \times 10^{-19}$ C
h	Planck constant: $6.626\,070\,15 \times 10^{-34}$ J·s
\hbar	Reduced Planck constant: $1.054\,571\,817 \times 10^{-34}$ J·s
k_B	Boltzmann constant: $1.380\,649 \times 10^{-23}$ J/K
m_e	Electron mass: $9.109\,383\,7015 \times 10^{-31}$ kg
R_K	Von Klitzing constant (h/e^2): 25 812.807 459 3045 Ω

List of Symbols

Ψ	Wave function
a	Lattice constant
Φ	Magnetic flux
Φ_0	Magnetic flux quantum
v_F	Fermi velocity
ω_c	Cyclotron frequency
E	Energy
E_F	Fermi level
E_D	Energetic location of Dirac point
E_g	Bandgap
Φ	Work function
I	Current
f	Frequency
ν	Filling factor
μ	Charge carrier mobility
μ_e	Electron mobility
μ_h	Hole mobility
N	Landau level index
n	Charge carrier density
n_s	Two-dimensional sheet carrier density

n_e	Electron density
n_h	Hole density
n_{LL}	Number of localized carriers
R	Resistance
ρ	Resistivity
R_{xx}	Longitudinal resistance
ρ_{xx}	Longitudinal resistivity
R_{xy}	Transverse (Hall) resistance
ρ_{xy}	Transverse (Hall) resistivity
T	Temperature
t	Thickness
t	Time
P	Pressure
B	Magnetic field
m^*	Effective electron mass

List of Abbreviations

2D	Two-dimensional
3D	Three-dimensional
2DEG	Two-dimensional electron gas
AC	Alternating current
AFM	Atomic force microscopy
AlGaAs	Aluminum gallium arsenide
ARPES	Angle-resolved photoelectron spectroscopy
Ar	Argon
BIPM	Bureau International des Poids et Mésures
CCC	Cryogenic current comparator
CIPM	International Committee for Weights and Measures
CVD	Chemical vapor deposition
DC	Direct current
DFT	Density functional theory
DOS	Density of states
F4-TCNQ	2,3,5,6-Tetrafluoro-7,7,8,8-tetracyan-oquino-dimethane
FET	Field effect transistor
GaAs	Gallium arsenide
hBN	Hexagonal boron nitride
He	Helium
IQHE	Integer quantum Hall effect
IUPAC	International Union of Pure and Applied Chemistry
IETS	Inelastic tunnelling spectroscopy
LA	longitudinal acoustic
LDOS	Local density of states
LLs	Landau levels
LSCM	Laser scanning confocal microscopy
LEED	Low-Energy Electron Diffraction
NMI	National metrology institute

N ₂	Nitrogen
PASG	Polymer-assisted sublimation growth
PMMA	Poly-methyl-methacrylate
PTB	Physikalisch-Technische Bundesanstalt
QAHE	Quantum anomalous Hall effect
QHE	Quantum Hall effect
QHR	Quantum Hall resistance
RIP	Remotely interfacial phonon
RT	Room temperature (≈ 20 °C)
SdH	Shubnikov de Haas oscillation
SEM	Scanning electron microscopy
SiC	Silicon carbide
SQUID	Superconducting Quantum Interference Device
STM	Scanning tunneling microscopy
TEM	Transmission electron microscopy
VTI	Variable temperature insert

Chapter 1. Introduction

1.1 The history of graphene

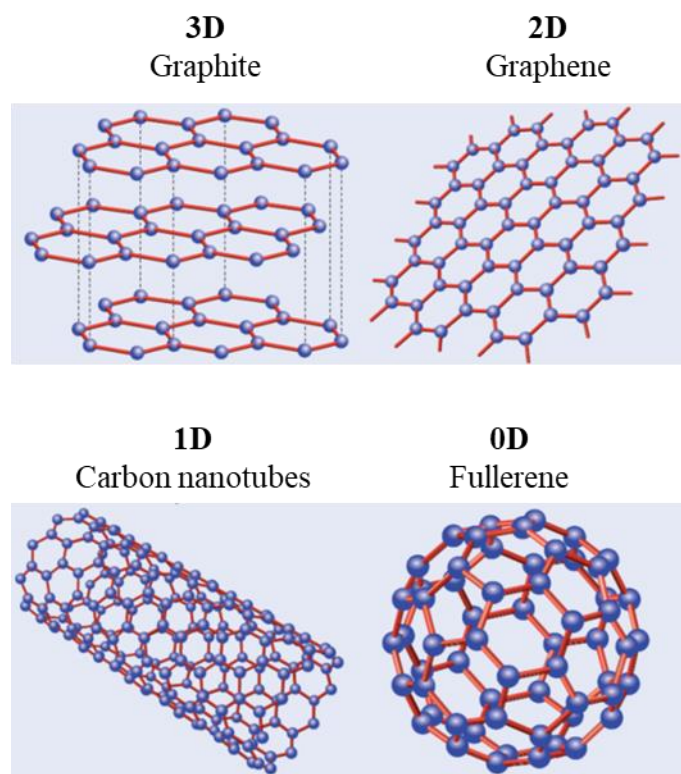


Figure 1.1 Graphite (top left) can be viewed as a stack of graphene layers. Graphene (top right) is a honeycomb lattice of carbon atoms. Carbon nanotubes (bottom left) are rolled-up cylinders of graphene. Fullerenes (C₆₀) (bottom right) are molecules consisting of wrapped graphene by introducing pentagons on the hexagonal lattice. Adapted from Ref. [1]

Graphene is a thin, two-dimensional (2D) material consisting of a single atomic layer of carbon atoms arranged in a hexagonal lattice. It is the basic building block of many other carbon-based materials, including graphite, carbon nanotubes, and fullerenes, as presented in Figure 1.1. Graphite, commonly found in pencils, is simply a stack of graphene layers. Carbon nanotubes are made of rolled-up sheets of graphene. Buckminsterfullerene molecules, also known as “buckyballs”, are nanometer-size spheres of wrapped-up graphene. These forms of carbon were isolated long before the discovery of graphene and have been used in many applications, but their electric, magnetic, and elastic properties all originate from the properties of graphene. Graphene is a 2D crystal with exceptional properties. It is a million times thinner than paper,

more robust than diamond, and more conductive than copper. Its properties include high optical transparency, high electric and thermal conductivity, high mechanical strength, single-molecule gas detection sensitivity, and high electron mobility. In addition, it is also transparent, flexible, and impermeable to gases and liquids. Graphene has a wide range of potential applications in electronics, energy storage, composite materials, and biomedical engineering. [2]

Historically, the term “graphene” has its origins in the Greek word *graphein*, meaning “to write”. This was one of the earliest documented uses of the term “graphene”. In 1800, the German chemist A. G. Wagner referred to the bulk material in pencils using the term “graphite”. [3] Since 1986, a precise definition of this material has been available. In 1997, the International Union of Pure and Applied Chemistry (IUPAC) formalized these definitions by incorporating them into their Compendium of Chemical Technology. [3]

In 2004, Andre Geim and Konstantin Novoselov at the University of Manchester isolated graphene using a method called mechanical exfoliation. They peeled off a single layer of graphene from bulk graphite using sticky tape. Due to their contribution to the isolation and observation of graphene, and more importantly, the discovery of its unique electronic properties and groundbreaking experiments regarding single-atom-thick 2D material, Andre Geim and Konstantin Novoselov were awarded the Nobel Prize in Physics in 2010. Since then, graphene has attracted significant attention due to its unique properties mentioned above. [4] It is a semi-metal with linear energy dispersion around the Dirac point due to its 2D honeycomb structure, which causes the material to behave differently from conventional semiconductors. [4,5] The discovery of graphene was a significant milestone in the field of materials science. It has opened new avenues for revolutionary applications, such as radio-frequency devices [6], gas sensors [7], and high-accuracy metrology [8].

In 1840, the German scientist Schafhaeutl decoupled individual flakes of graphite through intercalation and exfoliation for the first time. Extraordinary electrical properties were observed in these flakes. [3,9,10] In 1859, English chemist Benjamin Collins Brodie recognized the highly layered nature of thermally reduced graphite oxide. [11] The structure of graphite was identified in 1916 [12] by the related method of powder diffraction. [13,14] The properties of graphite oxide were studied in detail by Kohlschütter and Haenni in 1918. [15] Its structure was determined from single-crystal diffraction in 1924. [16] Since the observation of the graphite multilayer structure in experiments, scientists have attempted to fabricate monolayer graphite, which was later called graphene.

The epitaxial growth of ultrathin graphitic films and a few layers of graphene have been reported since 1970. The earliest efforts to fabricate a few layers of graphite date back to 1970 when John Grant reported graphitic films on Ru and Rh and Blakely et al on Ni. [17] In 1975, Lang et al. produced mono- and multi-layered graphite by thermal decomposition of carbon on single-crystal Pt substrates. [18] In 1975, van Bommel et al. sublimated silicon atoms from silicon carbide (SiC (0001)) crystal in high vacuum at elevated temperature to form thin sheets of graphene. [19] In 2004, Geim and Novoselov successfully obtained single-atom-thick carbon sheets from highly ordered graphite through a micromechanical exfoliation process. [5,16] Since then, extensive research on graphene has taken place.

A starting point for understanding the electronic properties of three-dimensional (3D) graphite was found by P.R. Wallace in 1947. He explored the theory of graphene, predicted the electronic structure, and noted the linear dispersion relation. [20] In 1984 Gordon W. Semenoff, David DiVincenzo, and Eugene J. Mele first pointed out the emergent massless Dirac equation. [21]

Nowadays, three main methods have been developed for fabricating monolayer and multilayer graphene: mechanical/chemical exfoliation, chemical vapor deposition (CVD), and sublimation of SiC. The mechanical exfoliation of graphene is a repeated peeling process. This method was invented by Andre Geim and Konstantin Novoselov. This method extracted a few atom-thick graphite in 2004 [16], and successfully obtained a single graphene sheet by scratching the graphite surface with sticky tape in 2005 [5]. Mechanical exfoliation can only produce graphene flakes that are approximately 10 - 100 μm in size, which is suitable only for fundamental laboratory research and not large enough for industrial purposes. The chemical exfoliation can be introduced as a two-stage process: the first stage is increasing the space between layers in graphite, which reduces the interlayer van der Waals forces. This can be done by intercalating graphite to create graphite-intercalated compounds. [22] In the second stage, these graphite-intercalated compounds are exfoliated to a single- or few-layer graphene by ultra-sonication or rapid heating and finally transferred to another substrate. Chemical exfoliation is a promising method for synthesizing large-scale graphene, but the structure may have many defects due to the oxidation and reduction processes.

An alternative technique for synthesizing graphene is CVD on transition metal substrates, such as Cu, Ni, Pd, Au, or Ru. [23,24] The first report on few-layer graphene synthesized by CVD was published in 2006. [25] This method is based on the saturation of transition metal by carbon in a hydrocarbon gas at high temperatures. In this process, the metal substrate acts as a reaction catalyst and determines the deposition mechanism of graphene, which influences the graphene

quality. Since acid solutions can etch some of the transition metals, graphene on these materials can be transferred to other substrates. This method offers the advantage of synthesizing large-scale graphene domains, but it requires transfer to an insulating substrate, which inevitably introduces defects in graphene.

Therefore, it is necessary to find a method to fabricate large-scale, low-defect-density graphene films directly on an insulating substrate for electronic application.

1.2 Epitaxial graphene by sublimation growth on SiC

Epitaxial graphene is graphene that spontaneously forms on silicon carbide (SiC) crystals when silicon sublimates from the surface at high temperature, resulting in a carbon-rich surface that recrystallizes into graphene. The method of sublimation growth on SiC is growing graphene on semi-insulating SiC substrates using a process called epitaxy, which offers several advantages over the other methods. For instance, epitaxial graphene can be grown in high-quality large-area sheets that are free from defects and impurities, making it an ideal material for use in electronic and optoelectronic devices. In addition, epitaxial graphene is a cost-effective option. Epitaxial graphene can be grown using a relatively simple and cost-effective process, unlike other forms of graphene, such as exfoliated graphene. Moreover, large-scale graphene on a semi-insulating SiC substrate allows for the integration of many devices on one graphene chip, and the device fabrication process is compatible with the existing SiC technology, which enables the scalable development of graphene electronics.

In recent years, research on epitaxial graphene has rapidly expanded. It is now considered to be one of the most promising materials for use in next-generation electronics, optoelectronics, and energy storage. Therefore, there is a growing interest in developing new methods for growing epitaxial graphene, as well as in the study of its properties and potential applications.

The idea of synthesizing graphene by thermal decomposition SiC is inspired by the investigation of single crystal SiC growth. In 1970, Tairov and Tzvetkov established a modified seeded sublimation growth process for the development of 6H-SiC, which was a breakthrough for SiC growth. [26,27] This process is also known as the modified Lely process. During that time, the the sublimation growth was focused on the synthetizations of SiC, rather than graphene. Inspired by the principles of the sublimation growth of SiC, the sublimation growth of graphene from single crystals of SiC(0001) was developed.

Epitaxial growth on insulating substrates was first demonstrated by van Bommel et al., a group from the Netherlands. In 1975, van Bommel et al. reported the observation of the SiC(0001) surface. At an elevated temperature of 1500 °C in an ultrahigh vacuum (UHV < 10⁻¹⁰ Torr), a “graphite pattern” became visible (note: in 1975, the name of graphene was not defined yet). The monolayer flakes of carbon were consistent with the structure of graphene obtained, as determined by Low-energy Electron Diffraction (LEED) and Auger electron spectroscopy. [14] In addition, Chuhei Oshima (1993) found other carbides allowing for graphene growth, such as TiC. [28] Before 2004, the grown films were usually analyzed using surface science techniques that did not provide information about the continuity and quality of the entire graphene film.

In 2009, Emtsev et al. demonstrated the growth of epitaxial graphene in an argon (Ar) atmosphere close to atmospheric pressure synthesized large scale (3 μm wide and 50 μm long) monolayer graphene strips on the periodic terraces of an insulating SiC substrate. [29] This method can grow large-scale, low-defect-density graphene films directly on an insulating SiC substrate for electronic device fabrication. Nowadays, graphene growth by SiC sublimation is typically performed in a furnace with an Ar to improve the uniformity of the epitaxial graphene layer. Epitaxial graphene on SiC has several advantages, including not requiring transfer for device processing and the ability to have a graphene sheet as large as the substrate up to the centimeter scale. SiC is a polar material with two inequivalent terminations, the Si face corresponding to the (0001) polar surface and the C face (000 $\bar{1}$). The growth mechanism of graphene layers on both faces is driven by the sublimation of Si at elevated temperatures, which occurs at a much faster rate of C face due to its higher vapor pressure. [30] The surface reconstructions and growth kinetics of Si and C faces are different, resulting in different graphene growth rates, growth morphologies, and electronic properties. [14,31]

The first attempt to perform magnetotransport in ultrathin epitaxial graphite on SiC was reported by Walt A. de Heer’s group in 2004. [32] In this paper, three layers of epitaxial graphene were obtained on a 6H-SiC substrate. The transport measurement exhibited an electron mobility up to 1100 cm²/Vs and nascent Shubnikov–de Haas oscillations. In the same year, Geim and Novoselov performed magnetotransport measurement in a few layers of graphene by exfoliated method. [16]

1.3 QHR standards based on epitaxial graphene on SiC

The quantum Hall effect (QHE) was discovered in 1980 when Klaus von Klitzing was investigating the transport properties of a Si-MOSFET device at a very low temperature and high magnetic field in Grenoble [33]. It is a macroscopic quantum phenomenon [34], in which the Hall resistance R_{xy} of a two-dimensional electron gas (2DEG) is quantized in high magnetic fields and cryogenic temperatures. The quantized Hall resistance is equal to $h/(ve^2)$ in theory, where ν is an integer known as the filling factor. The QHE thus provides an invariant reference for electrical resistance linked to two natural constants. It sparked an immediate interest in the metrological community.

Nowadays, the quantum Hall effect (QHE) is a cornerstone in the realization of the new *Système international d'unités* (International System of Units, SI). The practical realization of the ohm is carried out using a quantum Hall resistance (QHR) standard operated at $\nu = 2$, delivering $R_H = h/(2e^2)$. Improving the accessibility of QHR standards and simplifying their use can significantly improve the traceability of the primary resistance standard, the ohm, in both direct and alternating current regimes. Other SI units, such as the farad [35,36], the ampere [37,38], and the kilogram (via Kibble balance experiments) [39] essentially require the QHR standards in their traceability route to realize its SI units. High-performance QHR standards, capable of achieving an accuracy of 10^{-9} in lower magnetic fields and higher currents, are thus of great interest for the widespread and robust implementation of the new SI.

So far, conventional QHR standards utilized in many NMIs since the 1990s are based on Gallium-Arsenide (GaAs) heterostructures. These standards permit the implementation of the unit of resistance with an uncertainty of 1 n Ω/Ω or below, but only at high magnetic fields (usually around $B = 10$ T), ultra-low temperatures ($T < 1.5$ K) and limited current levels (typically, $I < 50$ μ A.). [40,41]

In 2005, two groups, A. K. Geim's group at the University of Manchester [5] and P. Kim's group at Columbia University [42], simultaneously observed the QHE in a single layer of exfoliated graphene. Graphene, a truly 2D material, provided another option to implement QHR standards for resistance metrology. The unique band structure of this semi-metal has both practical and fundamental implications. Due to the massless nature of charge carriers in graphene, the energy gap between the first two Landau levels is much more significant than that in semiconductor materials in a high magnetic field. The QHE in graphene can be observed at a much lower magnetic field and/or much higher temperature [43]. The marked difference in

band structure and charge carrier characteristics between graphene and semiconductor systems allows for a demonstration of the universality of the QHR through a rigorous test of the material independence of the value of $R_K = h/e^2$, the von Klitzing constant. [44]

Over the past decade, epitaxial graphene on SiC has emerged as a promising alternative to GaAs heterostructures for QHR standards. In the years 2010 to 2012, it was demonstrated for the first time that epitaxial graphene can be used for QHR standards, achieving an accuracy level of $n\Omega/\Omega$ at temperatures in the mK range and magnetic fields $B > 11$ T. [8,45,46] Nevertheless, these operating conditions were not yet competitive with those used for GaAs QHR standards. Recent research has shown that graphene QHR standards are able to achieve the accuracy level of $n\Omega/\Omega$ in realizing the ohm under a single optimal condition, e.g., either magnetic field B , current I , or temperature T , while the other two parameters were not optimized. [47–53] For instance, these graphene QHR standards can achieve an accuracy of 10^{-9} but require either high magnetic fields, low currents, or low temperatures. Implementing such experimental conditions for QHR standards requires expensive equipment, liquid cryogenics, and technical expertise. In addition, there was only one recent study reporting on the long-term stability of graphene QHR standards in metrology applications. [52] These are significant obstacles to a simplified and cost-effective practical realization of the ohm and related SI units based on QHR standards. Currently, these limitations do not allow for a wider dissemination and proliferation of primary QHR standards in NMIs, secondary calibration companies, and industry.

Ideally, QHR standards are expected to achieve an accuracy level of $n\Omega/\Omega$ under relaxed experimental conditions, specifically at a low magnetic field B , high current I , and high temperature T . By simplifying the operating conditions (B, I, T), the QHR device will become compatible with portable, compact, and cryogen-free setups, where the superconducting magnet would no longer be necessary. Therefore, the primary standards will become more accessible to secondary calibration companies and industrial applications beyond national metrology institutes (NMIs). Operating such a simplified system can shorten the calibration chain from primary QHR standards to the final product, resulting in higher accuracy for end-users in science, technology, and industry. However, achieving $n\Omega/\Omega$ -level accurate QHR standards under relaxed conditions is challenging due to the mutual constraint of B, I , and T on the QHE physics. For instance, to maintain high accuracy in quantized Hall resistance, decreasing B competes against increasing I and T . Furthermore, the QHR standards used in metrology must maintain high accuracy under relaxed experimental conditions for extended periods of time, ideally years or decades, as demonstrated by GaAs-based QHR standard.

This thesis aims to address these bottlenecks in QHR standards and further improve the performance of graphene QHR standards to underpin wider applications.

1.4 Contributions and Scope

The contributions in this thesis include two aspects: the permanent tailoring of charge carrier density in epitaxial graphene and the realization of the SI unit ohm by the *n*- and *p*-type graphene QHR standards. This thesis presents the results of the high-quality and large-scale epitaxial graphene produced by the sublimation growth on a 6H-SiC substrate. A molecular doping technique is developed in this thesis to enable the free control of the carrier density in epitaxial graphene for the application of resistance metrology. By adjusting the concentration of the 2,3,5,6-Tetrafluoro-7,7,8,8-tetracyano-quinodimethane (F4-TCNQ) molecule, the carrier density in epitaxial graphene can be permanently tuned to the desired values, spanning from the *n*-type to the *p*-type regime. The large-scale and high-quality epitaxial graphene, in conjunction with the advanced F4-TCNQ molecular doping technique, enables the scalable and integrated QHR standards to be patterned on centimeter-sized graphene chips using optical lithography. Both *n*- and *p*-type graphene QHR standards demonstrate the quantum Hall resistance has achieved an accuracy of $1.0 \pm 2.6 \text{ n}\Omega/\Omega$. The $\text{n}\Omega/\Omega$ -level accuracy of the QHR has been maintained over a period of 2.5 years to date. Moreover, the QHR maintains its accuracy even after experiencing long-distance transport between two national metrology institutes. Furthermore, the graphene QHR shows agreement with $R_K/2$ under the simultaneously relaxed conditions of $B = 4.5 \text{ T}$, $I = 232.5 \text{ }\mu\text{A}$, and $T = 4.2 \text{ K}$, thus realizing the SI unit of electrical resistance, the ohm (Ω).

This thesis commences in Chapter 1 with an introduction to the history of graphene, the epitaxial growth of graphene on SiC, and the QHR standards based on epitaxial graphene.

Chapter 2 provides an overview of the basic characteristics of graphene and its distinctive electronic properties. Chapter 2 also introduces the magnetotransport theory in graphene, which is related to its unique electronic structure. The transport theory includes the classical and quantum Hall effect and how this is modified in the case of graphene. This knowledge is useful throughout the results and discussions.

Chapter 3 explains the material growth setup, characterization technique, device fabrication, magnetotransport setup, and high-accuracy measurement system. Epitaxial graphene is grown on semi-insulating 6H-SiC substrates in a furnace at a temperature exceeding $1750 \text{ }^\circ\text{C}$. Surface

science measurements are used to characterize the quality of graphene. The fabrication of graphene QHR standards includes two steps: device fabrication by optical lithography and the F4-TCNQ molecular doping technique. Magnetotransport measurement is used to investigate the transport properties of epitaxial graphene. High-accuracy measurement is used to investigate the performance of graphene QHR standards.

Chapter 4 describes the F4-TCNQ molecular doping technique, whereby an F4-TCNQ powder is dissolved into PMMA to form a dopant blend. By precise adjustment of the F4-TCNQ dopant concentration in PMMA, the carrier density can be tuned to the desired values, from initial n - to the p -type regime across the charge neutrality point. As the F4-TCNQ molecular doping technique deals with a compensation doping process, it is of the utmost importance to reliably reproduce the initial carrier density of epitaxial graphene. This was accomplished by the pre-annealing process prior to the doping procedure. Further, the scattering mechanisms of epitaxial graphene at low and high temperature ranges are discussed. Because of the strong interaction between the graphene and the buffer layer/SiC substrate, the charge carriers of epitaxial graphene exhibit distinct scattering properties in comparison with the exfoliated graphene on SiO₂ or hexagonal boron nitride (hBN) substrates. At low temperatures ($T < 20$ K), the scattering is dominated by short-range and long-range scattering. At high temperatures above 20 K and below 300 K, additional scattering mechanisms emerge as a result of the interaction between graphene and the SiC substrate. These include remotely interfacial phonons (RIPs) and longitudinal acoustic (LA) phonons, which act as additional scatterers as the temperature increases. Finally, a doping model is proposed to explain the F4-TCNQ molecular doping process on the graphene/SiC surface.

Chapter 5 presents the high-accuracy measurements of various n - and p -type QHR devices with carrier densities over a wide range to achieve the $n\Omega/\Omega$ -level accuracy of the quantized Hall resistance. The high-accuracy measurement results of the n -type device demonstrate that the quantized Hall resistance with an accuracy of $(0.7 \pm 2.6) n\Omega/\Omega$ can be achieved in a wide magnetic field range from 4 to 12 T at 4.2 K. The graphene QHR standards fabricated by the different doping stacks (5 layer-, 3 layer-, and 2 layer- doping stacks) are tested in high-accuracy measurements, indicating the controlled doping effect and identical performance for resistance metrology. A systematic high-accuracy measurement of the QHR devices with varying electron densities has revealed that the onset of the quantization regime is dependent on the electron density. A 2D contour plot of the quantization regime is proposed to reveal the correlation between the quantization regime and the electron density, as well as the magnetic field.

Moreover, we compare the performance of our graphene QHR standard with that of a commercial one from Graphenesic AB company. Our graphene QHR standard exhibits superior performance compared to the commercial counterpart. Furthermore, the investigation is extended to *p*-type graphene QHR standards. These *p*-type graphene QHR standards also achieve an accuracy of $(2 \pm 2.6) \text{ n}\Omega/\Omega$ over a wide magnetic field range from 4.5 to 12 T at 4.2 K. The quantization regime of the *p*-type QHR standard is asymmetric with that of the *n*-type QHR standard. Finally, the QHR standard is investigated at high temperatures up to 300 K in order to explore the temperature limit of the accurate quantum Hall resistance. The temperature-dependent measurement results demonstrate that the $\text{n}\Omega/\Omega$ accuracy of QHR of epitaxial graphene is limited below 25 K. As the temperature increases above 25 K, the quantum Hall resistance deviates from the theoretical value $R_K/2$. This is attributed to the phonon-mediated quantum Hall transport in epitaxial monolayer graphene.

Chapter 6 presents high-accuracy measurements over a period of two years to investigate the long-term stability of graphene QHR standards. The devices were stored in a closed chamber with a mixture of nitrogen (N_2) and air at low humidity at room temperature for a period exceeding two years. Regular measurements demonstrated that graphene QHR standards allow for the realization of the ohm with an accuracy of $\text{n}\Omega/\Omega$ at a low magnetic field of $B = 4.5 \text{ T}$, a high current of $I = 232.5 \text{ }\mu\text{A}$, and a temperature of $T = 4.2 \text{ K}$, simultaneously. Meanwhile, repeated high-accuracy measurements demonstrate the robustness of the QHR standards over multiple cool-down cycles and their long-term stability over several years. In particular, we demonstrate that the quantized resistance remains stable within an accuracy of $\text{n}\Omega/\Omega$ over a period of 2.5 years to date. Furthermore, this level of accuracy has been maintained without any indication of degradation, even after undergoing long-distance transport between the Physikalisch-Technische Bundesanstalt (PTB) and the International Bureau of Weights and Measures (BIPM).

The final chapter, Chapter 8, presents a summary of the main results, alongside concluding remarks and an outlook.

Chapter 2. Theory and concepts

2.1 Crystal and electronic structure

Graphite is a crystalline form of the element carbon, which is composed of a layer-by-layer structure of graphene. The three-dimensional (3D) structure of graphite is held together by weak interlayer van der Waals forces, including some electronic delocalization. The macroscopic properties of graphite are determined by the crystal's covalent bonds. The σ bonds are in the plane of the graphene sheet. Within each layer, the carbon atoms are arranged in a honeycomb lattice connected by the in-plane sp^2 σ -bonds. The π bonds are perpendicular to the graphene sheet. Above and below the layer, π -bonds are formed that delocalize the electron wave function, thereby rendering graphite electrically and thermally conductive along the planes. In addition, these π -bonds facilitate the formation of van der Waals bonds between the layers, which serve to maintain the stacked configuration. Due to the weak van der Waals force, graphene-like layers in graphite are easy to separate and glide past each other. Therefore, graphite is used to make pencils. Since van der Waals bonds originate from induced electric dipoles, the electrical and thermal conductivities in the direction perpendicular to the layers in graphite are relatively poor. [54] As will be introduced subsequently in this chapter, graphene is essentially a single isolated layer of graphite, and bilayer, trilayer, and multilayer graphene is merely a very thin portion of graphite. [54]

Graphene is a material consisting of a single layer of carbon atoms arranged in a hexagonal (honeycomb) lattice. The carbon atoms in the lattice are separated by 1.42 Å. Each carbon atom has three nearest neighbors at an angle of $\approx 120^\circ$, which gives graphene its characteristic honeycomb structure. Such an atomic structure is characterized by the presence of two types of bonds and exhibits the so-called planar sp^2 hybridization. The valence orbitals of the graphene lattice include the $2s$, $2p_x$, $2p_y$, and $2p_z$ orbitals, where z is perpendicular to the sheet. Among the four valence orbitals, the (s, p_x, p_y) orbitals combine to form the in-plane σ (bonding or occupied) and σ^* (anti-bonding or unoccupied) orbitals, which are with respect to the planar symmetry. The σ bonds are strong covalent bonds that are responsible for the majority of the binding energy and the robustness of the lattice structure in a graphene sheet (Fig. 2.1a-b). [20,55] The remaining p_z orbital, pointing out of the graphene sheet (Fig. 2.1a-b), is odd with respect to the planar symmetry and cannot couple with the σ states. The lateral interaction with neighboring p_z orbitals results in the formation of delocalized π (bonding) and π^* (anti-

bonding) orbitals (Fig. 2.1a-b). [20] The π -band emerges from tunneling between the unaffected p_z orbital, which is perpendicular to the planar structure. Since each p_z orbital has one extra electron, the π -band is half-filled. The bonding π - and anti-bonding carbon π^* -orbitals form wide electronic valence and conduction bands (Fig. 2.1c), which cross the Fermi level at high-symmetry points in the Brillouin zone of graphene. [20,55]

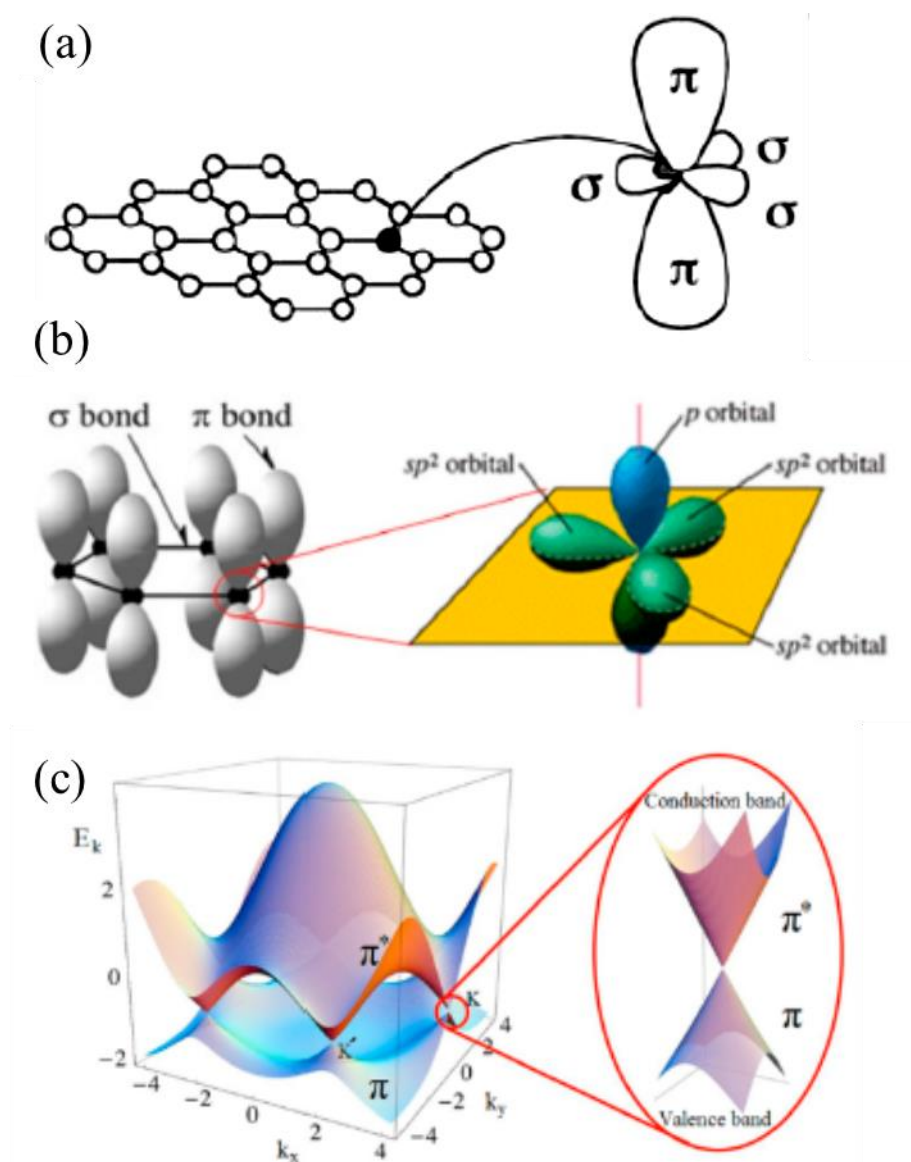


Figure 2.1 Illustration of the carbon valence orbitals (a): the three σ orbitals in graphene and the π orbital perpendicular to the sheet. The σ bonds in the carbon hexagonal network strongly connect the carbon atoms and are responsible for the binding energy and the elastic properties of the graphene sheet. The π bonds are perpendicular to the surface of the sheet. (b) σ and π bonds in graphene; (c) graphene π - and π^* -band structure. Adapted from Ref. [3,55]

The graphene plane is a hexagonal lattice with two atoms per unit cell (A and B) and a basis defined by the vectors (\vec{a}_1, \vec{a}_2) . The graphene lattice in real and reciprocal (momentum) space can be seen in Figure 2.2 (a) and (b), respectively. The distance of adjacent carbon atoms is $a_{cc} = 1.42 \text{ \AA}$, and the lattice constant is $a_1 = a_2 = \sqrt{3}a_{cc} = 2.46 \text{ \AA}$. The real space unit cell can be described by lattice vectors:

$$|\vec{a}_1| = |\vec{a}_2| = \sqrt{3}a_{cc}$$

$$\vec{a}_1 = \sqrt{3}a_{cc} \left(\frac{\sqrt{3}}{2}, \frac{1}{2} \right) \quad (2.1)$$

The reciprocal lattice of graphene is given by:

$$\vec{b}_1 = \frac{2\pi}{3a_{cc}}(1, \sqrt{3}), \quad \vec{b}_2 = \frac{2\pi}{3a_{cc}}(1, -\sqrt{3}) \quad (2.2)$$

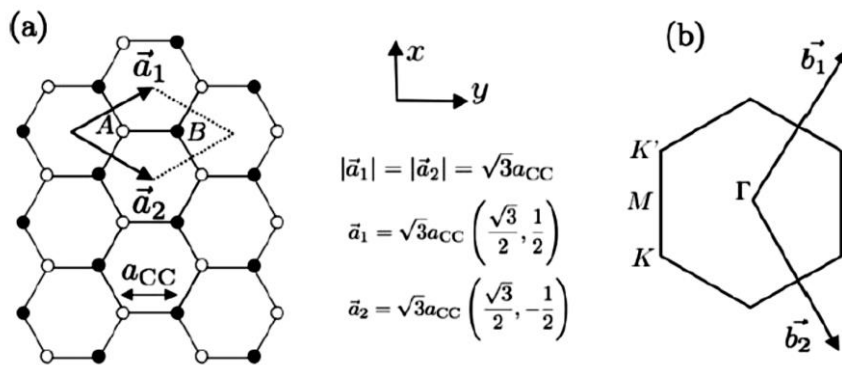


Figure 2.2. Basis vectors in the hexagonal lattice of graphene (a) and the corresponding Brillouin zone (b). The reciprocal basis vectors read: $\vec{b}_1 = b \left(\frac{1}{2}, \frac{\sqrt{3}}{2} \right)$ and $\vec{b}_2 = b \left(\frac{1}{2}, -\frac{\sqrt{3}}{2} \right)$, with $b = 4\pi/a\sqrt{3}$, where $a = \sqrt{3}a_{cc}$ and $a_{cc} = 1.42 \text{ \AA}$ is the carbon-carbon distance in graphene. Adapted from Ref. [55]

Graphene is a semi-metal with linear energy dispersion around the Dirac point due to its 2-dimensional honeycomb structure. [5] This makes the material behave differently from conventional semiconductors and, therefore, opens new avenues for revolutionary applications, such as RF devices, sensors, and highly accurate metrology. [4]

One model to derive the electronic band structure of graphene is to use the tight-binding approach. The tight-binding Hamiltonian for electrons in graphene considers that electrons can hop to both nearest- and next-nearest-neighbor atoms. [20] The energy bands derived from this Hamiltonian have the form:

$$E_{\pm}(\vec{k}) = \pm r_0 \sqrt{3 + f(\vec{k})} \quad (2.3)$$

where

$$f(\vec{k}) = 2 \cos(\sqrt{3}k_y a) + 4 \cos\left(\frac{\sqrt{3}}{2}k_y a\right) \cos\left(\frac{3}{2}k_x a\right) \quad (2.4)$$

The value r_0 can be derived from the first principle calculation [56,57] and has been experimentally determined to be 3.38 eV [58]. In theory, the Fermi level of graphene is exactly at the Dirac point. The DOS below the Dirac point are fully filled, while those above the Dirac point are empty. Graphene is thus a zero-band gap semi-metal, with the Fermi level located at the intersections between the valence and conduction (π and π^*) bands, which are located at the \mathbf{K} and \mathbf{K}' points in k -space. In reality, the existence of charge impurity below the graphene lattice or/and defect in the lattice can move the Fermi level above or below the Dirac point. Thus, graphene is not neutral and exhibits n - or p -type conductivity due to the free electrons or holes at the Fermi level.

2.2 Low-energy spectrum

The results from the tight-binding model are particularly interesting close to the \mathbf{K} and \mathbf{K}' points in reciprocal space, where the energy dispersion is $E \propto k$, in contrast to $E \propto k^2$ in conventional electrical semiconductors. Around these \mathbf{K} , \mathbf{K}' points, the energy dispersion of carriers is similar to that of ultra-relativistic particles with zero rest mass m_0 , $E(\vec{k}) = \sqrt{m_0^2 c^4 + c^2 \hbar^2 k^2} = c \hbar k$. Under these conditions, the Schrödinger equation for Bloch electrons reduces to the 2D Dirac equation. The Dirac equation is thus used to describe the behavior of carriers, massless Dirac Fermions, around the \mathbf{K} , \mathbf{K}' points, which are also called Dirac points.

Considering the electronic energy near the Dirac point, equation 2.4 can be transformed using a Taylor expansion around the \mathbf{K} points using $\mathbf{k} = \mathbf{K} + \mathbf{q}$ with $|\mathbf{q}| \ll |\mathbf{K}|$. The higher order terms $O = q^2/K^2$ is very small and thus can be ignored, resulting in a linear dispersion relation between the energy E_k and the wavevector \mathbf{q} ,

$$E_k = \hbar v_F |\mathbf{q}| \quad (2.5)$$

Where \mathbf{q} is measured from the Dirac points, v_F is the Fermi velocity $v_F = \frac{1}{\hbar} \frac{\partial E}{\partial k}$, which is approximately $v_F \approx 10^6$ m/s. [58] The linear dispersion of graphene can derive the relation

that $dE/dk = \pm\hbar v_F$, which indicates that the charge carriers are massless Dirac fermions and travel at a constant speed. In the reciprocal space $kdk = |E|dE(\hbar v_F)^2$, therefore the density of states (DOS) near the Dirac points can be calculated as,

$$DOS(E) = g_s g_v \frac{|E|}{2\pi(\hbar v_F)^2}, \quad (2.6)$$

where $g_s = g_v = 2$ representing spin (up and down) and valley (\mathbf{K} and \mathbf{K}') degeneracies. The DOS is linear with energy. No states exist at the Fermi level in an ideal and intrinsic graphene sample. In reality, this is not true because of the present of disorder in the system.

The Fermi energy of graphene can be derived from the DOS in Equation 2.6. Below the Fermi energy, the states are occupied. The carrier density n in the energy range can be calculated by the equation below,

$$n = \int_0^\infty DOS(E)f(E)dE \quad (2.7)$$

For simplicity, the temperature can be assumed to be zero, in which case the Fermi distribution $f(E)$ turns into the Heaviside step function (=1 for energies below E_F , zero otherwise), and the upper energy limit of the integral becomes the Fermi energy E_F . Thus, the carrier density is:

$$n = \frac{E_F^2}{\pi(\hbar v_F)^2} \quad (2.8)$$

In other words, the Fermi energy depends on the square root of the carrier density:

$$E_F = \hbar v_F \sqrt{\pi n} \quad (2.9)$$

2.3 Magnetotransport in graphene

2.3.1 Classical Hall effect

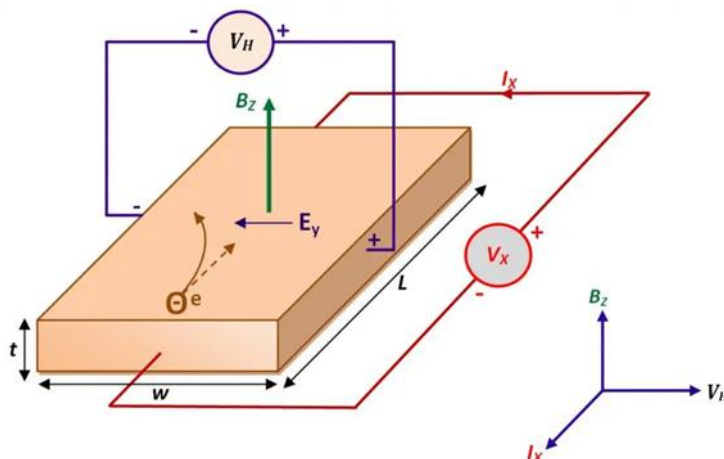


Figure 2.3 The schematic of the Hall effect for an n -type semiconductor. In the presence of a magnetic field B_z perpendicular to the applied current I_{xx} , electrons are deflected to the left side under the influence of the Lorentz force.

The Hall effect is a fundamental phenomenon in solid-state physics that provides valuable insights into the electronic properties of materials, particularly semiconductors. The classical Hall effect arises when a current-carrying conductor is subjected to a magnetic field perpendicular to the current flow. [59] A schematic of the Hall measurement for an n -type semiconductor is depicted in Figure 2.3. In the presence of a magnetic field perpendicular to the applied current, the electrons are deflected under the influence of Lorentz force, $F = q\mathbf{v} \times \mathbf{B}$. As a result, an electric field perpendicular to both the current direction and the magnetic field develops, generating a voltage difference across the material. This voltage difference is referred to as the Hall voltage V_H . The Hall voltage can be described by the following equation:

$$V_H = V_{xy} = -\frac{1}{n_e e} \frac{I_{xx} B_z}{t} \quad (2.10)$$

Where V_H is the Hall voltage, I_{xx} is the current flowing through the sample in the x direction, B_z is the magnetic field in the z -direction, n_e is the electron concentration, e is the elementary charge, and t is the thickness of the sample. Under these conditions, the resistivity of the sample takes a tensor form, being different in the direction parallel or perpendicular to the direction of the current. For a 2D conductor, the 2D resistivity is $\rho_{2D} = \rho_{3D}/t$. ρ_{2D} has the same dimensions as the 3D resistance (Ω). In order to avoid confusion, the units of ρ_{2D} are usually explicitly

written as $\Omega / (L/W) = \Omega/\text{square}$. Sometimes, the words resistance and resistivity for 2D samples are used indistinctly. Therefore, in the 2D material, the transversal resistance R_{xy} can be expressed as

$$R_{xy} = -\frac{V_{xy}}{I_{xx}} = \frac{B_z}{n_s e} \quad (2.11)$$

Where $n_s = nt$ is the sheet carrier density in 2D geometry. The term $1/n_s e$ is known as the Hall coefficient R_H . The Hall coefficient R_H is a material-dependent parameter that characterizes the strength and nature of the Hall effect. For semiconductors, the Hall coefficient can be expressed as:

$$R_H = \frac{1}{ne} \quad (2.12)$$

The longitudinal resistivity of the sample ρ_{xx} is independent of the magnetic field. It can be obtained by measuring the voltage developed along the direction of the current and considering the geometry of the sample (length L and width W).

$$\rho_{xx} = \frac{W V_{xx}}{L I_{xx}} \quad (2.13)$$

Equation 2.12 shows that the Hall coefficient depends on the carrier concentration. In practice, the polarity of V_H determines the sign of the charge carriers. Therefore, the Hall coefficient can provide valuable information about the charge carrier type and concentration in a semiconductor material. A Hall measurement can also determine the carrier mobility μ ,

$$\mu = 1/(ne\rho) \quad (2.14)$$

In our classical model of the Hall effect, free charge carriers are considered a single type of charge carrier.

2.3.2 Integer Quantum Hall effect

From classical considerations, the transversal resistance ρ_{xy} depends linearly on the external magnetic field B (Eq. 2.11), while the longitudinal resistance ρ_{xx} is a constant. The classic Hall effect picture breaks down when working with a high mobility, 2D system at low temperatures and in strong magnetic fields. [34] This is not the case for the high mobility of 2D systems at low temperatures and strong magnetic fields. Oscillations in ρ_{xx} (B) and steps in ρ_{xy} (B) are

observed; the former are called Shubnikov-de Haas oscillations, and the latter is the quantum Hall effect.

In 1980, Klaus von Klitzing discovered the quantum Hall effect (QHE) in two-dimensional electron systems subjected to low temperatures and strong magnetic fields, in which the Hall resistance R_{xy} exhibited steps that take on the quantized values, while simultaneously the longitudinal resistance ρ_{xx} drops to zero. Figure 2.4 shows a typical resistance measurement on a GaAs/AlGaAs sample. Steps and plateaus in the transversal resistance occur at universal values of $\rho_{xy} = h/\nu e^2$, with h being the Planck constant, e the elementary charge, and ν the integer. In the theory of integer QHE [60], the resistance of plateaus is related to R_K divided integer ν . The integer QHE has been observed in the monolayer of graphene at room temperature. [61]

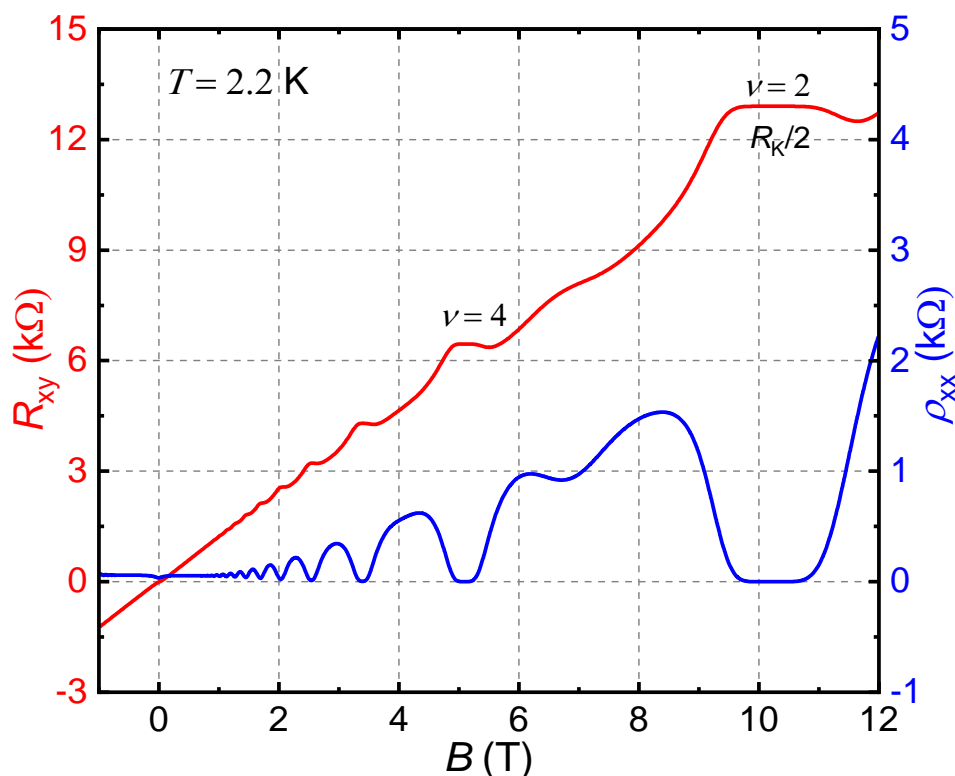


Figure 2.4 QHE Measurements of the Hall resistance R_{xy} and the longitudinal resistance R_{xx} for a GaAs/AlGaAs heterostructure at a temperature of 2.2 K.

An important property is the high accuracy of measurements of R_{xy} at the plateaus. This leads to the value of the quantum Hall resistance at filling factor 1 to be chosen as resistance standards, named the von Klitzing constant R_K . In 1990, the value of this constant was fixed at $R_{K-90} = 25812.807 \Omega$ by the International Committee for Weights and Measures (CIPM). Since 2019, the revised SI units defined the von Klitzing constant R_K as directly connected to the Planck constant h and the elementary charge e , $R_K = h/e^2$. [62] Its value is,

$$R_K = \frac{6.626\ 070\ 15 \times 10^{-34} \text{ J} \cdot \text{S}}{(1.602\ 176\ 634 \times 10^{-19} \text{ C})^2} = 25\ 812.807\ 459\ 3045 \dots \Omega \quad (2.15)$$

2.3.3 Landau level

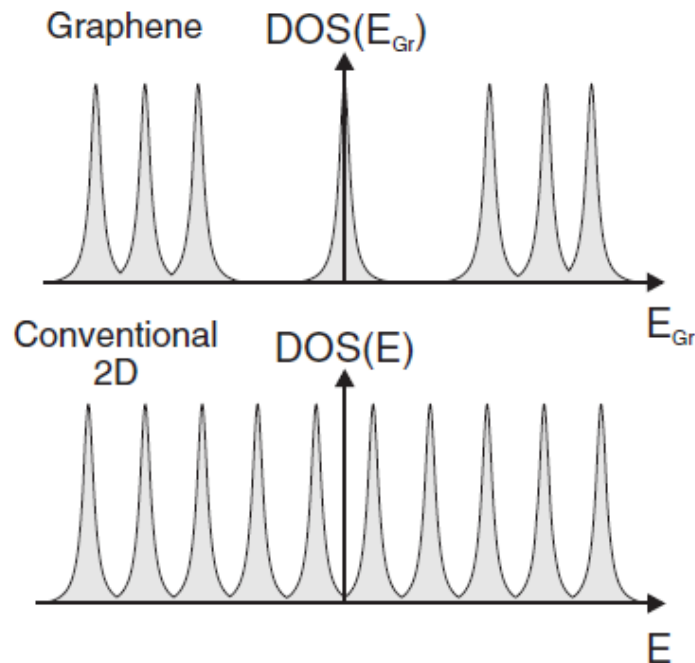


Figure 2.5 In the absence of disorder, the broadening of Landau levels presents in graphene and conventional 2D GaAs/AlGaAs heterostructures. Quantized cyclotron motion leads to the formation of Landau levels in the DOS. Adapted from Ref. [44]

The QHE can be understood as a consequence of Landau quantization. [63] The quantum effects become visible in the subject of low temperatures and high magnetic fields. In a strong magnetic field perpendicular to a plane, in-plane electrons with a constant velocity move in circular orbits. As the magnetic field increases, the size of the cyclotron orbit shrinks and becomes comparable to the electron wavelength. If the electron mobility is high enough, the electron motion can complete some specific cyclotron orbits, and the length of the orbits is equal to an integer number times the electron wavelength. Thus, the energy of the electrons and the frequency of the cyclotron orbits are quantized. Quantized cyclotron motion dramatically modifies the density of states (DOS) by breaking it into discrete levels, the so-called Landau levels (LLs), which are the allowed energies for cyclotron orbits under quantizing conditions. [44] Figure 2.5 presents the formation of LLs in the DOS in graphene and conventional 2D GaAs/AlGaAs heterostructures.

2.3 Magnetotransport in graphene

For non-relativistic fermions such as in GaAs/AlGaAs heterostructures, the LLs are equally spaced with a spacing of \hbar times the semiclassical cyclotron frequency ω_c , which is linearly dependent on B as shown in Figure 2.6(a). The corresponding energy eigenvalues are

$$E_N = \left(N + \frac{1}{2}\right) \frac{\hbar e B}{m^*} = \left(N + \frac{1}{2}\right) \hbar \omega_c \quad (2.16)$$

where $N = 0, 1, 2, 3, \dots$, and the cyclotron frequency is defined as $\omega_c = eB/m^*$. Therefore, the energy of the cyclotron motion is quantized. These quantized energy levels are known as LLs, and N is the LL index.

In theory, each LL is a heavily degenerate delta function in the DOS without energy broadening. In real samples, the presence of disorder broadens the delta function of the LLs, as shown in Figure 2.5. Due to the LLs broadening, localized and extended states have been formed. [64,65] When the Fermi level is located in the extended states, electrons in the bulk can flow from one contact to another contact in the states, and the backscattering is inevitable, resulting in the longitudinal resistance in QH measurement. When the Fermi level moves from the extended states to the localized states, electrons in the bulk cannot flow in these states. Only the edge states allow for the current flow without backscattering in transport, resulting in zero longitudinal resistance and quantized Hall resistance.

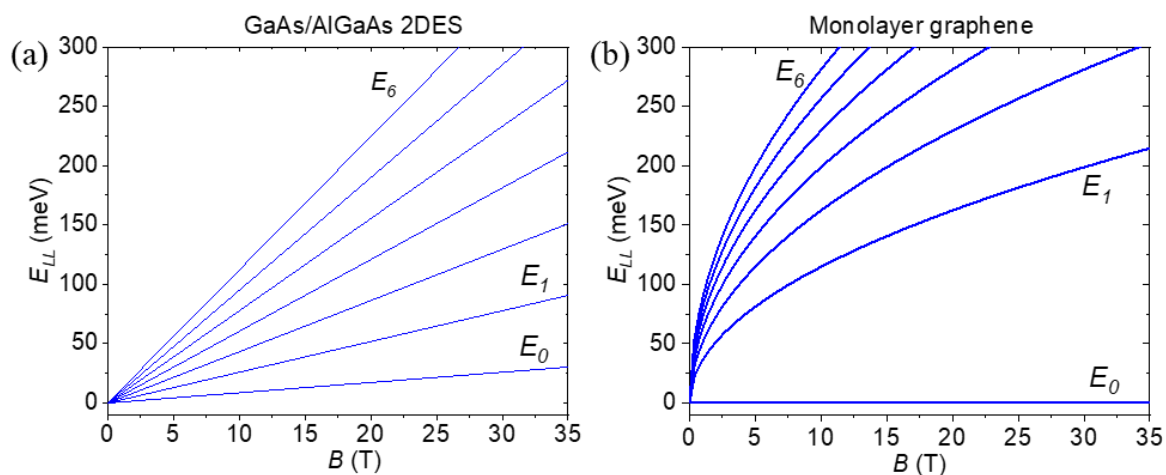


Figure 2.6 Landau level spectra of (a) GaAs/AlGaAs 2DES and (b) monolayer graphene with Landau index N from 0 to 6.

For graphene, the LL spectra and integer numbers exhibit different behaviors in conventional 2D semiconductors and graphene. The Landau levels of graphene at each Landau index N increase linearly with the \sqrt{B} . Due to the distinct electronic structures and dispersion relations,

the charge carriers are massless Dirac fermions in graphene. The Landau level spectrum in graphene is given by,

$$E_n = v_F \sqrt{2\hbar eBN} = \sqrt{N} \hbar \omega'_c, \quad (N = 0, 1, 2, 3 \dots) \quad (2.17)$$

where

$$\omega'_c = v_F \sqrt{\frac{2eB}{\hbar}} \quad (2.18)$$

is defined as the cyclotron frequency for massless Dirac fermions.

In contrast to the conventional 2D semiconductor case, the Landau levels of graphene have three important features. (1) As mentioned above, the Landau levels at each Landau index N depend on the magnetic field as $E_n \propto \sqrt{B}$, instead of $E_n \propto B$ in conventional 2D semiconductor case. (2) The energy difference between the N th and the $(N+1)$ th levels are unevenly distributed in graphene, $\Delta E_{LL} \propto (\sqrt{N+1} - \sqrt{N})\sqrt{B}$. Therefore, the most significant energy separation exists between the 1st and the 0th Landau levels. However, the energy difference is equidistance in conventional 2D semiconductors, $\Delta E_{LL} \propto B$. (3) The 0th Landau level always has zero energy, which is independent of magnetic fields. The states in the 0th Landau level are equally shared by electrons and holes. Therefore, this special zero-energy Landau level is only two-fold degenerate (spin). All these features are consequences of the unique nature of massless Dirac fermions in monolayer graphene. [5,54]

In the above, we discussed the Landau level spectrum in graphene and conventional 2D GaAs/AlGaAs heterostructures. In high magnetic fields, the DOS in energy exhibits a different distribution in zero magnetic fields. In the quantum regime, the DOS at each Landau level is a function of the magnetic field B . The available states N_{LL} per area in each Landau level is described as,

$$N_{LL} = \frac{\Phi}{\Phi_0} = \frac{B}{h/e} = \frac{eB}{h} \quad (2.19)$$

In Equation 2.19, Φ is the total magnetic flux through the sample, which is B . $\Phi_0 = h/e$ is the quantum of magnetic flux. Thus, the states pre-area in each Landau level are obtained by Φ/Φ_0 .

At a given electron (holes) density n_s , the states pre-area in each Landau level N_{LL} can be calculated from the magnetic flux density (magnetic field B). The number of filled Landau levels, a dimensionless quantity known as the filling factor ν , can be calculated by Equation,

$$\nu = \frac{n_s}{N_{LL}} = \frac{n_s h}{eB} \quad (2.20)$$

Considering the Landau level degeneracy, the GaAs/AlGaAs heterostructures have two-fold degeneracies, $g_s = 2$, and the filling factor $\nu = 2(N + 1)$. Factor 2 comes from spin up and spin down degeneracies. In monolayer graphene, the filling factor is $\nu = 4(N + 1/2)$. The four folds degeneracies at Landau index $N = 1, 2, 3 \dots$ corresponds to the spin and valley degeneracies, $g_s = g_v = 2$. At Landau index $N = 0$, graphene only has 2-fold spin degeneracies, and there is no valley degeneracy at $N = 0$. [66] Thus, the energy of charged electrons (or holes) in a high magnetic field is quantized into highly degenerate Landau levels.

Assuming the electron fully filled the N th Landau level, the charge carrier density for GaAs/AlGaAs heterostructures is,

$$n_s = \frac{2B}{h/e} (N + 1) = \frac{2eB}{h} (N + 1) \quad (2.21)$$

The carrier density for graphene is,

$$n_s = N \frac{4B}{h/e} + \frac{2B}{h/e} = \frac{4eB}{h} \left(N + \frac{1}{2} \right) \quad (2.22)$$

The quantum Hall plateaus at filling factor $\nu = 0, 2, 6, 10, \dots$ is the fingerprint of monolayer graphene and can be used experimentally to prove that electronic transport occurs through a single graphene layer.

When the Fermi level lies in a gap between two Landau levels and the Landau levels below the Fermi level are fully occupied, the filling factor ν in Equation 2.20 must be an integer. Thus, the carrier density is $n_s = \nu N_{LL}$. If we substitute this carrier density into the classical Hall effect Equation 2.11, we find that ρ_{xy} is quantized as

$$\rho_{xy} = \frac{B}{en_s} = \frac{B}{e\nu N_{LL}} = \frac{h}{\nu e^2} \quad (2.21)$$

Maxima in ρ_{xx} are observed every time the Fermi level crosses the center of a LL; plateaus in ρ_{xy} and vanishing ρ_{xx} are observed whenever the Fermi level lies in the middle of two LLs, pinned by localized states. [44]

Chapter 3. Experimental techniques and instruments

3.1 Epitaxial graphene growth

Three main methods exist to fabricate monolayer graphene: mechanical exfoliation from graphite, chemical vapor deposition (CVD) on metal foils, e.g., copper substrate, and epitaxial growth on SiC substrate. The mechanical exfoliation process is limited to the production of graphene sheets in micrometers and arbitrary geometry, rendering it unsuitable for the mass production of graphene-based electronics in industry. The transfer process to an insulating substrate will introduce additional defects. The CVD synthesis on metal foils is notorious for non-uniformity, including grain boundaries and polycrystalline structures. This makes it challenging to scale for commercial use. Prior to the device fabrication, the graphene on the metal substrate must be transferred to an insulating substrate. This process is not straightforward for the fabrication of graphene devices, and it can result in contamination and degradation of graphene. [67] Thus, the transfer process of graphene is a significant obstacle for graphene QHR standards to achieve high accuracy on the level of $n\Omega/\Omega$, which is essentially required for the application of resistance metrology.

To develop practical graphene QHR standards, the preferred method presented in this thesis is epitaxial growth on a semi-insulating SiC substrate. Epitaxial graphene grown on the semi-insulating SiC substrate is advantageous for device fabrication because it eliminates the transfer process. This method utilizes the thermal decomposition of the SiC substrate to produce a monocrystalline graphene layer over an entire wafer. [29,68] This enables readily mass fabrication of large-scale electronic devices without significant deterioration or contamination, as demonstrated in Chapters 4 and 5. All graphene QHR devices presented in this thesis were fabricated from epitaxial graphene grown on the Si face of semi-insulating 6H-SiC.

3.1.1 Growth setup

This thesis employs a horizontal inductively heated quartz tube reactor [69] to grow epitaxial graphene on a semi-insulating SiC substrate by thermal decomposition of SiC. Figure 3.1 presents the graphene growth setup in the cleanroom. All the graphene presented in this thesis were grown by the setup. The cylindrical graphite susceptor at the center of the inductive coil is subjected to an induction heating system, acting as a sample holder for the graphene and dummy samples. As shown in Figure 3.2, the SiC substrates ($10 \times 5 \text{ mm}^2$) are positioned within

3.1 Epitaxial graphene growth

the sample pocket of the susceptor. In this configuration, the primary samples are surrounded by dummy SiC samples to mitigate the potential influence of the susceptor's sidewall at elevated temperature annealing. During a single growth cycle, at least three pieces of graphene ($10 \times 5 \text{ mm}^2$) can be processed within the susceptor. This setup can grow large-scale and high-quality epitaxial graphene with high reproducibility.

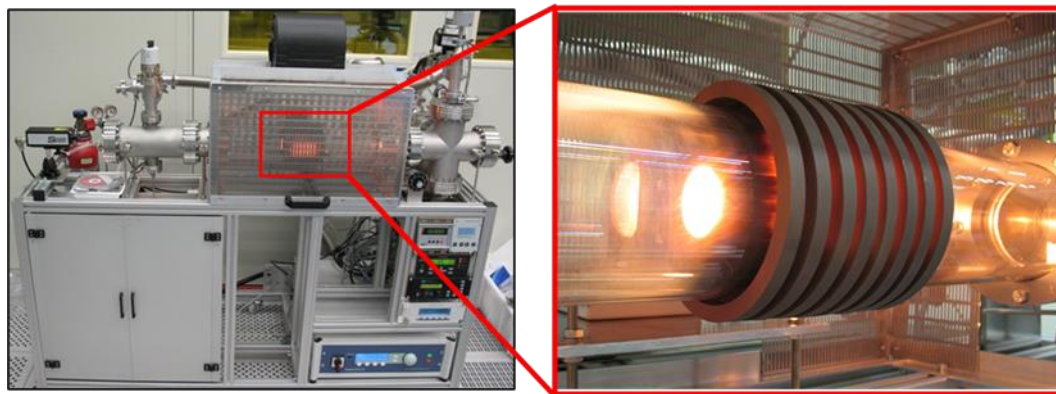


Figure 3.1 The horizontal quartz tube reactor setup is used for epitaxial growth of graphene on SiC.

The growth process requires a high vacuum up to 10^{-7} mbar, controllable high temperatures up to $1950 \text{ }^\circ\text{C}$, and reliable gas flow. The vacuum system comprises a scroll pump and a turbo molecular pump, which can achieve a 10^{-7} mbar pressure within the well-sealed quartz tube. An induction heating system with a maximum power of 11 kW is used to reach the desired growth temperature. An automated control system is designed to regulate the set-point temperature and actual temperature by controlling the furnace's heating power. [70] The temperature inside the susceptor is continuously monitored through a pyrometer during the growth process because accurate control of the growth temperature is essential for the growth process. An insulation layer of graphite surrounds the hot susceptor, reducing the thermal stress on the quartz glass cylinder, which is actively cooled with ambient air from the outside by a radial fan. A control system based on National Instrument LabView controls the gas flow, pressure, temperature, valves, and pumps. Argon (Ar), nitrogen (N_2), and a mixture of argon/hydrogen (95 % Ar and 5 % H_2) are three distinct gases that can be directed via disparate inlets to the chamber. The flow rate of the gases can be managed through mass flow controllers.

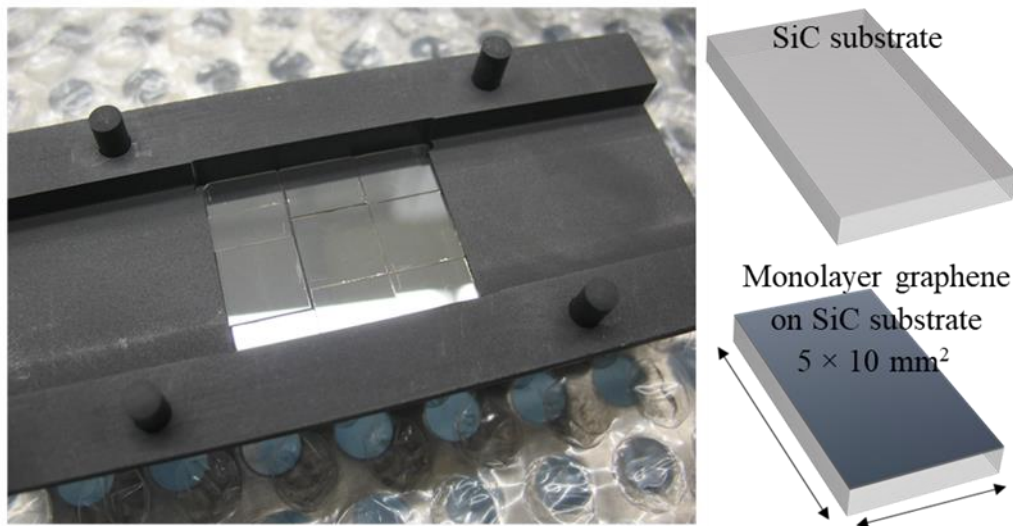


Figure 3.2 (left) The image of graphite susceptor and SiC substrate ($10 \times 5 \text{ mm}^2$) for growth. Dummy samples in the pocket surround the SiC substrates. (right) After the epitaxial growth, the entire SiC substrate is covered by monolayer graphene.

3.1.2 Polymer-assisted sublimation growth method

Epitaxial graphene in this study was grown on semi-insulating 6H-SiC substrates provided by *II-VI Comp.* The company is known for providing high-quality and low-miscut angle SiC. To achieve epitaxial growth of graphene, it is essential to consider product specifications, miscut angle, crystal defect density, and deformation. The SiC substrates were chosen to ensure homogeneous surface properties, with a micropipe defect density below 0.25 cm^2 , warp below $10 \text{ }\mu\text{m}$, and bow below $5 \text{ }\mu\text{m}$. To prepare for growth, the 4-inch SiC wafer was diced into rectangular chips ($5 \times 10 \text{ mm}^2$) using a resin bond diamond blade on the carbon face side in the clean room facility at the PTB [70]. It is important to note that the SiC substrate is a semi-insulator compensated by vanadium dopants with a resistivity of $\rho > 10^9 \text{ }\Omega\cdot\text{m}$. The very high resistance of the semi-insulating substrate prevents free carrier transport through it. This property is crucial for producing advanced graphene QHR devices for metrological applications.

Monolayer graphene was grown on a semi-insulating 6H-SiC(0001) specimen ($5 \times 10 \text{ mm}^2$) using the polymer-assisted sublimation growth (PASG) method. [70–73] In this thesis, the high-quality monolayer epitaxial graphene is obtained by the PASG method. The core idea of this method is to seed the growth of the surface stabilizing buffer layer with an external carbon source before the smooth surface morphology is destroyed by step bunching, which often occurs during high-temperature annealing. To implement this idea, a polymer of the AZ5214E photoresist is deposited onto the SiC substrate, which supplies additional carbon atoms for the

graphene growth process and assists in the formation of the buffer layer. The PASG effectively suppresses the inherent but unfavorable formation of high SiC surface terrace steps during high-temperature sublimation growth. This is achieved by the rapid formation of the graphene buffer layer, which stabilizes the SiC surface. The nominal miscut of the SiC wafer from *II-VI Comp.* is about -0.06° towards $[1\bar{1}00]$ crystal direction and almost zero towards $[11\bar{2}0]$ crystal direction. Sublimation growth is performed in Ar gas at 1800°C and 900 mbar pressure for 6 minutes.

The process of growing monolayer graphene on SiC involves two steps. First, at high temperatures, Si atoms sublime from the SiC crystal, and the carbon atoms assemble into a first carbon lattice, forming a buffer layer on the substrate. Second, a new buffer layer is formed under the first buffer layer, which then separates from the bonds of the SiC substrate, resulting in the first buffer layer becoming a monolayer graphene. [74,75] In summary, monolayer graphene is formed from the first carbon lattice, while the second carbon lattice acts as a buffer layer between the monolayer graphene and the SiC substrate. This unique buffer layer is crucial for the transport properties of the epitaxial graphene on SiC, which we will discuss further in the quantum transport results.

3.2 Surface characterization techniques

3.2.1 Laser scanning confocal microscopy

Laser scanning confocal microscopy (LSCM) is a useful, fast, and efficient optical imaging technique, which is widely used in material science, semiconductor inspection, and life science. Confocal microscopy has higher image resolution compared with conventional optical microscopes, but its image resolution is less than that of scanning electron microscopy (SEM) and atomic force microscopy (AFM).

To further understand the principle of confocal microscopy, I briefly introduce the difference between optical and confocal microscopy. Traditional optical microscopy illuminates the specimen over a wide area. It captures the reflected light into the eyepieces or detectors, including the signal from the focused plane of the specimen and the unnecessary light from the background and fluorescence emission. The unnecessary signal seriously reduces its resolution and contrast. While LSCM selectively captures the signal from the focused specimen and filters out unnecessary signals. LSCM can increase the image resolution and contrast of a micrograph

by using a spatial pinhole to block out-of-focus light in image formation. [76] The confocal microscopy only illuminates the focal plane of the specimen with a finely focused spot. Typically, the size of the illumination points ranges from approximately 0.25 to 0.8 micrometers in diameter (depending upon the objective numerical aperture) and 0.5 to 1.5 micrometers deep at the brightest intensity. [77]

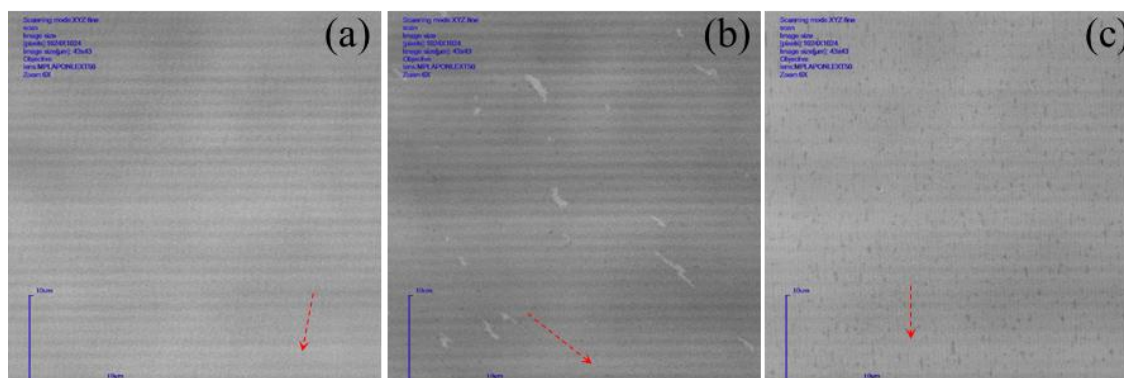


Figure 3.3 Typical images of (a) pure monolayer graphene, (b) monolayer graphene with bilayer patches (white area), and (c) monolayer graphene with a buffer layer (dark spots) in scale of $43 \times 43 \mu\text{m}^2$ by laser scanning confocal microscopy. The red arrows indicate the direction along the terraces. The horizontal stripes are the background signal of the confocal microscopy.

In this thesis, the LSCM is employed to evaluate the quality of epitaxial graphene after growth. It enables to distinguish the buffer layer, monolayer graphene, and bilayer graphene on a micrometer scale in a few seconds by the contrasts. Figure 3.3 depicts a typical image of epitaxial monolayer graphene on SiC. The LSCM image clearly distinguishes the buffer layer on SiC, the monolayer, and the bilayer graphene by the distinct contrasts. Figure 3.3 (a) shows a perfect monolayer graphene covered on SiC substrate at a scale of $43 \times 43 \mu\text{m}^2$ in confocal microscopy. The uniform color and contrast indicate a homogeneous distribution of the monolayer graphene across the entire area. Figure 3.3 (b) displays over 98 % coverage of monolayer graphene in the observed areas. Small white patches are the bilayer graphene. In these local sites, the graphene growth occurs at a faster speed, thus the bilayer graphene patches form. Figure 3.3 (c) presents another common occurrence: the co-existence of a monolayer graphene and a buffer layer. The buffer layer areas are visible as dark spots. This indicates an absence of monolayer graphene coverage in those areas due to a lower growth speed in those local spots.

3.2.2 Atomic force microscopy

Generally, the LSCM technique can only detect the different optical properties of the materials, e.g., the buffer layer and graphene layer. For higher resolution, it is recommended to use a scanning probe technique such as AFM. AFM is a basic technique in nanoscopic research and is frequently employed to display a sample's real space morphology or topography. The AFM has a similar measurement scale and resolutions comparable to SEM and transmission electron microscopy (TEM), yet with distinct applications. AFM can provide atomic-scale resolution (< 1 nm) in height (Z - axis) and a few nanometers resolution (< 10 nm) in lateral (X - / Y - axis) directions, depending on the size of the AFM tip.

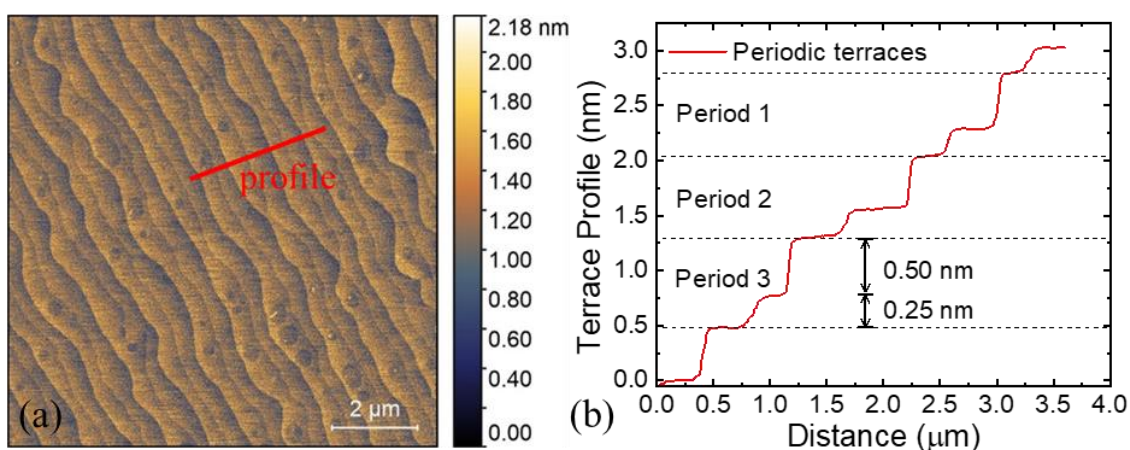


Figure 3.4 Typical topography image of monolayer epitaxial graphene, without any buffer layer and bilayer pitches in the detected area (a) AFM topography ($10 \times 10 \mu\text{m}^2$) of a PASG graphene layer grown at 1800°C for 6 min on a 6H-SiC (0001) substrate with a small miscut angle of -0.06° . (b) The periodic steps and terraces profile along the red indication line in (a). The ultrasmooth graphene exhibits periodic step heights of 0.25 nm and 0.50 nm.

The working principle of an AFM is scanning with a tip (or a probe) in close proximity to the sample surface. Typically, AFM can be used in two modes: contact mode or non-contact mode. The contact mode operates at small tip-sample distances in contact or intermittent contact and measures topography based on the short-range repulsive force, which may damage the tip and sample. [78] In this study, epitaxial graphene is investigated in the non-contact mode. This mode measures surface topography based on the attractive force, thereby preventing damage to the tip or sample. The interaction between the sample and the tip in AFM measurements can be controlled and limited to very low values, which renders the imaging typically non-destructive.

This thesis uses AFM to characterize the topography of a single layer of epitaxial graphene on SiC at the nanoscale level. In principle, a perfect monolayer epitaxial graphene exhibits atomic steps and terraces in period on SiC substrate, which are fingerprint information of monolayer epitaxial graphene. Figure 3.4 presents a typical topography image of monolayer epitaxial graphene in this thesis, without any buffer layer and bilayer pitches in the detected area. The AFM image in Figure 3.4(a) displays a typical ultra-smooth, bilayer-free graphene layer ($10 \times 10 \mu\text{m}^2$) on a SiC substrate. Figure 3.4(b) exhibits the periodic steps and terraces profile, which corresponds to the red indication line in (a). The ultra-smooth graphene on 6H-SiC substrate has periodic step heights of 0.25 nm and 0.50 nm, corresponding to one and two SiC crystal layers, respectively. The AFM measurement demonstrates that the monolayer graphene grown using the PASG method is of high quality and homogeneity on the micrometer scale.

3.3 Device fabrication

3.3.1 Optical Lithography

This study aims to develop practical graphene QHR standards for metrological applications. The device fabrication process should be cost-effective, efficient, reliable, and reproducible. More importantly, the $n\Omega/\Omega$ accurate QHR device must remain stable over a long period (years) and be user-friendly for easy access. To meet these requirements, we utilized a fabrication process based on ultraviolet (UV) lithography instead of electron beam lithography.

As previously described, monolayer epitaxial graphene was grown on a semi-insulating 6H-SiC(0001) SiC substrates ($10 \times 5 \text{ mm}^2$) using the so-called polymer-assisted sublimation growth (PASG) method. [71] The SiC wafer from *II-VI Comp.* has a nominal miscut of about -0.06° toward $[1\bar{1}00]$ and almost zero toward $[11\bar{2}0]$. The Hall bar devices were fabricated in PTB's clean room using standard UV lithography, reactive ion etching (RIE), thermal deposition, and wet etching (potassium iodide solution, *MicroChemicals TechniEtch AC12*). The sequence of the Hall bar fabrication steps is presented in Figure 3.5. To fabricate the Hall bar, a layer of metal was deposited directly onto the as-grown graphene surface, as illustrated in Figure 3.5 (a) – (b). The layer comprised a 20 nm PdAu alloy with a mass ratio of 60% Pd to 40% Au, followed by a 40 nm Au layer. This step aimed to prevent contact from organic photoresists or contaminants during the microfabrication process. Similar methods have been described in the literature. [79,80] During high temperature epitaxial growth, the graphene forms not only on the silicon face of the SiC but also uncontrollably on the side walls and the

3.3 Device fabrication

carbon face of the SiC. To fabricate the device for low-temperature transport measurement, it is necessary to fully etch away the graphene on the edge of the SiC substrate and only retain the graphene in the Hall channel.

Figure 3.5 (c) - (f) illustrates the initial UV lithography process. The gold on the edge was removed by the etchant TechniEtch™ ACI2 (wet etching), and the graphene on the edge was removed by RIE (dry etching), while the Hall channel was protected with gold. The second UV lithography process is shown in Figure 3.5 (g) – (i). The Ohmic contacts were formed on the SiC substrate by evaporating a titanium (10 nm)/gold (100 nm) layer with a small overlap to the PdAu/Au layer. Figure 3.5 (j) – (l) illustrates the third UV lithography process. The Au was removed from the graphene Hall channel by wet etching in TechniEtch™ ACI2 solution, while the Ohmic contact pads were protected with the photoresist. After dissolving the photoresist in acetone, the fabrication of the Hall bar device was completed, as presented in Figure 3.5 (m).

The Hall bars are 1600 μm in length and 400 μm in width. There are two contact pads for the source and drain, along with six contact pads for the voltage probes. The distance between the voltage probes is 400 μm . The geometry ratio of the Hall bar width to the distance between two neighboring contact pairs is 1:1 ($w = 400 \mu\text{m}$, $l = 400 \mu\text{m}$). The Hall bar is nearly perpendicular to the terrace steps. The contact resistances for all devices were measured by 3-terminal measurements at low temperatures (4.2 K) in the quantum Hall regime. The Ohmic contact resistances were measured to be less than 10 Ω , ensuring reliable high-accuracy QHR measurements. [41]

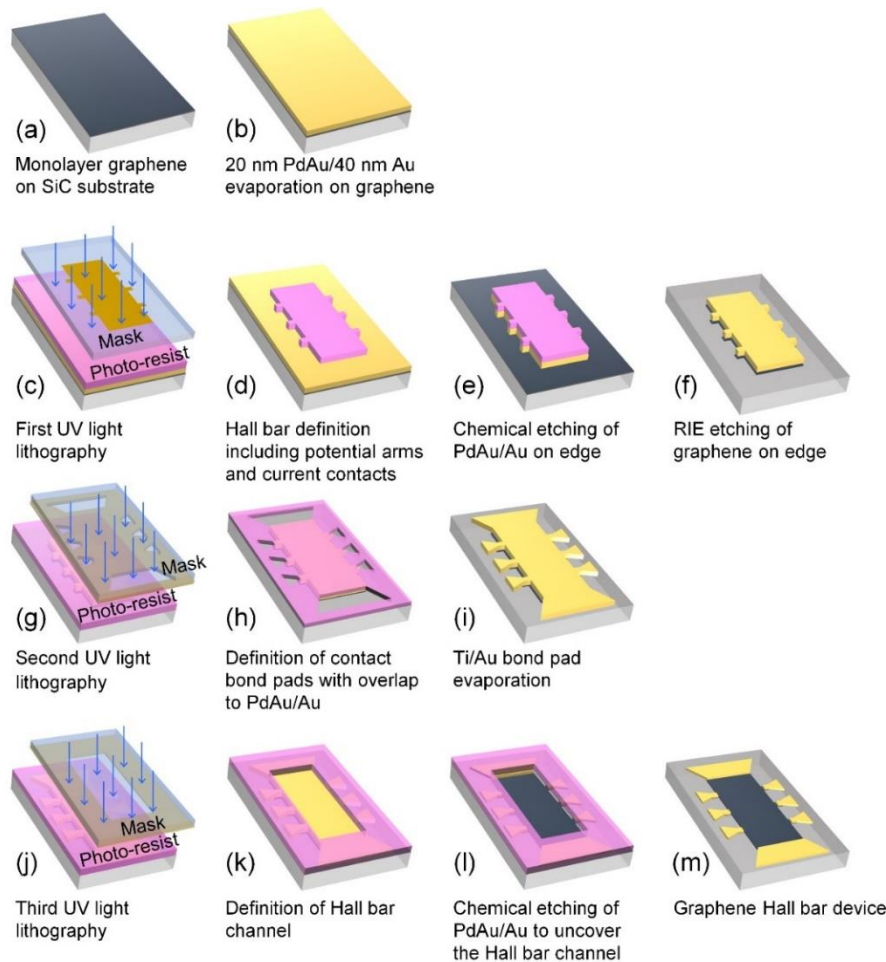


Figure 3.5 (a) Monolayer epitaxial graphene on SiC substrate (5 mm × 10 mm). (b) Thermal evaporation of 20 nm PdAu / 40 nm Au on the as-grown graphene surface. The precious metal layer prevents contact with organic photoresists during the microfabrication process. (c-d) First UV lithography step for Hall bar definition by wet/dry etching. (e) Chemical wet etching of the surrounding PdAu/Au layer by TechniEtch™ AC12, while the Hall bar channel is protected by photoresist. Afterward, the photoresist is removed by acetone and isopropanol. (f) RIE etching of the graphene on the edge and the backside of the substrate, while the graphene below the metal is protected. The Pd/Au layer forms the Ohmic contact with graphene at the potential arms and the current contact positions. The contact areas have a finger-like shape. (g-h) The second UV lithography step is for bond pad fabrication. (i) The bond pads are formed by thermal evaporation of a 10 nm Ti and 100 nm Au layer with an overlap to the PdAu/Au layer at the potential arms and current contacts. (j-k) Third UV lithography step for uncovering the graphene Hall bar channel. (l) Removal of the PdAu/Au layer on the Hall bar channel by TechniEtch™ AC12 wet-chemical etching. (m) Removal of the photoresist by acetone and isopropanol.

3.3.2 F4-TCNQ molecular doping technique

The as-grown epitaxial graphene exhibits a high electron density of 10^{13} cm^{-2} . [29] This thesis investigated a molecular doping technique using the electron acceptor of the F4-TCNQ molecule to compensate for the high electron density of as-grown epitaxial graphene. By precisely adjusting the dopant concentration, the carrier density was freely controlled in a wide range from the intrinsic *n*- to the *p*-type regime. After the molecular doping treatment, the fabricated quantum Hall devices are ready to use, and no further treatments are required.

Pre-annealing treatments

The as-grow epitaxial graphene on SiC has a very high initial electron density of $\approx 1 \times 10^{13} \text{ cm}^{-2}$ demonstrated by using the Hall measurements and angle-resolved photoelectron spectroscopy (ARPES) in an ultra-high vacuum. [29] During device fabrication, the wet etching (*MicroChemicals TechniEtch* ACI2) process reduces the initial electron density due to the *p*-type doping effect of the ACI2 solution. A similar *p*-type doping effect was reported in the references. [79,81] Our graphene Hall bar device without any co-polymer encapsulation has an electron density $\approx 1 \times 10^{12} \text{ cm}^{-2}$ at 300 K. The electron density at 4.2 K is slightly lower than $\approx 1 \times 10^{12} \text{ cm}^{-2}$. For the epitaxial graphene without any encapsulation, the electron density is slightly decreasing from $1.1 \times 10^{12} \text{ cm}^{-2}$ at 300 K to $9.9 \times 10^{11} \text{ cm}^{-2}$ at 4.2 K. This behavior is consistent with the result in other studies. [82]

To ensure a reproducible and controllable doping process, it is important to keep a consistent initial electron density in graphene prior to the F4-TCNQ doping process. This was accomplished by fabricating high-quality epi-graphene using the PASG method [71] and specific surface annealing procedures. After microfabrication of the graphene QHR device, the graphene surface was cleaned using two different annealing procedures. For each treatment, the chamber was pumped to 10^{-7} mbar for 12 hours. To investigate the different annealing procedures, one sample set was cleaned by annealing in a vacuum at 450 °C for 2 hours, and the other one was additionally annealed in a hydrogen atmosphere (1000 mbar) at 450 °C for another 2 hours. After the annealing procedures, the doping layer stacks were spin-coated onto the chip immediately.

Preparation of the dopant blend

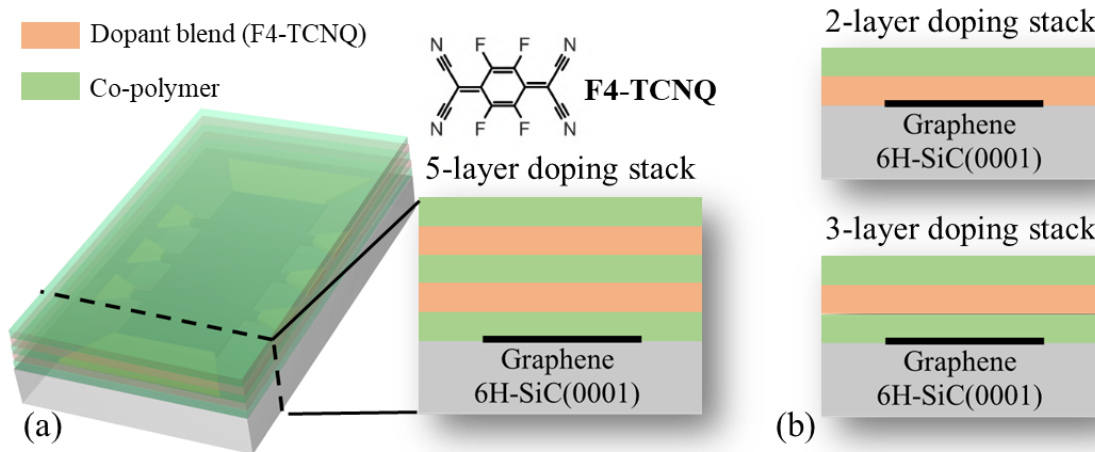


Figure 3.6 Schematic representation of 3D and 2D doping stacks on graphene-based QHR devices. The dopant blend is a mixture of F4-TCNQ, anisole, and 950 K PMMA. The copolymer is EL6 (MMA (8.5) MAA). (a) The 5-layer doping stack includes two layers of dopant blend, which are separated by three layers of copolymer. (b) The 3-layer doping stack includes one layer of dopant blend and two layers of co-polymer. The 2-layer doping stack has one layer of dopant blend, which is directly spin-coated onto the graphene surface without a spacer layer, and one layer of copolymer on top, which acts as encapsulation.

In contrast to the method of thermally evaporating the F4-TCNQ powder onto the graphene surface [83], we spin-coat the dopant blend and copolymer layers onto the graphene surface to tune the carrier density. The dopant blend is a mixture of F4-TCNQ, anisole, and 950K Polymethylmethacrylate (PMMA) (*MicroChemicals*). The F4-TCNQ molecule powder was bought from *Sigma-Aldrich*. The molecular doping mixture was produced by dissolving 25 mg of F4-TCNQ powder in 3 ml anisole. [75] By subsequent dilution of a portion of this mixture in 950K PMMA, four different doping concentrations were obtained with volume mixing ratios of F4-TCNQ/anisole to PMMA of 1%, 5%, 25%, and 50%. The copolymer layers were spin-coated on a graphene surface by using EL6 copolymer (MMA (8.5) MAA).

A five-layer doping stack is depicted in Figure 3.6(a). After the pre-annealing treatment, the doping stacks were spin-coated on QHR devices from the bottom to the top layer sequentially. After spin-coating, each layer was baked for 5 min at 160 °C (above the PMMA glass transition temperature) on the hot plate. Finally, twelve Hall bar devices with identical dimensions ($5 \times 10 \text{ mm}^2$) were fabricated in a single graphene chip using UV lithography, as shown in Figure 3.6(a). Following the same recipe, we also prepare the 2- and 3-layer doping stack graphene-based QHR devices, as shown in Figure 3.6(b).

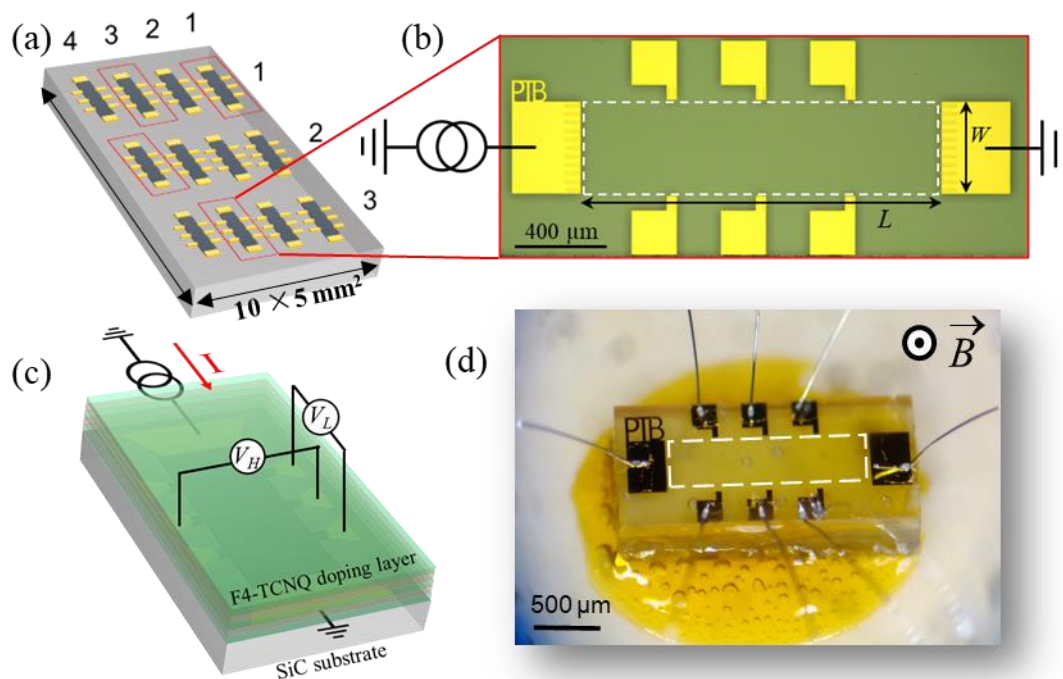


Figure 3.7 (a) Twelve identical graphene Hall bar devices with index numbers on SiC substrate ($5 \times 10 \text{ mm}^2$). (b) Optical microscopy image of a macroscopic Hall bar device with length $L = 1600 \mu\text{m}$ and width $W = 400 \mu\text{m}$. The white line indicates the area of monolayer epitaxial graphene. (c) The schematic diagram of F4-TCNQ doped graphene QHR device in Hall measurement. (d) The photo of a real device glued and wire-bonded on a TO-8 sample holder in optical microscopy.

The QHR devices presented in Chapters 4 and 5 included 5-, 3-, and 2-layer doping stacks. A very wide F4-TCNQ concentration in PMMA was tested to tune the carrier density of as-grown epitaxial graphene, including the volume ratios of F4-TCNQ/anisole to PMMA in the doping layer from 1% to 50%. Detailed information is presented in each chapter. The devices presented in Chapter 6 are 5-layer F4-TCNQ doping stack structures. The volume ratio of F4-TCNQ/anisole to PMMA in the doping layer is 25%. The spacer layer is EL6 copolymer (MMA(8.5) MAA).

3.4 Magnetotransport measurement at low temperatures

Twelve identical Hall bar structures are integrated into one graphene chip. After the device fabrication and molecular doping process, the chip was diced to obtain twelve individual graphene QHR standards. Each of them was mounted on its own TO8 chip carrier for subsequent characterization, including magnetotransport and high-accuracy measurements. The

graphene QHR standards were stored in a closed chamber with a mixture of N₂ and air at room temperature and ambient pressure.

Chapter 4 focuses on the magnetotransport measurement results of the F4-TCNQ doped graphene QHR devices. Chapter 5 focuses on the high-accuracy measurement results of the graphene QHR standards. Chapter 6 focuses on the realization of SI unit ohm under relaxed conditions. The following techniques were used for the magnetotransport experiment.

3.4.1 Cryogenic and electronic setup

- **Cryostats**

This section describes the setups for magnetotransport measurements of graphene QHR devices. To investigate the quantum transport phenomena, the devices need to be cooled down to cryogenic temperatures and subjected to a perpendicular magnetic field. The cryogenic setups are used to cool down the device and observe the quantum Hall effect in magnetic fields.

The magnetotransport measurements of the graphene QHR devices were performed in two different commercial cryostats. The first cryostat is a He flow cryostat with a variable temperature insert (VTI) from *Oxford Instruments NanoScience*. Here, temperatures can be varied from 1.4 K to 300 K. There are two thermometers (*Lake Shore Cernox* thin film sensors) in the cryostat to detect the temperature. One is used to detect the temperature in the needle valve. The other one is installed on the probe and is therefore very close to the sample. This thermometer can thus be used to detect the temperature of the sample during the cool-down process. In particular, this cryostat is equipped with a vector magnet in which a 3D-vector magnetic field can be applied up to 1 T, enabling rotational measurements with a fixed magnetic field along different planes. In addition, in the *z* direction (out-of-plane direction) a magnetic field up to 9 T can be applied. The interior of the cryostat is uncoupled from room temperature by several vacuum shields, a liquid nitrogen cooling shield (77 K), and a liquid helium cooling shield (4.2 K), the so-called main bath. The lower temperature (1.4 K) is achieved by controlling the needle valve and pumping the liquid helium in the sample space. Temperature-dependent transport measurements were performed on this VTI cryostat.

The second cryostat is a commercial bath cryostat with a superconducting magnet, which can generate fields up to 12 T at 4.2 K. In the bath cryostat, the sample is immersed in liquid helium. Therefore, the temperature is 4.2 K. This cryostat is integrated into the high-accuracy measurement system, and the high-accuracy measurements were performed in this bath cryostat.

- **Electronic setup**

The QHR devices were glued to standard TO-8 chip carriers and electrically connected using Al wire bonding. The chip carrier was mounted on a sample rod electrically connected to the outside of the cryostat and connected to a switch box to further connect the measuring equipment. Near the chip carrier, the Cernox thermometer was installed so that the real temperature of the device could be measured.

The standard procedure for Hall measurements is to apply a constant current from the source (drain) side and to measure the voltage in a four-probe configuration. Magnetotransport measurements were performed using *Keithley 6220* current sources, *Keithley 2182* nanovoltmeters, *Adret 103A* DC sources, and *HP 3458A* multimeters.

3.4.2 Ohmic contact resistance

For QHR standards in highly accurate measurements, the quality of ohmic contacts is critical. First, the quality must be high such that the measurements are not affected by the contact resistance. Second, the contacts must be robust because the quantum Hall resistors which are routinely used over periods of years must withstand numerous thermal cycles between room and cryogenic temperatures. [84] A low contact resistance R_C is essentially important for applications in metrology, where a QHR standard should have contact resistances at least below 10Ω , but ideally much lower, in order to not influence the accuracy of quantization. [41]

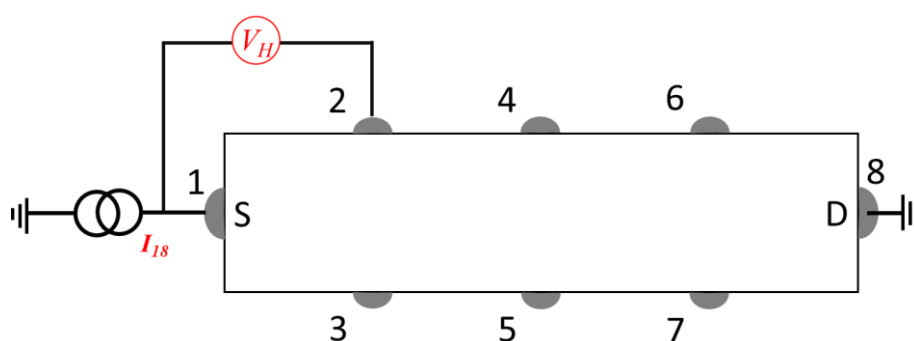


Figure 3.8 The schematic of a three-point measurement to determine the contact resistance.

For the graphene QHR standard, the Ohmic contacts were evaporated on the graphene/SiC substrate using titanium (10 nm)/gold (100 nm) layer with a small overlap to the PdAu/Au layer. The detailed processes are described in Section 3.3. The contact resistance does not depend on the current (as long as the current stays below its breakdown value. This contacting technique

has been very intensely used for resistance standards without showing any time deterioration over a period of 3 years.

The three-point measurement is used to check the contact resistance in the quantum Hall regime. The magnetic field B is first adjusted to a value corresponding to the well-quantized Hall resistance at filling factor 2. The current should be in the same order as that used for the QHR measurements. For instance, to evaluate the resistance of contact 1, the measuring current is passed through contact 1 and 8, and the potential difference between contact 1 and 2 is measured. Therefore, the contact resistance R_{C1} is determined in this measurement, as shown in Figure 3.8.

The contact resistances of the graphene QHR devices were measured by three-terminal measurements at low temperatures (4.2 K) in the quantum Hall regime. The graphene QHR devices are subjected to magnetic fields above 4 T at an applied current of 10 μA . The contact resistances were checked to less than 1 Ω , which is below the recommended maximum value of 10 Ω as given in the guidelines for quantum Hall metrology. [41]

3.4.3 Hall measurements

By Hall measurement in low magnetic fields, the electrical properties of graphene QHR devices, such as sheet resistance, carrier density, and carrier mobility, can be determined. In this thesis, Hall measurements were carried out in cryostat at a temperature of 4.2 K to determine the sheet resistance ρ_{xx} , carrier density n , and carrier mobility μ . The zero-field ($B = 0$) carrier density n was calculated from the slope of the Hall resistance curve $R_{xy}(B)$ in a low magnetic field using the classical Hall equation $n = \Delta B / (e \cdot \Delta R_{xy})$. The Hall mobility is then calculated from the zero-field resistivity ρ_{xx} and carrier density n , using the formula $\mu = 1 / (e \cdot n \cdot \rho_{xx})$.

3.5 High-accuracy measurements

3.5.1 Principle of current-reversal measurement

The method of current-reversal measurement can measure the longitudinal resistance within the uncertainty of ± 2 m Ω with an applied current of 50 μA . The longitudinal resistances $R_{xx} = \rho_{xx} l / w$ were determined from the mean value from the measurement with both current polarities. Thus, with this technique, thermoelectric effects or any instrumental offsets were safely canceled, while the information was still available to account for current path-dependent effects.

Thermoelectric voltages (thermoelectric EMFs) are generated by thermal differences between the junctions of dissimilar metals. Widely varying temperatures within the circuit can also create thermoelectric voltages. A few microvolts of thermal voltages can be generated by temperature gradients in the test circuit caused by fluctuating temperatures in the lab. These voltages can be large compared to the signal that the nanovoltmeter is trying to measure. Thermoelectric voltages can cause the following results: 1) instability or zero offset that is above acceptable levels, and 2) the reading is sensitive to (and responds to) temperature changes. The latter can be demonstrated by touching the circuit, by placing a heat source near the circuit, or by a regular pattern of instability.

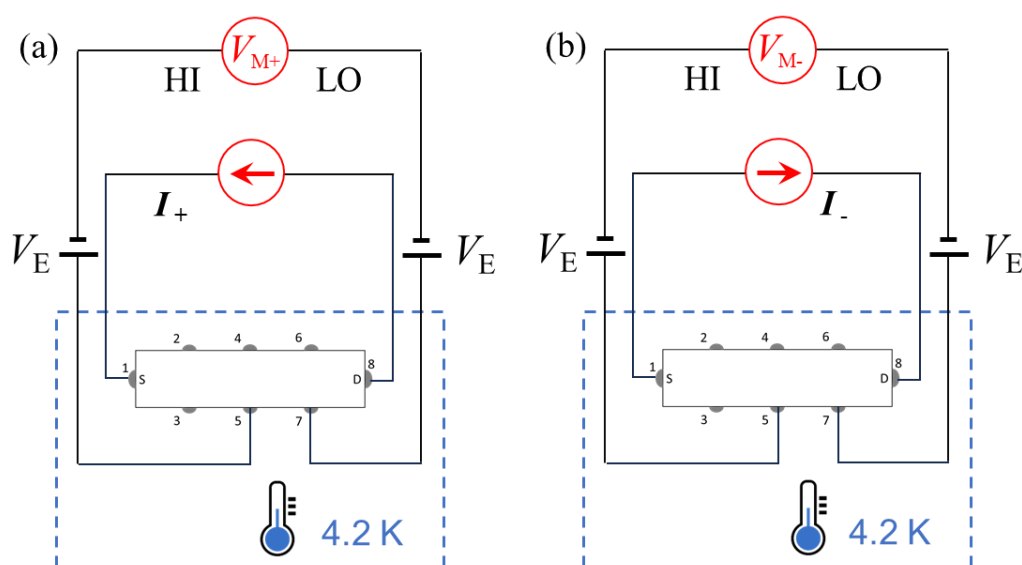


Figure 3.9 The schematic of the current-reversal measurement with (a) positive and (b) reversal current applied to measure the longitudinal resistance in the quantization regime.

The current-reversal measurement is a technique to accurately measure a very small resistance on the level of milliohm. This technique is used to reduce or eliminate thermoelectric voltages. In this study, all the transport measurements were performed at cryogenic temperatures. The devices were cooled down to the liquid helium temperature, while the electronic instruments for the signal detection and acquisition were kept at room temperature. The electronic wires connected the cold devices and warm electronic instruments. Therefore, there is a big temperature gradient in the electronic wires, which can cause thermoelectric voltages in the resistance measurement.

Thermoelectric voltages can be canceled out by making two measurements with currents of opposite polarity, as shown in Figure 3.8. With the positive current applied as in Figure 3.8 (a), the measured voltage is:

$$V_{M+} = 2V_E + IR_{57} \quad (3.4)$$

reversing the current polarity as shown in Figure 3.8(b) yields the following voltage measurement:

$$V_{M-} = 2V_E - IR_{57} \quad (3.5)$$

The two measurements can be combined to cancel thermoelectric voltages:

$$V_M = (V_{M+} - V_{M-})/2 = [(2V_E + IR_{57}) - (2V_E - IR_{57})]/2 \quad (3.6)$$

The measured resistance is computed in the usual manner:

$$R_{57} = V_M / I \quad (3.7)$$

3.5.2 Principle of the CCC bridge

A cryogenic current comparator (CCC) is used in electrical metrology to compare ratios of two electrical currents with the highest precision. This instrument exceeds the accuracy of other current comparators by several orders of magnitude for the use of high-accuracy measurements of resistances. The CCC can be considered as an ideal direct current (DC) transformer. The operating principle is based on the use of the Meissner effect in a superconducting screen which surrounds current-carrying coils of different turns, and on the use of a Superconducting Quantum Interference Device (SQUID) as a null detector for the magnetic field near the screen. Both are based on the effects of superconductivity and therefore require very low temperatures, typically supplied by liquid helium (4.2 K). For the operation of CCC in resistance bridges, specially designed synchronized dual current sources are needed.

The simplified CCC bridge circuit for high-accuracy measurement is schematically shown in Figure 3.10. Two isolated current sources, ‘Master’ and ‘Slave’, separately drive current through QHR and 100Ω resistors and associated windings N_1 and N_2 on the CCC. The 100Ω resistor is a calibrated reference with high accuracy. The most important precondition for a successful measurement is a stable, reliable, and highly accurate reference resistor. The current ratio can be set via electronics to a few parts in 10^6 , and this ratio is improved to a level of 1 part in 10^{11} by forming a negative feedback loop from the SQUID sensing the net flux in the CCC to the Slave current source. When balanced, the reading on the nanovoltmeter is exactly

proportional to the resistance ratio. [85] The main uncertainty components of the bridge are the noise of the SQUID sensor, the Johnson noise of the resistors being measured, and the current and voltage noise of the null detector. These components combine to give a typical measurement uncertainty of 1 part per billion (ppb) for a measurement time between 5 to 15 min. [85]

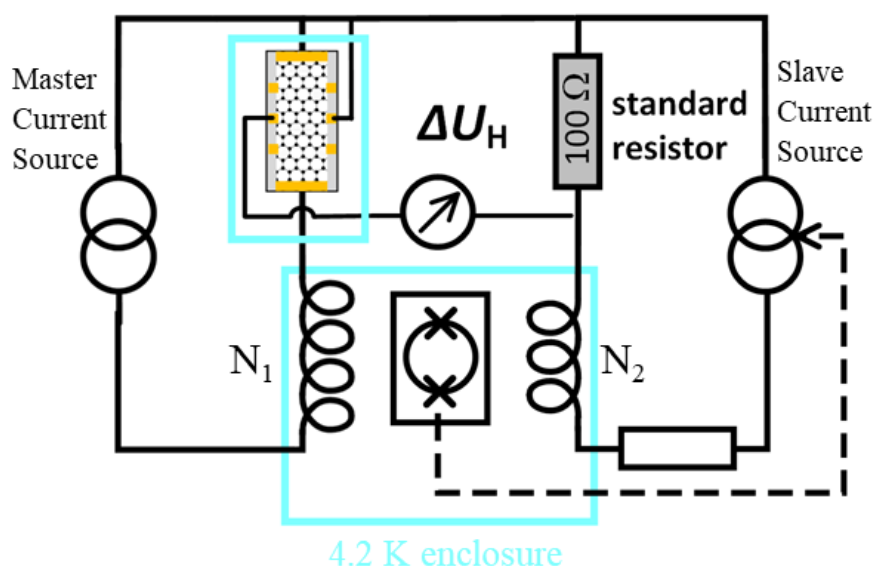


Figure 3.10 Schematic wiring diagram of the CCC resistance bridge used for the precision quantum Hall measurements. The voltage ΔU_H is the difference between the Hall voltage of the QH device and the voltage across a 100Ω reference resistor, which was calibrated against the quantized value $R_K/2$ of a conventional GaAs-quantum Hall resistance standard. The QH device and the CCC are cooled to cryogenic temperature of 4.2 K, indicated by a light blue rectangle. The 100Ω resistor (reference resistor) is kept at a constant temperature close to room temperature. Uncertainties attached to the reference resistors are considered in the type B uncertainty of the resulting QH resistance values. Adapted from Ref. [51]

In principle, the value of the quantized Hall resistance is exactly $h/\nu e^2$ when the magnetic field is set to integer filling factor ν . However, in practice, many possible effects can cause the Hall resistance to deviate from exact quantization. Unwanted dissipation in the QHE is the main factor that causes the deviation. [85] For instance, if ρ_{xx} is not exactly zero, the Hall device is not in the non-dissipative state, and R_{xy} will deviate from exact quantization. Also, if the contact resistances of the graphene are too large (typically $\geq 10 \Omega$), excessive dissipation will occur at the contacts, resulting in errors in R_H . Over the last two decades, the metrological community has evaluated all possible errors in the QHE and composed a set of experimental guidelines for the measurement uncertainty smaller than 1 ppb. [41,84] In this thesis, the high-accuracy

measurements of the graphene QHR standards were performed following the established guidelines. [41]

3.5.3 High-accuracy measurements

The graphene QHR standards are cooled down using a commercial He-4 bath cryostat with a magnetic field of up to 12 T and a temperature of 4.2 K. The high-accuracy measurements of the graphene QHR standards were performed through indirect comparison with a well-characterized GaAs QHR standard via an intermediate 100 Ω resistor. The traceability to the quantized value $R_K/2$ of the GaAs QHR standard allows for precise determination of the quantum Hall resistance R_{xy} of the graphene device under test [86], where $R_K = h/e^2$ is the von Klitzing constant. The Hall resistance R_{xy} were carried out at $T = 4.2$ K and $I = 38.7$ μ A using a commercial cryogenic current comparator (CCC) resistance bridge from *Magnicon GmbH*. The balancing of the bridge is realized by compensating for the current-induced magnetic flux of both arms of the CCC bridge, which is detected by a sensitive DC SQUID in a cryogenic environment. The remaining Hall voltage difference ΔU_H is a direct measurement of the deviation from the $R_K/2$ value, as shown in Figure 3.10. The Hall resistance R_{xy} was determined by the CCC bridge. The relative deviation $(R_{xy} - R_K/2) / (R_K/2)$ of the QHR value from the nominal resistance value $R_K/2$ has a typical accuracy of ≈ 2.5 n Ω/Ω ($k = 2$), which is limited by the calibration and stability of the 100 Ω resistor. For the current-dependent measurements at $I = 155.0$ and 232.5 μ A (highest accessible currents in the setup), an intermediate 10-k Ω resistor was used in the CCC bridge. The longitudinal resistance ρ_{xx} is determined by two individual resistance measurements using the CCC resistance bridge. The longitudinal resistance ρ_{xx} is calculated as the difference of the Hall resistance of diagonal and orthogonal contact pairs. [86]

Statistical Analysis

In the case of the precision QHR measurements using the CCC resistance bridge, combined extended type A and type B uncertainties ($k = 2$) were considered. Table 3-1 summarizes the uncertainties involved in R_{xy} measurements with the CCC bridge. The typical type A uncertainty of the bridge voltage difference is ≤ 0.6 nV/V (≤ 0.2 nV/V) for the typical total measurement time of 5 min (15 min) with a sample count/number of measurement cycles of $N = 12$ ($N = 48$). The combined uncertainty assigned to the calibration value of the 100 Ω reference resistor is about 1.21 n $\Omega \Omega^{-1}$. The mean value and the standard deviation (Type A uncertainty) are calculated by the measurement bridge software. Typical combined

3.5 High-accuracy measurements

uncertainties (type A and B) of the bridge are $1.25 \text{ n}\Omega\Omega^{-1}$ ($k = 1$) and combined expanded uncertainties of $2.60 \text{ n}\Omega\Omega^{-1}$ ($k = 2$). The main contribution to type B uncertainty arises from uncertainties attached to the 100Ω reference resistor. [50]

Table 3-2 summarizes the sources and contributions of uncertainties for R_{xx} measurements with the *Magnicon* CCC resistance bridge. The longitudinal resistance measurements with the CCC are determined from the difference of two individual Hall measurements with $N = 12$ samples/measurement cycles. A type B uncertainty due to the drift of the 100Ω resistor is $6.5 \mu\Omega$. The resulting combined expanded uncertainty of the longitudinal resistance is typically about $\pm 18.0 \mu\Omega$ ($k = 2$) for measurements inside the resistance plateau ($R_{xx} \approx 0$) where the noise level is low.

Table 3-1. Uncertainty sources and their contributions for R_{xy} measurements with the CCC resistance bridge.

Quantity i	Unc. type	$u_i \text{ n}\Omega/\Omega$
Typical stability of 100Ω resistor calibration value ($k = 1$)	B	1.17
Typical type A measurement uncertainty of 100Ω resistor ($k = 1$)	A	0.30
Syst. Errors of CCC for measurement chain R_{xy} - 100Ω -reference QHR ($k = 1$)	B	<0.10
Typical type A measurement uncertainty of R_{xy} ($k = 1$)	A	<0.55
Typical combined expanded uncertainty of R_{xy} ($k = 2$)	C	<2.60

Table 3-2. Uncertainty contributions and sources for R_{xx} measurements with the CCC resistance bridge.

Quantity i	Unc. type	$u_i \mu\Omega$
Type B uncertainty due to 100Ω reference resistor drift ($k = 1$)	B	<6.5
Typical type A measurement uncertainty ($k = 1$)	A	<9.5
Typical combined expanded uncertainty of R_{xx} ($k = 2$)	C	<18.0

3.5.4 Definition of deviation regime and quantization regime

Due to the Fermi level pinning in epitaxial graphene, the epitaxial graphene exhibits a very wide Hall plateau ($\nu = 2$) in magnetic fields. This thesis presents high-accuracy measurement results that identify a deviation regime and a quantization regime in the wide Hall plateau, which were not previously discussed in graphene- and GaAs-based QHR standards in the literature. The investigation of the deviation regime in the Hall plateau is important for further

understanding of the QHE in epitaxial graphene and its application to resistance standards. In the deviation and quantization regimes, the longitudinal resistances exhibit a minor difference in the level of micro-ohms, which is identified through high-accuracy measurements. The minor difference in the longitudinal resistance is used to distinguish the boundary between the deviation and quantization regimes. This definition was applied to all the high-accuracy measurements of the graphene QHR standards discussed in Chapters 5 and 6.

The QHE theory states that the quantum Hall resistance R_{xy} in a magnetic field corresponds to zero longitudinal resistance. Consequently, the reliable determination of the quantum Hall resistance can be realized through the measurement of zero longitudinal resistance. In this study, we thus determine the so-called “quantization regime” using the criterion $|\rho_{xx}| = 0 \mu\Omega$ within the uncertainty of $\pm 18.0 \mu\Omega$ ($k = 2$), ensuring a relative deviation of R_{xy} from $R_K/2$ with an accuracy of $(R_{xy} - R_K/2) / (R_K/2) \leq (2 \pm 3) \text{ n}\Omega/\Omega$ ($k = 2$). The determined criterion is in accordance with the recommended guidelines for the use of GaAs QHR standards. [41] $|\rho_{xx}| = 0 \mu\Omega$ is a rather conservative criterion to determine the quantization regime. For a given QHR standard with a small s parameter, the relative deviation $(R_{xy} - R_K/2) / (R_K/2)$ could still be within $(2 \pm 3) \text{ n}\Omega/\Omega$ in metrology, even though the longitudinal resistance increases to a few hundred $\mu\Omega$, which will be discussed in Chapter 6. The measured value of the relative deviation $(R_{xy} - R_K/2) / (R_K/2)$ serves as a parallel experiment to evaluate the quantization accuracy of the QHR standard. The quantization regime can be validated by the measured value of $(R_{xy} - R_K/2) / (R_K/2)$.

It is imperative to underscore the following points. 1. The method of measuring the longitudinal resistance ρ_{xx} is independent of the accuracy of the nominal well-characterized GaAs QHR standard due to its value being determined by calculating the difference between the measured Hall resistance of diagonal and orthogonal contact pairs. 2. The high-accuracy measurement of Hall resistance R_{xy} is dependent on the accuracy of the nominal GaAs QHR standard, as its value is compared to the nominal well-characterized GaAs QHR standard via the 100Ω resistor, as previously mentioned. The aim of resistance metrology is to provide a primary standard that is not dependent on any other resistance. Accordingly, in this study, a conservative criterion was selected to determine the quantization regime. The criterion $|\rho_{xx}| = 0 \mu\Omega$ guarantees the relative deviation of the R_{xy} from $R_K/2$ with an accuracy of $\leq (2 \pm 3) \text{ n}\Omega/\Omega$ ($k = 2$).

Chapter 4. F4-TCNQ Molecular doping in epitaxial graphene

The unique properties of epitaxial graphene grown on an insulating SiC substrate make it attractive for electronic applications, particularly in the field of quantum resistance metrology. However, its high intrinsic *n*-doping and difficulty in controlling its carrier density present significant challenges for electronic applications. Different research groups used F4-TCNQ powder to tune the carrier density of epitaxial graphene. However, the doping effect was not stable because the powder is mobile on the graphene surface in the air. In addition, only *n*-type epitaxial graphene was achieved by the deposition of F4-TCNQ powder. In 2019, a research team at Chalmers University of Technology developed a method to tune the carrier density, in which the F4-TCNQ powder was dissolved in anisole and mixed with PMMA. The mixture of F4-TCNQ and PMMA exhibits high doping efficiency and very stable doping properties.

This thesis further developed the F4-TCNQ molecular doping technique to control the carrier density of epitaxial graphene with high precision and reliability over a very broad range. By precise adjustment of the concentration of F4-TCNQ in PMMA, the carrier density of epitaxial graphene has been successfully controlled to the desired values, spanning from intrinsic *n*-type to *p*-type regimes. The transport scattering mechanisms in epitaxial graphene at cryogenic temperatures were investigated. Based on the experiment and simulation results, a doping model and an energy band alignment picture were established to explain the molecular doping process of the F4-TCNQ accumulated on the graphene surface.

The majority of the content in this chapter has been previously published in Ref. [51]. Most of the graphene films on SiC used in this chapter were produced by Dr. Davood Momeni and Dr. Atasi Chatterjee. The simulation results presented in Section 4.6 were conducted by Stefan Wundrack. We would like to acknowledge the fruitful discussion and insightful comment provided by Prof. Dr. Thomas Seyller on the proposed energy band alignment picture.

4.1 Introduction

Epitaxial graphene is a promising material for the fabrication of future electronic devices due to its uniform and ordered growth on an insulating silicon carbide SiC substrate. It has excellent material properties, including high electronic and thermal conductivity. Moreover, it can be grown on large-scale SiC wafers and processed without the need for transfer to another substrate. [87,88] The two-dimensional hexagonal carbon lattice has a linear band structure

(Dirac cone) near the K -point, which enables high mobility of electrons and holes, known as massless relativistic Dirac fermions. This also allows for the observation of the quantum Hall effect (QHE) at room temperature. [43] To develop electronics based on epitaxial graphene, it is crucial to reliably control the carrier density from n - to p -type regimes over a wide range. This is because as-grown epitaxial graphene has a considerably high n -type carrier density of up to 10^{13} cm⁻². [29] The goal of this chapter is to find a solution to precisely reduce the carrier density to the charge-neutrality point and further into the p -type regime.

Various approaches exist to reduce the carrier density in epitaxial graphene. These include traditional substitutional doping, such as metal atom adsorption (e.g., gold or antimony). [89] However, this method inevitably introduces additional charge impurities, which greatly increase the scattering centers and negatively affect conductivity. [90] Other methods, such as electronic gating [91], corona discharge [92], and photochemical gating [93] have also been reported to reduce carrier density. Molecular doping with acids, such as diluted aqua regia or nitric acid, in combination with annealing processes [79,81,94] [95], fluorinated fullerenes [96], and oxygen adsorption [97,98] have successfully reduced electron density. Functionalization of graphene with chromium tricarbonyl provides a gateless and reversible method for tuning the carrier density. [99,100] However, most of these techniques do not allow for permanent tuning of the electronic properties or require adjustment in the user's laboratory. The stability of doped graphene layers can be improved by applying passivation layers of PMMA, [93,98] dielectrics, [101] hexagonal boron nitride layers, [102,103] perylene [104] or glass encapsulation. [105]

The molecule 2,3,5,6-tetrafluor-7,7,8,8-tetracyan-chinodimethan (F4-TCNQ) is an electron acceptor, and its electron affinity (~ 5.35 eV) is much larger than epitaxial graphene (4.3 eV). [96] Previous experiments have demonstrated that the F4-TCNQ molecules significantly reduces the electron density of graphene through a charge transfer mechanism. [83,106–108] The F4-TCNQ powder was deposited onto the epitaxial graphene surface by thermal evaporation. This method reduces the carrier density of epitaxial graphene from its intrinsic value to the charge neutrality point in the n -type regime. However, the evaporation of F4-TCNQ powder on the graphene surface does not enable tuning the carrier density beyond the charge neutrality point towards the p -type regime. [83] Furthermore, the doping effect is unstable due to the desorption of the F4-TCNQ powder from the graphene surface. [83] Recent investigations have shown that the combination of F4-TCNQ/PMMA doping stacks on epitaxial graphene can tune the carrier density to p -type. [109] However, achieving precise tuning of the

carrier density over a wide range - from the as-grown value to the desired p -type regime - remains a challenge. This is of great importance for the development of graphene-based electronic devices. For instance, a graphene-based QHR standard requires optimal carrier densities on the order of 10^{11} cm^{-2} . [110]

4.2 Concentration-dependent F4-TCNQ doped epitaxial graphene

In this section, we investigated the concentration-dependent F4-TCNQ doping in the 5-layer doped QHR devices. Data from the three groups of chips with different pre-annealing treatments and F4-TCNQ doping ratios are summarized in Table 4-1. The 1-layer doping stack is a copolymer layer encapsulated on the graphene surface. The first group of devices was prepared with the directly spin-coated doping layer without any pre-annealing treatment. The second group of devices was vacuum annealed before molecular doping. The third group of devices was annealed in a hydrogen atmosphere before molecular doping, as described in section 4.4.

Table 4-1. Characteristics of the graphene Hall bar devices with F4-TCNQ concentrations, pre-annealing treatment, and layers of doping stack. One device was post-annealed at 150 °C for 11 hours in a helium atmosphere after the first measurement. Charge carrier density and mobility were determined from the magnetotransport measurements at 4.2 K. Adapted from the reference [51].

Volume ratio	Pre-annealing	Doping stack	Carrier density [cm^{-2}]	Mobility [$\text{cm}^2\text{V}^{-1}\text{s}^{-1}$]
0:100	no	1L	2.40×10^{11}	6670
50:100	no	5L	-1.96×10^{10}	17280
0:100	vacuum	1L	5.83×10^{11}	5010
1:100	vacuum	5L	3.61×10^{11}	7280
5:100	vacuum	5L	2.22×10^{11}	8260
25:100	vacuum	5L	9.83×10^{10}	8880
50:100	vacuum	5L	6.69×10^9	48090
	same device, post-annealed		9.26×10^{10}	9970
0:100	H ₂	1L	7.12×10^{11}	4290
1:100	H ₂	5L	5.32×10^{11}	6290
5:100	H ₂	5L	2.70×10^{11}	4520
50:100	H ₂	5L	3.17×10^{10}	24240

Three reference devices were fabricated to determine the initial carrier density of the undoped graphene (volume ratio = 0:100), which was spin-coated with only one layer of copolymer to protect the graphene surface. For the reference device without pre-annealing treatment, a very low electron density ($n_e = 2.4 \times 10^{11} \text{ cm}^{-2}$) was observed from the quantum Hall measurement at 4.2 K due to the aqua regia (a mixture of nitric acid and hydrochloric acid) doping effect during the device fabrication process. [82,84,95] The other two reference devices were vacuum and hydrogen annealed, as described above. The higher electron densities of the annealed devices ($n_e = 7.12 \times 10^{11} \text{ cm}^{-2}$) are attributed to the removal of ambient gas molecules and impurities from the graphene surface, compared to that of the non-annealed devices. The best cleaning is achieved by annealing in a hydrogen atmosphere, resulting in the highest electron density.

One device (50% doping ratio, vacuum annealed, 5L) was post-annealed at 150 °C for 11 hours in a helium atmosphere after magnetotransport measurement (denoted post-annealed in Table 4-1). By post-annealing treatment, the electron density increases from $6.69 \times 10^9 \text{ cm}^{-2}$ to $9.26 \times 10^{10} \text{ cm}^{-2}$, as presented in Table 4-1.

The concentration-dependent molecular doping in epitaxial graphene has been studied using low-temperature magnetotransport measurement. Figure 4.1 displays the Hall resistance R_{xy} and the longitudinal resistivity ρ_{xx} , respectively, as plotted by varying doping ratios on vacuum-annealed devices. The Hall slope steadily increases around zero magnetic fields, revealing a reduction of the electron density within the graphene. The findings suggest that the electron density decreases as the doping concentration increases, indicating successful doping. Table 4-1 shows the corresponding data. The electron density gradually decreases from the initial value of $n = 5.8 \times 10^{11} \text{ cm}^{-2}$ in undoped graphene to $n = 6.7 \times 10^9 \text{ cm}^{-2}$ as the F4-TCNQ doping concentration increases. These results underline the compensating character of molecular doping.

The Hall plateaus at filling factor 2 are observed at high magnetic fields, as shown in Figure 4.1 (a). As the doping concentration increases, the onset of the plateaus gradually shifts to lower magnetic fields. At the highest doping level (50 % F4-TCNQ volume mixing ratio), an onset at $\approx 0.2 \text{ T}$ is observed (inset of Figure 4.1). The shallow bump at the onset of the R_{xy} plateau is related to variations in the Hall angle, causing a minor contribution to the longitudinal resistance. Even at a temperature of 4.2 K, the $\nu = 6$ plateau appears clearly for the weakly doped and undoped devices.

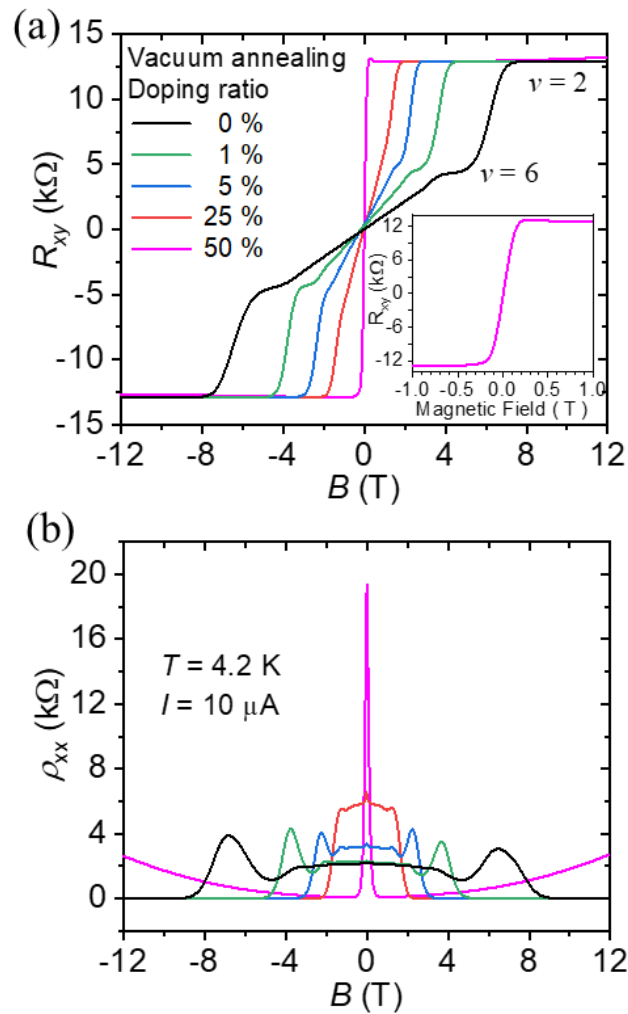


Figure 4.1 (a) Standard Hall resistance measurements of the graphene-based Hall devices with different F4-TCNQ doping mixing ratios (5L doping stack) and one undoped device. The graphene surface was cleaned by vacuum annealing. The measurements show a gradual shift of the onset of the Hall plateau with an increasing doping level. The inset shows the low magnetic field range of the device with a 50% doping ratio and the resistance plateau starting at about 0.25 T. The shallow bump is attributed to longitudinal resistance contributions at non-ideal Hall angles. (b) Measurements of the longitudinal resistivity ρ_{xx} of the same device set. Adapted from the reference [51].

Additionally, with increasing doping concentration, the longitudinal resistivity $\rho_{xx} \approx 0$ is observed at the lower magnetic fields in Figure 4.1 (b), which is accompanied by the shift of the onset of the quantum Hall plateau. Moreover, the highly symmetric B -field dependence of the ρ_{xx} and R_{xy} curves in both magnetic field directions indicates a highly uniform carrier

4.2 Concentration-dependent F4-TCNQ doped epitaxial graphene

density distribution for the different F4-TCNQ doping concentrations in combination with PASG graphene.

Note that the device with the lowest carrier density does not exhibit a flat ρ_{xx} minimum, corresponding to the Hall resistance deviating from the quantized R_{xy} value, as shown by the pink curves in Figure 4.1 (b). The significant increase in longitudinal resistance is symmetrical for the magnetic field directions. The increase in longitudinal resistance is due to the fact that the 0th Landau band is not completely filled with a very low carrier density. [111]

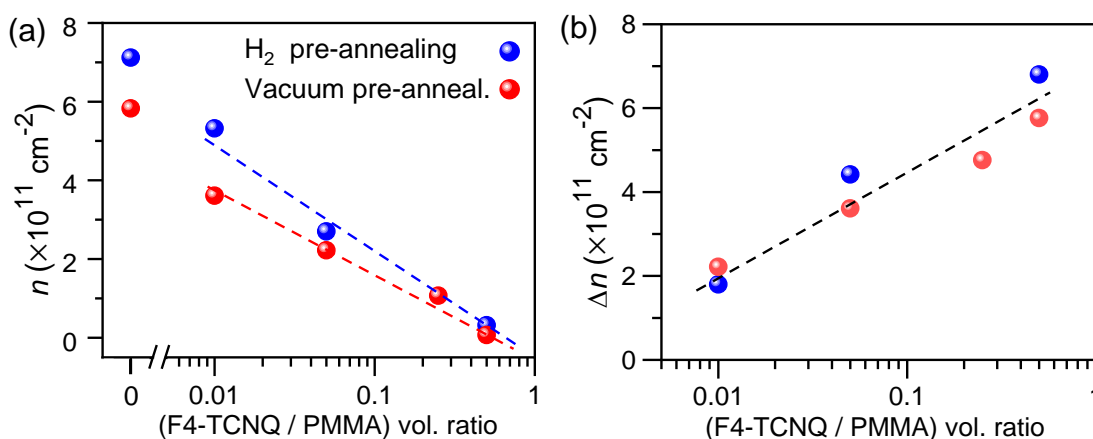


Figure 4.2 (a) The electron density n of the F4-TCNQ doped graphene Hall bar devices (5L doping stack) is a function of the F4-TCNQ/anisole volume concentration in PMMA for both sample sets (graphene pre-annealing in vacuum and hydrogen atmosphere). The differences at weakly doping levels between both sample sets indicate the impact of the different initial carrier densities of the undoped graphene. (b) The compensated carrier density, $\Delta n = n_{\text{undoped}} - n_{\text{doped}}$, shows a sublinear increase as a function of the F4-TCNQ volume concentration. Adapted from the reference [51].

From the two sets of devices with different doping ratios, we can evaluate the carrier density as a function of volume ratio (F4-TCNQ/anisole: PMMA). The plots in Figure 4.2 (a) and the data in Table 4-1 show that by gradually increasing the doping ratio up to 50 %, the electron density can be reduced by about two orders of magnitude. The semi-logarithmic plot of the data in Figure 4.2 (a) shows a sub-linear decrease in the carrier density in the graphene layer with increasing volume concentration of F4-TCNQ. This implies a high doping efficiency of F4-TCNQ at low concentrations and a moderate doping efficiency at high concentrations. This can be seen more clearly in Figure 4.2 (b), where the difference in carrier density between the doped and the undoped devices, $\Delta n = n_{\text{undoped}} - n_{\text{doped}}$, is plotted as a function of volume ratio. The corresponding plot in Figure 4.2 (b) shows a logarithmic increase in Δn . This result reveals a

sub-linear behavior of the electron transfer as a function of the F4-TCNQ volume concentration. Furthermore, the sub-linear behavior indicates a self-limiting effect with increasing doping concentration. In conclusion, the above results demonstrate a highly reproducible concentration-dependent doping technique and thus offer a new way to tune the carrier density of epitaxial graphene easily and reliably.

At low doping ratios, the difference in carrier densities between two sets of devices is due to the different initial carrier densities, which will be discussed in the next section. This result underlines the importance of preparation of the graphene surface to obtain reproducible starting conditions.

4.3 Decisive influence of graphene's initial charge carrier density

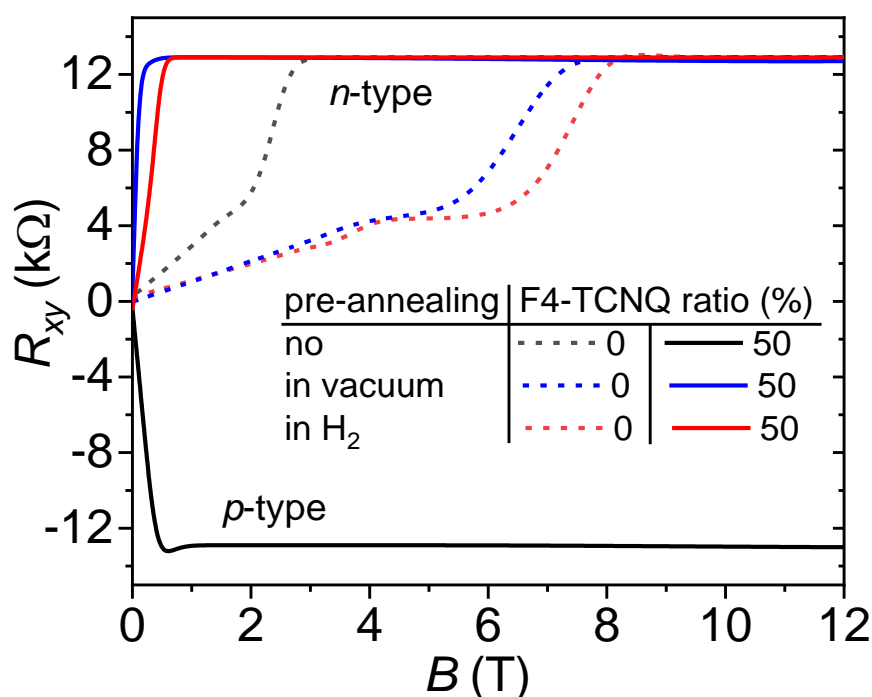


Figure 4.3 Comparison of the Hall resistances for differently pre-conditioned graphene devices without and with 50% volume ratio F4-TCNQ doping. The doping-related shift of the Hall curves indicates that the initial carrier density has a decisive influence on compensation doping. Adapted from the reference [51].

Since the F4-TCNQ molecular doping is a compensation doping technique, it is important to consider the initial carrier density of graphene when using this molecular doping method. The final adjustment of the carrier density in graphene is determined by both the initial carrier

4.3 Decisive influence of graphene's initial charge carrier density

density and the F4-TCNQ doping ratio, as observed in our experiments. For the graphene with different pre-annealing treatments, spin-coating the same F4-TCNQ doping concentration (50:100) on graphene leads to distinct final electron densities in graphene. This is demonstrated by a steeper Hall slope and an early onset of the Hall plateau at lower magnetic fields for the doped graphene, as shown in Figure 4.3.

The quantum Hall measurements of the devices with the same F4-TCNQ doping ratio but different initial carrier densities are presented in Figure 4.3. The Hall measurement calculation clearly reveals that the electron density of the vacuum pre-annealed device (blue curves) with a lower initial value shifted to a lower final value (from $n = 5.83 \times 10^{11} \text{ cm}^{-2}$ to $6.69 \times 10^9 \text{ cm}^{-2}$), while the electron density in the hydrogen annealed device (red curves) shifted from a higher initial value of $n = 7.12 \times 10^{11} \text{ cm}^{-2}$ to a higher final value of $3.17 \times 10^{10} \text{ cm}^{-2}$. This is manifested in a steeper Hall slope and an onset of the Hall plateau at lower magnetic fields.

However, the undoped device without annealing treatment exhibits the lowest initial electron density. At the same doping concentration ratio, the electron acceptor of the F4-TCNQ molecule completely compensates for the electron in graphene, leading to a *p*-type graphene. Figure 4.3 shows that the Hall slopes of the non-annealed devices change the sign from positive to negative, indicating that the graphene is transferred from *n*-type ($n_e = 2.4 \times 10^{11} \text{ cm}^{-2}$) to *p*-type ($n_p = 1.96 \times 10^{10} \text{ cm}^{-2}$) by the F4-TCNQ doping. This comparison highlights the importance of the graphene pre-treatment and initial carrier density knowledge for controlling the final carrier density of an F4-TCNQ-doped device.

Furthermore, when examining the absolute compensated electron density in graphene through the molecular doping process, the value of compensated electron density varies among the three groups of devices with different pre-annealing treatments. This variation in doping efficiency may be related to the difference in energy gaps between the Fermi energy in graphene and the lowest unoccupied molecular orbital (LUMO) in the F4-TCNQ molecule. This comparison demonstrates that controlling the final carrier density of graphene by F4-TCNQ doping requires careful consideration of the pre-treatment of graphene and its initial carrier density.

It is worth mentioning that the presented F4-TCNQ doping technique allows the fabrication of a high-quality *p*-type epitaxial graphene QHR device for metrological applications. [50] This is in contrast to other studies where direct evaporation of F4-TCNQ powder onto the graphene surface failed to achieve *p*-type graphene. [83,106,107,112] The studies in the literature have only observed *n*-type epitaxial graphene. By the high coverage, F4-TCNQ doping the Fermi

energy saturates at a low value in the *n*-type regime. The reason could be related to different initial electron densities or host matrix-related effects. For the high coverage of powder deposition on the graphene surface, a cluster of atoms becomes non-negligible and inevitable, which saturates the efficiency of charge transfer doping. Meanwhile, the F4-TCNQ molecules dispersed in PMMA uniformly distribute on the graphene surface, resulting in a high efficiency of charge transfer and *p*-type doped graphene.

4.4 Different doping stacks for the molecular doping

The electron densities of the 3- and 5-layer (3L and 5L) doped devices are presented in Table 4-2. The result of the electron density varying with the doping layers is consistent with that of varying the F4-TCNQ concentration. The 3L structures exhibit a higher carrier density than the 5L structures at the same F4-TCNQ doping ratio (5:100). This is attributed to a lower amount of supplied F4-TCNQ molecules in the 3L structure compared to the 5L structure. In addition, the 3L structure has a thinner dopant stack, which may lead to a higher rate of F4-TCNQ molecules being lost due to out-diffusion from the dopant stack. As a result, fewer F4-TCNQ molecules accumulate on the graphene surface, leading to a higher electron density in the 3L structures.

Table 4-2. Characteristics of the graphene Hall bar devices with 2-layer, 3-layer, and 5-layer doping stacks. The volume ratio of F4-TCNQ in 2-layer structures is 50:100, and in both the 3-layer and 5-layer structures is 5:100.

Volume ratio	Pre-annealing	Doping stack	Carrier density [cm ⁻²]	Mobility [cm ² V ⁻¹ s ⁻¹]
0:100	vacuum	1L	5.83×10 ¹¹	5010
5:100	vacuum	3L	5.40×10 ¹¹	6680
5:100	vacuum	5L	2.22×10 ¹¹	8260
0:100	H ₂	1L	7.12×10 ¹¹	4290
5:100	H ₂	3L	4.29×10 ¹¹	4390
5:100	H ₂	5L	2.70×10 ¹¹	4520
50:100	vacuum	2L	2.32×10 ¹¹	4260
50:100	vacuum	2L	2.70×10 ¹¹	6640

In contrast, the 2L structures have a dopant blend layer that is directly spin-coated onto the graphene surface, followed by a capping layer of copolymer, as illustrated in Figure 4.4(b). The

4.5 Transport scattering mechanism in epitaxial graphene

results in Table 4-2 indicate that the graphene can be doped with equal efficiency using a 2L structure, as compared to that of the 3L and 5L structures.

The electron density in the 2L structures is lower than in the 3L structures, which is reasonable considering the 10 times higher doping volume ratio used for the former. Compared to the 5L structures (with a spacer layer) that have the same doping ratio (50:100), the 2L structure (without a spacer layer) exhibits more than 10 times higher electron density. Nevertheless, it is difficult to calculate the impact of the absence of the spacer layer.

Notably, the 2L and 3L structure devices exhibit mobility values comparable to those of the 5L structure, which demonstrates that the variation in the doping stack and the presence of a spacer layer do not negatively impact electron scattering in graphene.

4.5 Transport scattering mechanism in epitaxial graphene

4.5.1 High mobility of epitaxial graphene doped by F4-TCNQ

The impact of the molecular dopant on the electron transport properties can be inspected by measuring the charge carrier mobility μ . The Hall mobility was calculated from the measured zero-field resistivity ρ_{xx} , using the formula $\mu = 1/(e \cdot n \cdot \rho_{xx})$. As shown in Table 4-1, the mobility is increasing as the electron density decreases. This typical behavior in epitaxial graphene has been reported in the literature. [79,92,93] [108] [81] [113] In our study, electron mobility up to $\mu_e = 48100 \text{ cm}^2/\text{Vs}$ and hole mobility up to $\mu_h = 57550 \text{ cm}^2/\text{Vs}$ were achieved by molecular doping, which is in agreement with the literature values and indicates the exceptional quality of our molecularly doped graphene devices. [81,93] [109] [113] Interestingly, the increase in mobility was a result of increasing the level of compensation (higher F4-TCNQ concentration), indicating no severe degradation of the electron transport properties by molecular doping.

According to the calculation of carrier densities in our graphene, we can estimate the upper limit of the Fermi energy fluctuation near the Dirac point. In the absence of an external gate voltage, the lowest electron density achieved in the n -type graphene by F4-TCNQ doping is $n_e = 6.69 \times 10^9 / \text{cm}^2$ ($\mu_e = 48100 \text{ cm}^2/\text{Vs}$), and the lowest hole density achieved in the p -type graphene is $n_h = -5.99 \times 10^{10} \text{ cm}^2$ ($\mu_h = 57550 \text{ cm}^2/\text{Vs}$). These data are extracted from the magnetotransport measurements at 4.2 K, from which the devices simultaneously fulfill the criteria of linear $R_{xy}(B)$ at low magnetic fields and a fully developed Hall plateau at $\nu = 2$. These criteria correspond to devices that behave as a single electronic band system with

spatially homogeneous carrier density. [114–118] Hence, the upper limit of electron (hole) density fluctuations for the *n*-type (*p*-type) graphene doped by F4-TCNQ is calculated as $\Delta E_F \sim 9.5$ meV ($\Delta E_F \sim 9.0$ meV), according to Equation 2.9, $E_F = \hbar v_F \sqrt{\pi n}$ (\hbar the reduced Planck constant, v_F the Fermi velocity in graphene).

4.5.2 Long-range and short-range scattering in epitaxial graphene

At low temperatures below 20 K, the mobility is limited by charge impurities (long-range scattering) and neutral atomic defects (short-range scattering). [119–122] At low carrier densities, the mobility is dominated by the charge impurity scattering, which is independent of carrier density. In the case of charged impurities, the carrier mobility is inversely proportional to the impurity density n_{imp} [122,123]. This can be expressed as follows:

$$\mu_c \approx \frac{C_0}{n_{imp}} \quad (4.1)$$

where C_0 is a constant. [123] If the impurity density n_{imp} is not changing, μ_c is a constant value. At high carrier densities, the mobility is dominated by the neutral atomic defect scattering, which is dependent on the carrier density n . The mobility induced by the short-range scattering is derived by the equation [121,122,124],

$$\mu_s = \frac{1}{ne\rho_s} \quad (4.2)$$

where ρ_s is the resistivity due to the short-range scattering. According to Matthiessen's rule, the overall mobility at low temperatures is derived by the equation,

$$\mu^{-1} = \mu_c^{-1} + ne\rho_s \quad (4.3)$$

The F4-TCNQ doping technique enables control of the carrier density of epitaxial graphene from the *n*-type to the *p*-type regime. We systematically investigated the mobility as a function of carrier density for the *n*- and *p*-type devices, as shown in Figure 4.4. Each data point is extracted from an individual device and a QHE measurement at 4.2 K. As the carrier density is reduced by F4-TCNQ molecular doping, the electron and hole mobilities increase. However, the electron and hole mobilities exhibit an asymmetric dependence on carrier density, indicating the presence of an asymmetric scattering behavior for electrons and holes in epitaxial graphene. At a carrier density of around 7.0×10^9 cm⁻², the electron and hole mobilities are equal in the experiment data. As the carrier density gradually increases in a wide range from 10^9 cm⁻² to 10^{11} cm⁻², the electron mobility is always larger than the hole mobility, and the estimated

mobility ratio of electron to hole increases from 1 and 2. At a carrier density of 10^{11} cm^{-2} , the electron mobility is approximately twice that of the hole mobility.

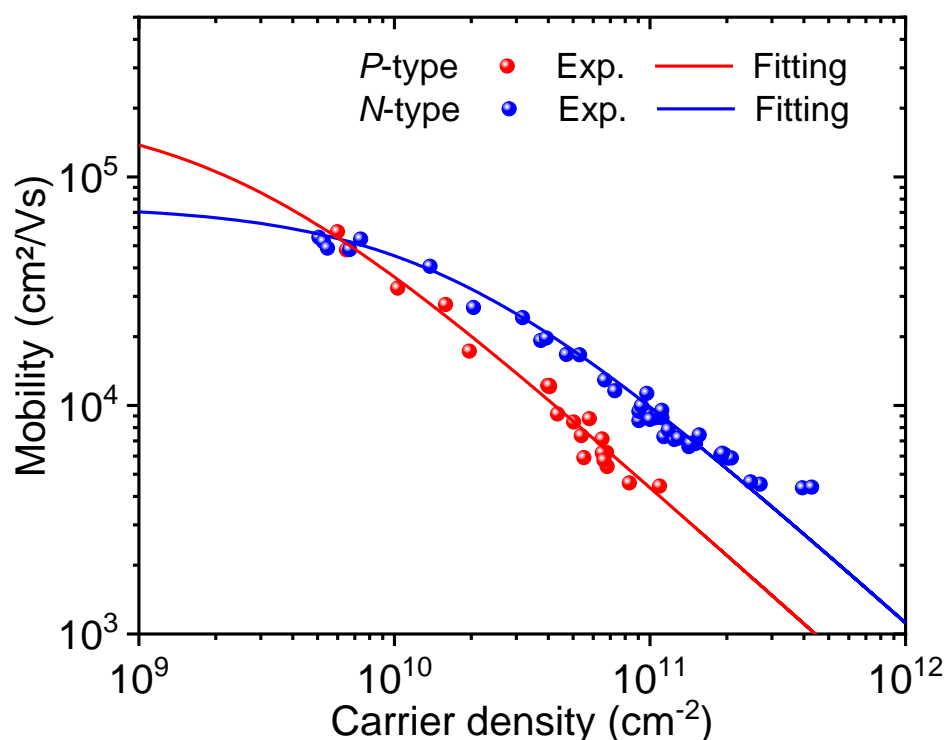


Figure 4.4 The mobility as a function of carrier density for *n*- and *p*-type epitaxial graphene doped by F4-TCNQ molecules. The transport measurements are performed at 4.2 K, in which the mobility is limited by the long- and short-range scatterings.

As previously discussed, the charge carrier scattering in epitaxial graphene at low temperatures is dominated by long-range and short-range scattering. Assuming that the density of the charge impurities did not change by the F4-TCNQ molecular doping, the data fits well (solid line in Figure 4.4) to Equation 4.3, in which both long- and short-range scattering are included. In this model, both μ_c and ρ_s are fitting parameters that are assumed to be constant. We obtain the $\mu_{ch} \approx 200\,000 \text{ cm}^2/\text{Vs}$ ($\mu_{ce} \approx 75\,000 \text{ cm}^2/\text{Vs}$), and $\rho_{sh} \approx 14\,000 \Omega$ ($\rho_{se} \approx 5\,500 \Omega$) for hole (electron). The fitting results indicate that the *n*- and *p*-type epitaxial graphene exhibit different long-range and short-range scattering.

At carrier densities above $1.0 \times 10^{10} \text{ cm}^{-2}$, the scattering is dominated by the short-range scattering, while the long-range scattering is negligible ($\mu_c^{-1} \ll n\rho_s$) in high carrier density region $n \geq 1.0 \times 10^{10} \text{ cm}^{-2}$. According to the fitting values of $\rho_{sh} > \rho_{se}$, the *p*-type epitaxial graphene has stronger short-range scattering than that in *n*-type graphene. The reason is not clear yet.

In the low carrier density region ($n < 1.0 \times 10^{10} \text{ cm}^{-2}$), the long-range scattering is the dominant scattering, while the short-range scattering is negligibly small ($\mu_c^{-1} \gg n e \rho_s$). According to the fitting values of charge impurity mobility $\mu_{ch} > \mu_{ce}$, the *p*-type epitaxial graphene has less long-range scattering than that in *n*-type graphene. The unequal charge impurity mobility of electrons and holes in epitaxial graphene is a consequence of the unbalanced scattering cross sections for charged scatterers in a system with 2D relativistic dispersion. [123,125] This theory can be understood by considering the idea that an attractive potential scatters a charge carrier more effectively than a repulsive potential. [125]

In as-grown epitaxial graphene, the intrinsic *n*-type electron density is attributed to *p*-type polarization doping induced by the bulk of the hexagonal SiC substrate and overcompensation by donor-like states related to the buffer layer. [126] The main charge impurities in epitaxial graphene are the donor-like states, including the Si dangling bonds and interface states in the buffer layer. The donor-like states are positively charged beneath the graphene layer, which serves as the attractive potential scatters for electrons and repulsive potential for holes. According to the theory discussed above, the cross-section for repulsive scatters is less than that of the attractive scatters. Therefore, the positive charge impurities have less scattering strength for the hole, resulting in a higher charge impurity mobility for the hole. Our experiment and fitting results are well explained by this theory model in the literature.

Please note here that the carrier density is tuned by varying the amounts of F4-TCNQ molecules, which is different from the case of tuning the carrier density using a top metal gate applying a gate voltage. The latter tunes the carrier density by changing the Fermi level of graphene, whereas the density of charge impurities below the graphene is not affected by the gate voltage. The analyses above assume that the density of the charge impurities did not change by the F4-TCNQ molecular doping. It is also possible that the density of the charged impurities in epitaxial graphene can be reduced by the F4-TCNQ molecular doping. In this case, both the charge impurity mobility μ_c and the carrier density are controlled by the F4-TCNQ doping. In past studies, it has not been addressed yet whether the density of charge impurity below the graphene is tuned by F4-TCNQ molecular doping or not.

4.5.3 Temperature-dependent mobility

In epitaxial graphene, the temperature-dependent resistivity can be described by the model, [82,113,127–129]

$$\rho = \rho_0 + \rho_{LA} + \rho_{RIP} \quad (4.4)$$

4.5 Transport scattering mechanism in epitaxial graphene

where ρ_0 is the residual resistivity at low temperatures and ρ_{LA} is the resistivity due to longitudinal acoustic (LA) phonon scattering:

$$\rho_{LA} = \frac{\pi D_A^2 k_B}{e^2 \hbar \rho_s v_s^2 v_F^2} T, \quad (4.5)$$

with $D_A = 18$ eV being the acoustic deformation potential [82,130], k_B the Boltzmann constant, e the electron charge, \hbar the Planck constant, $\rho_s = 7.6 \times 10^{-7}$ kg/m² the two-dimensional mass density, $v_s = 1.73 \times 10^4$ m/s the sound velocity, $v_F = 10^6$ m/s the Fermi velocity, and T the temperature. The third contribution from the remotely interfacial phonons (RIPs). The low-energy phonon modes are given by,

$$\rho_{RIP} = \sum_{i=1}^3 \left(\frac{C_i}{\exp(E_i/k_B T) - 1} \right), \quad (4.6)$$

where C_i is the electron-phonon coupling constant and E_i is the phonon energy. To fit our data, we considered three phonon modes of 6H-SiC epitaxial graphene, $E_{ph1} = 70$ meV, $E_{ph2} = 16$ meV, and $E_{ph3} \approx 2.0$ meV. [82,131,132] These phonon energies were selected to match the low-energy phonon modes in epitaxial graphene on SiC, as measured by inelastic tunnelling spectroscopy (IETS) [82,131,132]. The 16- and 70-meV phonon modes correspond to two out-of-plane acoustic phonon modes at the Γ -point and M -point respectively, where two neighboring planes (here the graphene and the buffer layer) are oscillating out of phase. The coupling of these phonon modes to the charge carriers in epitaxial graphene is significantly enhanced at the position of the localized defects in the buffer layer/substrate. [131,132]. The 2.0 meV phonon mode can be attributed to the low-frequency horizontal phonon mode at 2 – 5 meV at the Γ -point [133]. This mode occurs when two neighboring planes (here graphene and buffer layer) oscillate out-of-phase parallel to each other.

Figure 4.5 shows the electron mobility as a function of temperature from 4.2 to 300 K for device G1594-D6_3(chip1)2 HFML. The electron density of this device is 3.28×10^{11} cm⁻² at 4.2 K. The mobility limits as a result of various scattering mechanisms, including charge impurity scattering, scattering by remotely interfacial phonons at the graphene/SiC interface, and scattering by LA phonons in graphene (in-plane) [82,113]. At $T < 25$ K, the electron mobility remains nearly constant as the temperature increases. The charge impurities and atomic defects play the most dominant role. At $T > 25$ K, the electron mobility gradually decreases as the temperature increases. The mobility is limited by the remote interfacial phonons scattering since

the LA phonons make only a small contribution to the overall mobility for temperatures above 400 K.

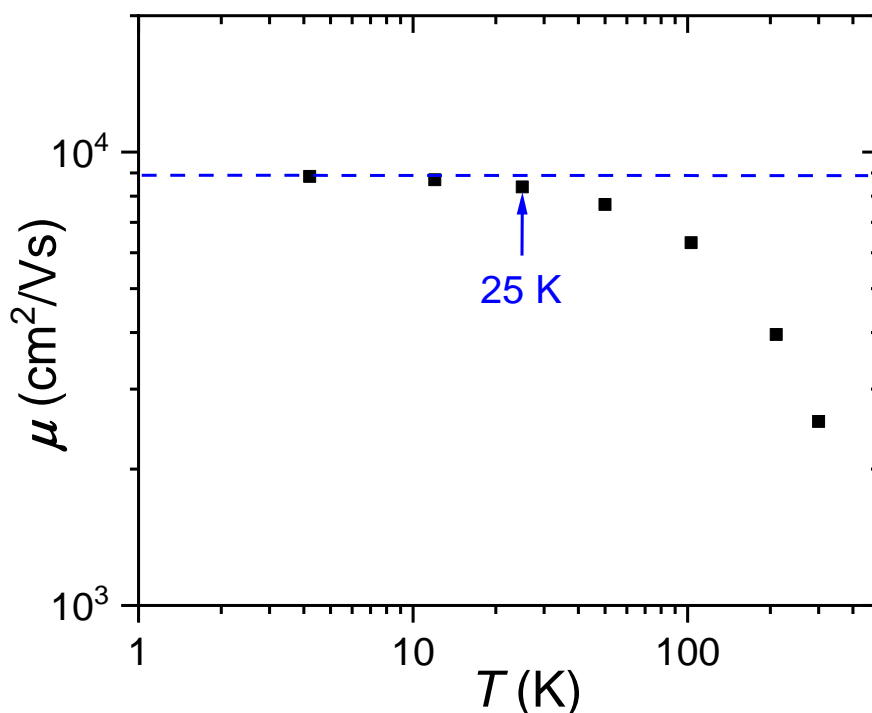


Figure 4.5 The electron mobility is a function of temperature from 4.2 to 300 K for device G1594-D6_3(chip1)2 HFML. The electron density of this device is $3.28 \times 10^{11} \text{ cm}^{-2}$ at 4.2 K. The mobility decreases as temperature increases.

4.6 Doping model for F4-TCNQ molecular doped epitaxial graphene on SiC

This section describes an energy band model to explain the F4-TCNQ molecular doping process on graphene surface in the experiment. The simulation results based on the density functional theory (DFT) confirmed the energy band alignment results. The charge density difference at the single-layer graphene/F4T-CNQ interface was performed using the *Quantum Espresso* software package, including Perdew-Burke-Ernzerhof parametrization of the generalized gradient approximation (GGA-PBE) exchange-correlation functional and projector augmented wave (PAW) pseudopotentials. The geometric optimization and calculation of HOMO/LUMO energy states of an isolated F4-TCNQ molecule at different ionization states (F4-TCNQ⁰, F4-TCNQ⁻¹, F4-TCNQ⁻²) were calculated using *ORCA* software. DFT calculations were applied using the Hybrid Meta-GGA XC PW6B95 functional with the Karlsruhe basis set of valence triple-zeta polarization (def2-TZVP) for all atom types.

In this section, Stefan Wundrack conducted the DFT simulation. Based on his simulation results and the experimental data discussed above, we established a charge transfer model and an energy band alignment picture to explain the F4-TCNQ molecular doping process on the graphene surface. We would like to acknowledge the fruitful discussion and insightful comment provided by Prof. Dr. Thomas Seyller regarding the energy band alignment picture.

4.6.1 Electron wave function and charge density distribution

The interpretation of this result requires a more detailed understanding of the microscopic doping mechanism. Recent findings suggest that molecular doping occurs through the diffusion of the F4-TCNQ molecules from the doping layer to the graphene surface via the copolymer spacer layer. [109] The amount of F4-TCNQ on the graphene surface is proportional to the concentration in the doping layer as given by the diffusion law, as given in the reference. [109] Moreover, it can be assumed that the F4-TCNQ doping layer concentration is approximately proportional to the volume concentration in the dopant solution because the anisole is completely evaporated during the 160 °C annealing process. As a result, the F4-TCNQ concentration at the graphene surface is assumed to vary linearly with the F4-TCNQ volume ratio (in Figure 4.2).

In the actual doping process, only dopant molecules in close proximity to the graphene surface are involved. [83] Simulation studies have proven that the F4-TCNQ molecules are favorably positioned parallel to the graphene surface at a distance of a few angstroms. [107] Based on the configuration, the electron wave function distribution was simulated by our collaborator Stefan Wundrack of PTB's Chemistry Division using density functional theory (DFT) software, as illustrated in Figure 4.6. The planar molecular structure of F4-TCNQ is visually presented in Figure 4.6(a). The wave function distribution (ψ) in the highest occupied molecular orbital (HOMO) molecular orbital of the F4-TCNQ molecule indicates the backbone of the conjugated π -electron system in its ground state. Figure 4.6(b) schematically represents the electron wave function distribution in both the ground state (F4-TCNQ⁰) and excited state (F4-TCNQ⁻¹) of the F4-TCNQ molecule. The F4-TCNQ molecule undergoes a transition from its ground state (F4-TCNQ⁰) to the excited state (F4-TCNQ⁻¹) upon accepting an electron. In the excited state, the single charge (electron) is balanced by the formation of an aromatic carbon ring, and the separation of the negative charge near the CN group leads to the redistribution of the π -electrons. Both the simulation and the previous experimental results [83] prove that the cyano (CN) groups of the F4-TCNQ molecule play a crucial role in the accumulation of charge carriers in

their local environment in graphene. The DFT calculations demonstrate a bond rearrangement of HOMO (ground state, F4-TCNQ) and HOMO* (excited state, F4-TCNQ⁻¹).

DFT simulation of charge transfer in F4-TCNQ/graphene system

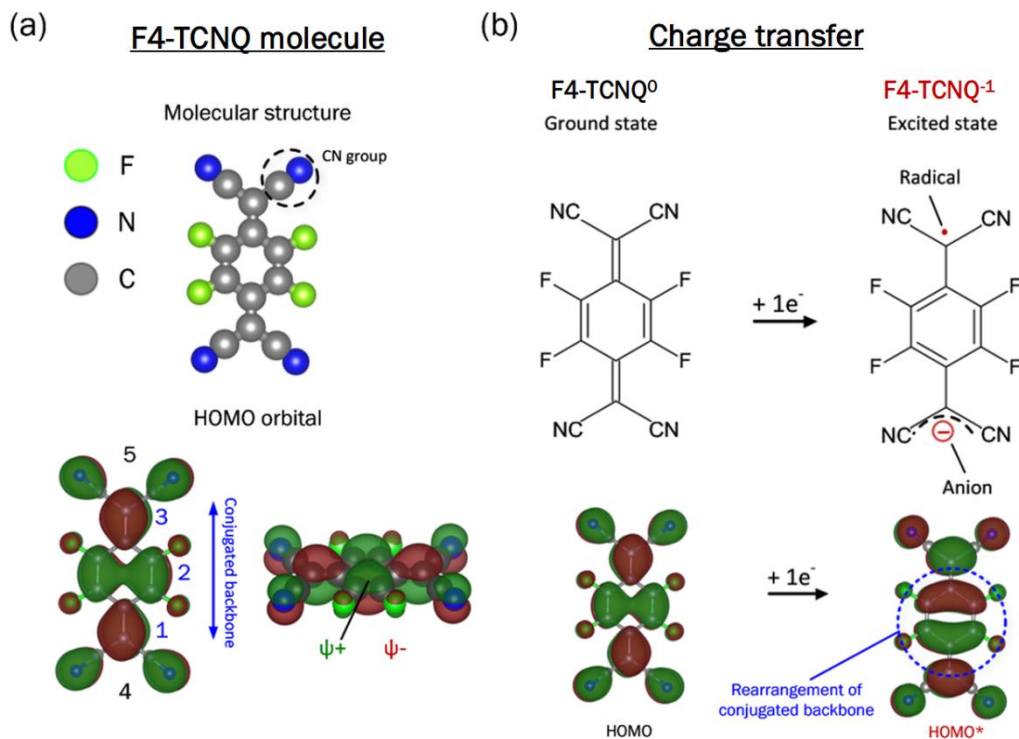


Figure 4.6 The electron wave function distribution (a) Planar molecular structure of F4-TCNQ and visualization of the wave function distribution (ψ) in the HOMO molecular orbital indicating the backbone of the conjugated π -electron system. (b) Schematic representation of the rearrangement of the π -electrons in the charge transfer process in F4-TCNQ. The charge carrier acceptance of a single electron is compensated by forming an aromatic carbon ring and separating the negative charges near the CN groups. DFT calculations reveal a bond rearrangement in F4-TCNQ between HOMO (ground state, F4-TCNQ⁰) and HOMO* (excited state, F4-TCNQ⁻¹). Adapted from the reference [51].

Figure 4.7 shows the extracted energy levels of the F4-TCNQ molecule, the single-ionized F4-TCNQ⁻¹, and the double-ionized F4-TCNQ⁻² based on the DFT simulation. The calculated electron affinity E_A indicates an energy shift from the HOMO and lowest unoccupied molecular orbital (LUMO) levels to the HOMO* and LUMO*. There is also a significant decrease in electron affinity. The F4-TCNQ molecule has an electron affinity of 5.35 eV, while the single ionized F4-TCNQ⁻¹ has an electron affinity of 1.09 eV. It is important to note that these

4.6 Doping model for F4-TCNQ molecular doped epitaxial graphene on SiC

ionization states were calculated only for a single molecule in a vacuum cell and do not consider any interaction with epitaxial graphene.

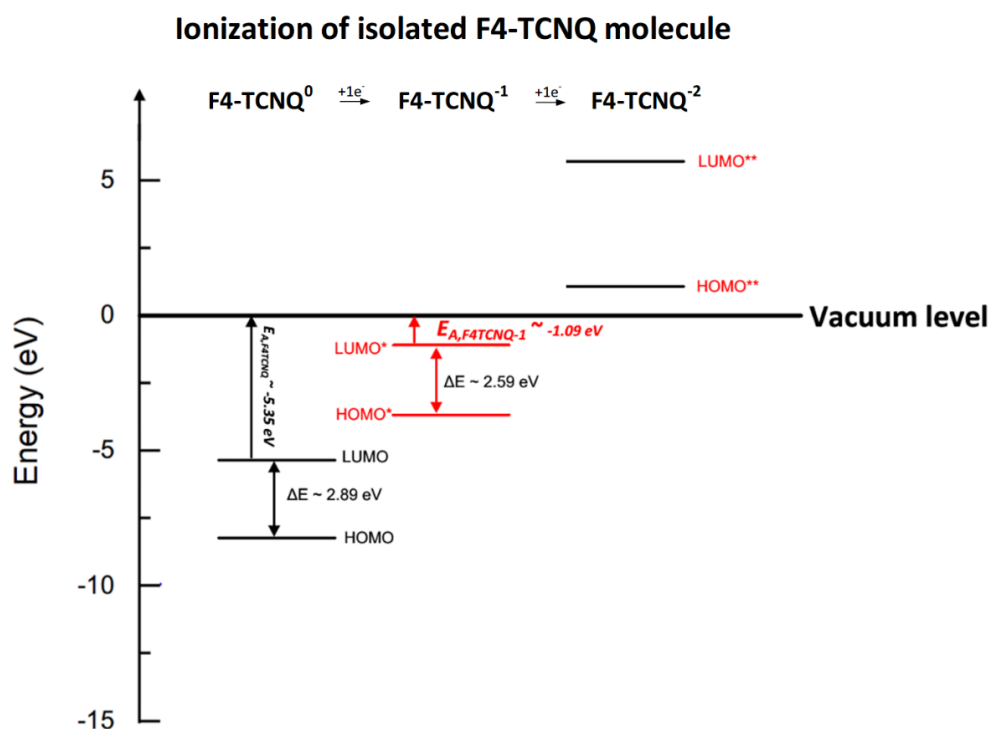


Figure 4.7 Calculated energy levels of an isolated F4-TCNQ molecule physisorbed on a graphene supercell in the neutral state (HOMO and LUMO, F4-TCNQ⁰), in the single ionized (HOMO* and LUMO*, F4-TCNQ⁻¹) and the double ionized state (HOMO** and LUMO**, F4-TCNQ⁻²). E_A denotes the calculated electron affinity. Adapted from the reference [51].

The simulation of the charge density difference of a single F4-TCNQ molecule is shown in Figure 4.8. The red (blue) distribution represents the charge accumulation (depletion). Charge accumulation primarily occurs near the CN groups of the F4-TCNQ molecule due to the wavefunction overlap between the π -bonds of graphene and the CN groups of F4-TCNQ, leading to the formation of charge transfer complexes (CTC). According to the simulation results, it is estimated that an F4-TCNQ molecule receives about 0.3 - 0.4 electrons from graphene. [107,109]

Charge density difference of SL Graphene/F4-TCNQ interface

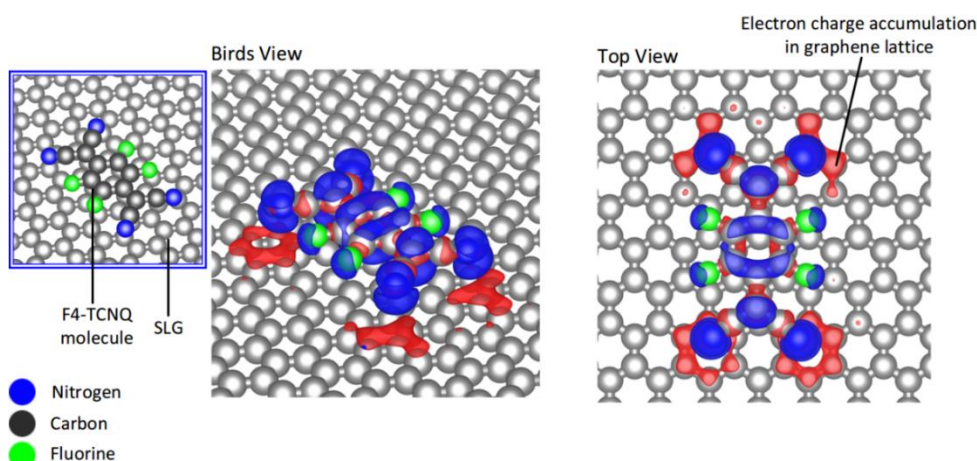


Figure 4.8 Charge density difference of monolayer graphene/F4-TCNQ interface.

Calculated charge density difference plot of F4-TCNQ physisorbed on a graphene supercell. The red (blue) distribution corresponds to charge accumulation (depletion). The accumulation of charge carriers in graphene occurs predominantly near the CN groups of the F4-TCNQ molecule. There is an increased tunnel probability due to a small distance ($d_{\text{calculated}} \approx 3.4 \text{ \AA}$) between graphene and F4-TCNQ and the energetically favorable position between graphene's Fermi level ($E_{\text{F}} \approx 4.3 \text{ eV}$) and F4-TCNQ LUMO level ($E_{\text{LUMO}} \approx 5.3 \text{ eV}$). Adapted from the reference [51].

4.6.2 Energy band alignment in graphene/F4-TCNQ charge transfer complex

Due to the strong electron affinity of F4-TCNQ (5.35 eV compared to 4.30 eV of epitaxial graphene), the Fermi energy of graphene is higher than the HOMO of the F4-TCNQ molecule. As a result, the neutral F4-TCNQ molecules in proximity to the graphene surface act as potent electron acceptors. The electrons in graphene transfer to the LUMO state of the F4-TCNQ molecules, as shown in Figure 4.9. [83,107,112,134] Finally, the electron density in the graphene layer decreases, causing the Fermi energy in graphene to shift to a lower value. The F4-TCNQ molecules receive electrons from the graphene to fill the LUMO state, resulting in the formation of the F4-TCNQ⁻ charge. This redistribution of charge density leads to the formation of excited HOMO* and LUMO* states at higher energies in the graphene/F4-TCNQ⁻ charge transfer complex.

The amount of charge transferred from graphene to the F4-TCNQ is affected by two factors: the number of available acceptors and the difference between the work functions of graphene and the F4-TCNQ LUMO level. [93,135] The reduction in the difference in work functions

4.6 Doping model for F4-TCNQ molecular doped epitaxial graphene on SiC

between graphene and F4-TCNQ explains the self-limitation of the doping process as the F4-TCNQ concentration increases. In addition, the reduction in available sites on the graphene surface for the F4-TCNQ molecule at high doping concentrations is another reason. The accumulation of negative charge above the graphene layer causes a gating effect. The schematic band diagram in Figure 4.9 shows the excited highest occupied molecular orbital (HOMO*) level of the F4-TCNQ⁻ anions that have accepted an electron from the graphene layer. Furthermore, the accumulation of F4-TCNQ⁻ anions on top of the graphene layer can act as a negatively charged gate, hindering electron transfer to the dopant molecules due to Coulomb repulsion. This effect should also be considered when analyzing the doping mechanism, and it can be compared to the photochemical gating by light-induced acceptors in a resist layer atop epitaxial graphene. [93]

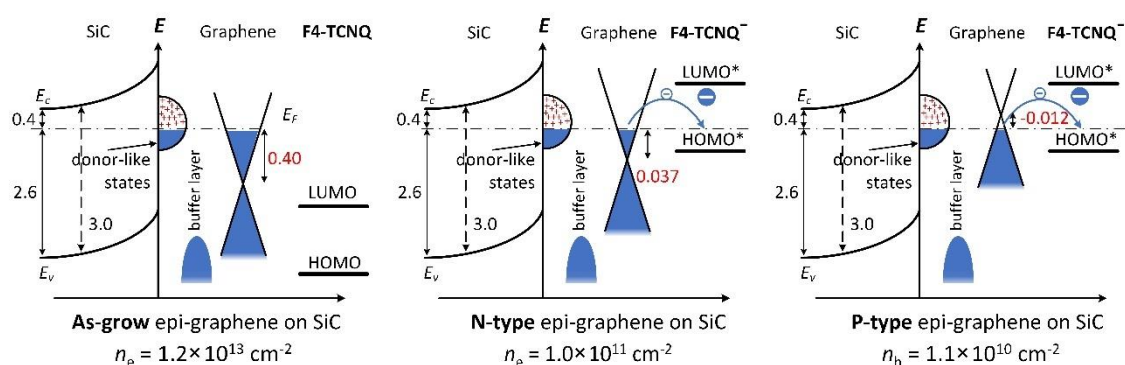


Figure 4.9 Schematic band diagram sketch for molecular doping of *n*- and *p*-type epitaxial graphene by F4-TCNQ. (a) Before charge transfer, the high electron density ($n_e = 1.2 \times 10^{13} \text{ cm}^{-2}$) of as-grown epitaxial graphene is attributed to donor-like states between the SiC surface and the buffer layer, e.g., Si dangling bonds. The energy position of the highest occupied molecular orbital (HOMO) and lowest unoccupied molecular orbital (LUMO) state in F4-TCNQ are below the Fermi energy. In the doped state, the electron density of as-grown graphene is reduced to (b) $n_e = 1.0 \times 10^{11} \text{ cm}^{-2}$ for *n*-type graphene and (c) $n_h = 1.1 \times 10^{10} \text{ cm}^{-2}$ for *p*-type graphene. The graphene/F4-TCNQ⁻ charge transfer complex is formed. The excited HOMO* and LUMO* states shift to higher energies. (a) The neutral F4-TCNQ molecule and (b – c) the anion F4-TCNQ⁻ after accepting one electron present in the diagram. With this reaction, a delocalized ionic state is formed, and the F4-TCNQ turns into an aromatic molecule.

As previously discussed, the electron density in epitaxial graphene is closely related to the donor-like states located at the interface of the SiC substrate and the buffer layer [126], as depicted in Figure 4.9. These donor-like states act as a reservoir of electrons, which are donated

to the graphene. It is assumed that the charges in these states also change during the equilibration process of charge transfer. This means that the F4-TCNQ molecules on the graphene surface partially compensate for the charges in donor-like states due to the energy difference in the work function between the F4-TCNQ and the donor-like states.

4.6.3 Exclusion of double ionized state F4-TCNQ⁻² and charge transfer to PMMA

We now also consider the formation of the doubly ionized state (HOMO^{**} and LUMO^{**}, F4-TCNQ⁻²). The HOMO^{**} and LUMO^{**} levels of the doubly ionized F4-TCNQ are above the vacuum level, indicating an energetically unstable state. Our calculation demonstrates that the doubly ionized state is indeed an energetically unstable state, which is consistent with previous experimental results [83], where only the single ionized anion (F4-TCNQ⁻) was observed. Thus, we excluded the doubly ionized state from the charge transfer process.

Furthermore, the calculation results indicated that the PMMA, which only acts as an insulator, does not contribute to the charge transfer process. Therefore, we can conclude that the charge transfer from the graphene, F4-TCNQ, and F4-TCNQ⁻ to the PMMA is ruled out. The energy alignments of the LUMO and HOMO levels of the PMMA [136], a single F4-TCNQ molecule, the work functions (Φ) of the donor-like states (dangling bonds) in the buffer layer of 6H-SiC, and the work function of single-layer graphene (SLG) are shown in Figure 4.10. The Fermi energy in graphene lies between the LUMO and HOMO levels of PMMA, making the charge transfer between the graphene and PMMA impossible. The LUMO level of PMMA is higher than the HOMO levels of F4-TCNQ and F4-TCNQ⁻, making charge transfer impossible between a low energy level of F4-TCNQ and F4-TCNQ⁻ to a high energy level of PMMA. Therefore, the PMMA acts as an electron blockade layer and isolates the ionized charge F4-TCNQ⁻¹.

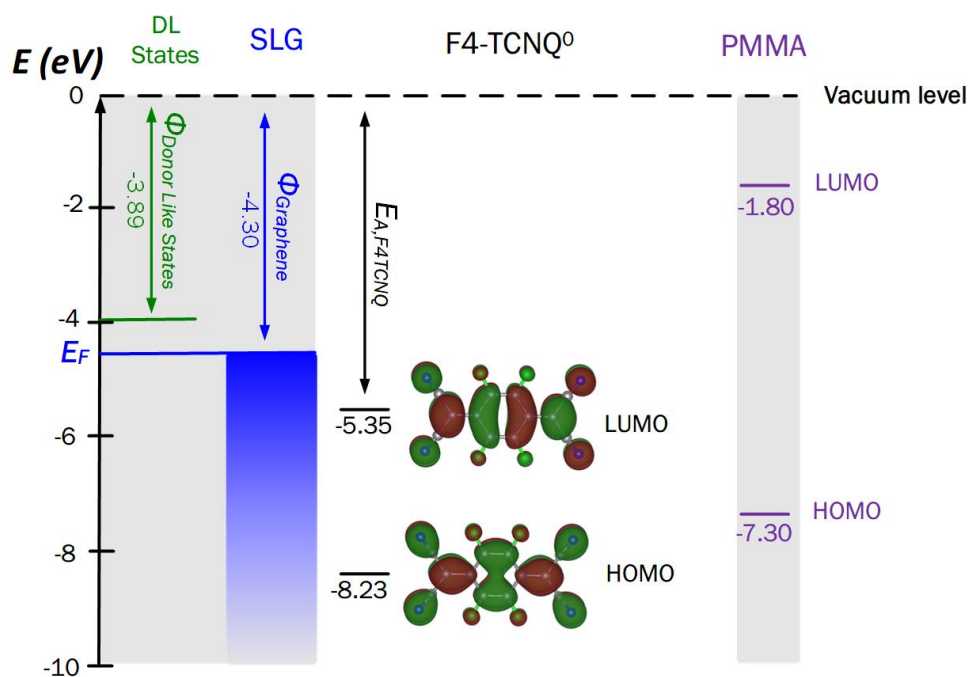


Figure 4.10 Comparison of the LUMO and HOMO levels of a single F4-TCNQ molecule with the work functions (Φ) of donor-like state (dangling bonds) in the buffer layer of 6H-SiC, work function of single-layer graphene (SLG) and HOMO and LUMO levels of PMMA. [136] Adapted from the reference [51].

Chapter 5. Epitaxial graphene quantum Hall resistance standard

This chapter presents high-accuracy measurement results of the *n*- and *p*-type graphene QHR standards. The carrier density of the epitaxial graphene QHR device is controlled by the F4-TCNQ molecular doping technique to the desired value in *n*- and *p*-type regimes for the resistance metrology. Section 5.1 introduces the history of graphene QHR standards that achieved accuracy on the level of $n\Omega/\Omega$ from institutions worldwide. Section 5.2 presents high-accuracy measurement results of *n*-type graphene QHR devices with different electron densities from 10^{11} cm^{-2} to 10^{10} cm^{-2} . Moreover, devices with 5L-, 3L-, and 2L doping stacks are also investigated by high-accuracy measurements. In these measurements, the deviation and quantization regimes are observed. The systematic high-accuracy measurements from devices with different carrier densities find that the onsets of the deviation and quantization regimes are correlated with the electron density. In section 5.3, a contour plot is proposed that describes the quantization regime as a function of the electron (hole) density and magnetic field. Section 5.4 discusses the high-accuracy measurement results of the *p*-type graphene QHR devices. Furthermore, the asymmetric behavior of the contour plot of the *n*- and *p*-type QHR standards is observed. Section 5.5 presents the temperature-dependent measurement of the graphene QHR standard. The $n\Omega/\Omega$ accuracy of the QHR is destroyed at temperatures $T > 25 \text{ K}$, which is explained by the unique remote interfacial phonon-mediated transport in epitaxial graphene.

Most of the content in Sections 5.2 and 5.3 is published in Ref. [51]. The content in Section 5.4 is to be submitted to a journal. Most of the graphene films on SiC used in Sections 5.2, 5.3, and 5.5 were grown by Dr. Davood Momeni and Dr. Atasi Chatterjee. Dr. Mattias Kruskopf contributed to the device fabrication and high-accuracy measurements of the *p*-type graphene QHR standards in Section 5.4. The magnetotransport measurements in high magnetic fields in section 5.5 were conducted at the High Field Magnet Laboratory (HFML-EMFL), Radboud University, the Netherlands, with support from Prof. Dr. Uli Zeitler and Dr. Oleksandr Zheliuk.

5.1 Graphene QHR standards

The quantum Hall effect allows the international standard for resistance to be defined in terms of the electron charge e and Planck's constant h alone. The effect comprises the quantization of the Hall resistance in two-dimensional electron systems in rational fractions of $R_K = h/e^2 = 25\,812.807\,459\,30\dots \Omega$, the resistance quantum. The level of precision necessary for metrology –

a few parts per billion – has been achieved in silicon and Gallium-Arsenide (GaAs) heterostructure devices. [84,137,138] The GaAs quantum Hall resistance (QHR) standard has been in use in many national metrology institutes (NMIs) since the 1990s. However, this level of accuracy is only achieved at high magnetic flux density (usually around $B = 10$ T), very low temperature ($T < 1.5$ K), and limited current magnitude (typically $I < 50$ μ A). [40,41] Graphene should, in principle, be an ideal material for a quantum resistance standard because it is inherently 2D, and its Landau levels are significantly split in a magnetic field.

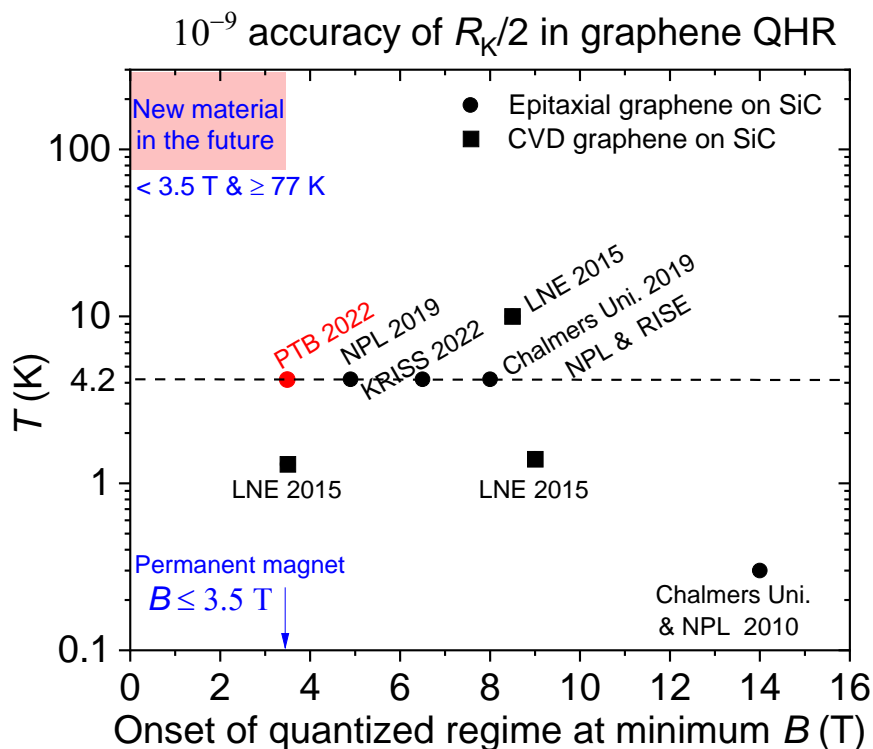


Figure 5.1 The resistance quantization based on the graphene QHR standard has achieved an accuracy of $n\Omega/\Omega$ under the operating conditions of minimum magnetic field and highest temperatures by different research groups all over the world. So far, only six institutions have reported that their graphene QHR standard successfully achieved accuracy on the $n\Omega/\Omega$ level in the world. All the graphene QHR standards are from four sources: the PTB, Chalmers University of Technology, KRIS, and LNE. [8] [47,48,139] [49–51] The red dot marks the results obtained within this thesis.

Over the past decade, epitaxial graphene on SiC has emerged as a promising alternative to GaAs heterostructures for QHR standards. Figure 5.1 presents the progress of epitaxial graphene QHR standards with an accuracy on the level of $n\Omega/\Omega$ for resistance quantization. So far, only six institutions worldwide have reported that their graphene QHR standard successfully achieved accuracy on the $n\Omega/\Omega$ level.

In 2010, Tzalenchuk et al [8] was the first to demonstrate that an epitaxial graphene QHR standard achieved an accuracy of 3 parts in 10^9 at a temperature of 300 mK and the magnetic fields $B > 11$ T. The graphene was epitaxially grown on SiC substrate on a large scale ($160 \times 35 \mu\text{m}^2$). In 2012, Woszczyzna et al [140] demonstrated that an exfoliated graphene QHR standard can also achieve accuracy on the level $n\Omega/\Omega$ at 60 mK and $B > 16$ T. Nevertheless, these operating conditions were not yet competitive with those used for GaAs QHR standards. In 2015, the LNE group demonstrated that the graphene QHR standard can achieve an $n\Omega/\Omega$ accuracy at 1.5 K and 3.5 T. [47,48,139] The graphene on SiC was grown by CVD. Since 2019, the groups from Chalmers University of Technology – NPL – RISE team, KRISS, and PTB reported resistance quantization with $n\Omega/\Omega$ accuracy in epitaxial graphene QHR standards at an increased temperature of 4.2 K. [49–51] All the graphene QHR standards are from four sources: the PTB, Chalmers University of Technology, KRISS, and LNE.

Realization of the resistance quantization under relaxed conditions, e.g., lower magnetic fields and higher temperatures, is of great importance for the dissemination of QHR standards. The graphene QHR standards in this thesis exhibit an advanced performance in terms of the operating conditions, which have achieved an accuracy of $(0.7 \pm 2.6) n\Omega/\Omega$ at a magnetic field as low as 3.5 T and a temperature of 4.2 K. In comparison with the graphene QHR standards in the literature [8] [47,48,139] [49–51], the graphene QHR standards in this thesis can achieve an $n\Omega/\Omega$ accuracy at a lower magnetic field at 3.5 T and higher temperature at 4.2 K simultaneously, as shown in Figure 5.1.

5.2 n-type graphene QHR standards

In chapters 4, 5, and 6, epitaxial graphene QHR standards with different carrier densities are fabricated by the optical lithography and the F4-TCNQ molecular doping method. The epitaxial graphene exhibits a very wide Hall plateau ($\nu = 2$), which is attributed to the Fermi level pinning in epitaxial graphene. This section presents high-accuracy measurement results that identify a deviation regime and a quantization regime in the wide Hall plateau, which were not previously recognized in graphene- and GaAs-based QHR standards in the literature. The investigation of the deviation regime in the Hall plateau is important for further understanding of the QHE in epitaxial graphene and its application to resistance standards. In the deviation and quantization regimes, the longitudinal resistances exhibit a minor difference in the level of micro-ohms, which is identified through high-accuracy measurement. The minor difference in the

longitudinal resistance is used to distinguish the boundary between the deviation and quantization regimes.

In the high-accuracy measurements, the deviation regime was defined by a criterion of a low but non-zero longitudinal resistivity $\rho_{xx} \leq 100 \text{ m}\Omega$. In this regime, the quantum Hall resistance R_{xy} starts to deviate from the nominal $R_K/2$ within the achievable measurement uncertainty. The quantization regime was defined by the criteria $|\rho_{xx}| = 0 \text{ }\mu\Omega$ within the uncertainty $\pm 23 \text{ }\mu\Omega$, which guarantees the relative deviation of the quantum Hall resistance R_{xy} from $R_K/2$ with an accuracy of $\text{n}\Omega/\Omega$, e.g., $(R_{xy} - R_K/2) / (R_K/2) \leq (0.7 \pm 2.6) \text{ n}\Omega/\Omega$ ($k = 2$). The definition of deviation and quantization regimes are discussed previously in detail in Section 3.5.

5.2.1 n-type QHR standard with different electron densities

Figure 5.2 presents the typical magnetotransport (b) and high-accuracy (a and c) measurements of the vacuum-annealed QHR device with 25% volume concentration F4-TCNQ (5L doping stack). Through F4-TCNQ molecular doping, the electron density was reduced to $1.1 \times 10^{11} \text{ cm}^{-2}$ at a measured temperature of 4.2 K. In the magnetotransport measurement, a very wide Hall plateau at filling factor 2 was observed at magnetic fields ranging from about 2 T up to 12 T, corresponding to a very small longitudinal resistivity. The high-accuracy values of the Hall and longitudinal resistances allow us to distinguish between the deviation and quantization regimes. The deviation regime was determined at the magnetic fields ranging from about 2 T to 4 T, where the longitudinal resistivity ρ_{xx} was non-zero but less than $100 \text{ m}\Omega$, as shown in Figure 5(b).

Figure 5.2(a), (c) shows the relative deviation of the quantum Hall resistance R_{xy} from $R_K/2$ and the longitudinal resistivity ρ_{xx} as a function of the magnetic field B in the high-accuracy measurements. The Hall resistance exhibits a perfect quantization with an accuracy of $|(R_{xy} - R_K/2) / (R_K/2)| < (0.7 \pm 2.6) \text{ n}\Omega/\Omega$ at magnetic fields $B \geq 3.5 \text{ T}$. The value of ρ_{xx} is $80 \text{ }\mu\Omega$ at $B = 3.5 \text{ T}$, but it has no detrimental effect on the QHR value due to the very small s parameter. [50] The longitudinal resistivity drops to $(20.1 \pm 23.0) \text{ }\mu\Omega$ at 4 T and further to $(3.8 \pm 19.7) \text{ }\mu\Omega$ at 12 T, demonstrating zero longitudinal resistivity within the uncertainty and a dissipationless state of the electron gas in the graphene.

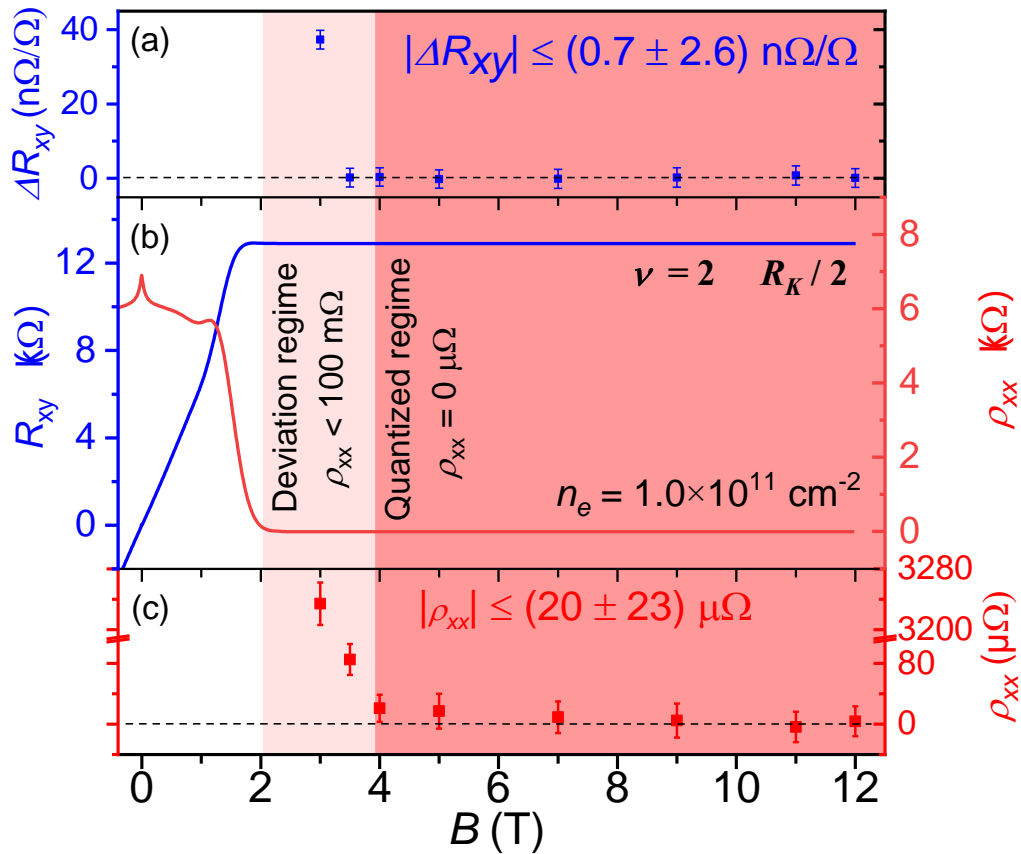


Figure 5.2 The magnetotransport (b) and high-accuracy (a), (c) measurement of the vacuum annealed QHR device with 25% volume concentration F4-TCNQ (5L doping stack). (b) Hall resistance R_{xy} and longitudinal resistivity ρ_{xx} as functions of the magnetic field from a graphene QHR device with carrier density $1.0 \times 10^{11} \text{ cm}^{-2}$ at 4.2 K. The deviation regime is at magnetic fields from 2 T to 4 T for this device, corresponding to the longitudinal resistivity $0 < \rho_{xx} < 100 \text{ m}\Omega$. High-accuracy measurement of (a) the Hall resistance deviation $(R_{xy} - R_K/2) / (R_K/2)$ and (c) the longitudinal resistivity ρ_{xx} on the $\nu = 2$ plateau at 4.2 K and $I = 38 \text{ }\mu\text{A}$. The relative deviation of the Hall resistance R_{xy} from $R_K/2$ is less than $(2 \pm 2.6) n\Omega/\Omega$ ($k = 2$) in the magnetic field from 4 T to 12 T. The quantization regime is defined by $\rho_{xx} = 0 \text{ }\mu\Omega$ with the uncertainty of $\pm 23 \text{ }\mu\Omega$ ($k = 2$). Here, the onset of the quantization regime is at $B = 4$ T.

The longitudinal resistance values determine the deviation regime, $0 < \rho_{xx} < 100 \text{ m}\Omega$. In this device, the deviation regime begins at about 2 T, which is about 2 T lower than the onset of the quantization regime. The width of the deviation regime is determined by the types and energy strength of the disorder. In the quantization regime, the measured values of ρ_{xx} are lower than any previously published values obtained at 4.2 K. [47,48] This suggests a homogeneous carrier distribution and spatial dispersion of the compensating dopant molecules. The vanishing

resistivity also indicates that no parallel transport channel has formed, regardless of the concentration levels.

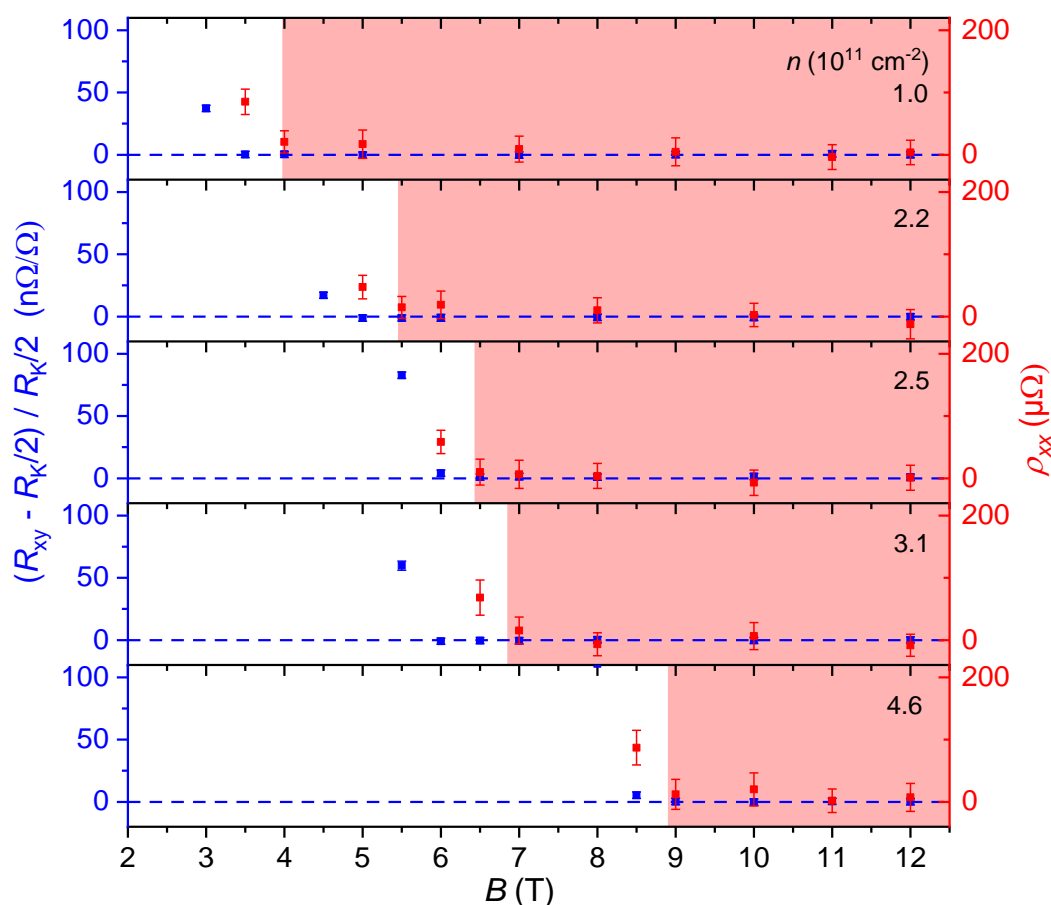


Figure 5.3 Precision measurements of Hall and longitudinal resistance as a function magnetic field of the F4-TCNQ doped devices (5L doping stack) at 4.2 K and $I = 38 \mu\text{A}$, ordered according to their electron density. The quantization regime ($\rho_{xx} \leq 21 \mu\Omega \pm 23 \mu\Omega$) ($k = 2$) is marked in red. As the electron density increases, the onset of the quantization regime shifts to higher magnetic fields. In the quantum regime, the relative deviation of the QH resistance R_{xy} from $R_K/2$ is $< (0.7 \pm 2.6) \text{ n}\Omega/\Omega$.

Due to the wide range of carrier densities that can be controlled in graphene, the QHR devices were measured using high-accuracy measurements at different electron/hole densities. Figure 5.3 shows the relative deviation of R_{xy} from $R_K/2$ and the longitudinal resistivity ρ_{xx} plotted as a function of the magnetic field for different electron densities n_e . The devices exhibit the same trend, where the onset of the quantization regime shifts to higher magnetic fields with increasing electron density. The vanishing longitudinal resistivity within the uncertainty is a reliable criterion to determine the onset of the quantization regime, in which the deviation of the QHR

is within an accuracy of 10^{-9} . These results imply that the onset of the quantization regime is correlated with the electron density.

5.2.2 n-type QHR standards with different doping stacks

So far, the F4-TCNQ doping procedure has been focused on 5-layer doping stacks that have been systematically investigated in various studies as well as in this thesis. [49–51] To simplify this doping procedure, we explore the potential limits of the F4-TCNQ doping method by investigating graphene QHR standards with 2- and 3-layer doping stacks. The structure of the 2- and 3-layer doping stacks is presented previously in Figure 4.4, and the details of preparation are summarized in Table 5-1. The high-accuracy measurement shows excellent resistance quantization with an accuracy of a few $n\Omega/\Omega$ at 4.2 K over a wide QH plateau in Figures 5.4 and 5.5.

Table 5-1. The graphene QHR standards were doped by F4-TCNQ with a 2-, 3-, and 5-layer doping stack.

Device	Volume ratio	Pre-annealing	Doping stack	Carrier density (cm^{-2})	Mobility ($\text{cm}^2\text{V}^{-1}\text{s}^{-1}$)
G1536_4(chip5)	50:100	Vacuum	2L	2.30×10^{11}	4263
G1517_11(chip45)	5:100	H ₂	3L	4.30×10^{11}	4392
G1514_12(chip50)	5:100	Vacuum	3L	5.40×10^{11}	6675
G1515_11(chip38)	5:100	H ₂	5L	2.50×10^{11}	4631

Figure 5.4 shows the relative deviation of R_{xy} from $R_K/2$ and the longitudinal resistivity ρ_{xx} as a function of the magnetic field with different electron densities of a 3-layer doping stack device at 4.2 K and $I = 38 \mu\text{A}$. The quantization regime was observed in high magnetic fields above 7 T. As the electron density increases, the onset of the quantization regime shifts to higher magnetic fields, which is consistent with the trend observed in 5-layer doping stack devices.

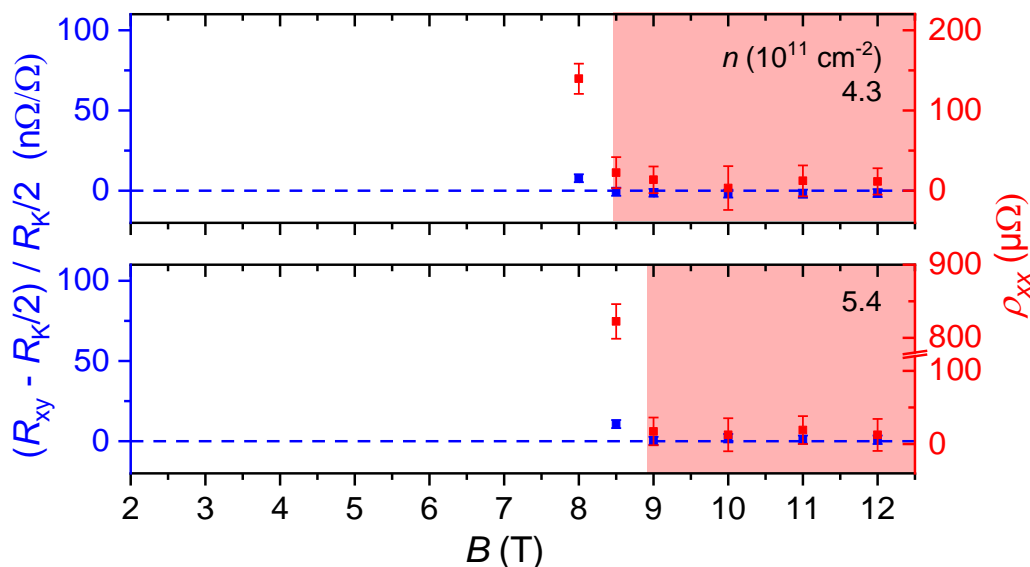


Figure 5.4 Precision measurements of the F4-TCNQ doped devices with 3L-doping stack. The relative deviation of R_{xy} from $R_K/2$ and the longitudinal resistivity ρ_{xx} as a function of the magnetic field with different electron densities at 4.2 K and $I = 38 \mu\text{A}$. The quantization regime ($\rho_{xx} \leq 21 \mu\Omega \pm 23 \mu\Omega$) ($k = 2$) is marked in red. As the electron density increases, the onset of the quantization regime shifts to higher magnetic fields. In the quantum regime, the relative deviation of the QH resistance R_{xy} from $R_K/2$ is $< (0.7 \pm 3) \text{ n}\Omega/\Omega$.

Figure 5.5 shows high-accuracy measurements of the graphene-based QH devices with 2-layer, 3-layer, and 5-layer doping stacks. The carrier densities are reduced to the desired level of 10^{11} cm^{-2} and are very similar despite the different layer sequences. The onset of the quantization regime occurs at magnetic field values B_{on} of 5 T, 6.5 T, and 8.5 T in the QHR standards with 2-, 5- and 3-layer stacks, respectively. This onset of the quantization regime in magnetic field exhibits a correlation with the electron density, as previously discussed in Section 5.2.1. All three QHR standards exhibit excellent resistance quantization, with relative deviations of the QH resistance R_{xy} from $R_K/2$ within $2 \pm 3 \text{ n}\Omega/\Omega$ (combined uncertainties, $k = 2$) throughout the entire accessible QH plateau range. The 2-layer device with the lowest carrier density of $n = 2.3 \times 10^{11} \text{ cm}^{-2}$ shows a QH plateau onset at $B_{\text{on}} = 5 \text{ T}$, which extends over the entire range up to 12 T.

The compact table-top cryostats are equipped with a small superconducting magnet, which can achieve magnetic fields up to 6 T. The 2-layer QHR device can achieve the high accuracy in magnetic fields below 6 T, making it suitable for metrological applications in table-top cryostats.

The results demonstrate the excellent metrological quality of graphene-based QHRs with F4-TCNQ doping stacks of 2-, 3-, and 5-layers. There is no preference for any of the three investigated layer sequences as long as the required carrier density is obtained. The ability to use different doping stacks enables greater flexibility in the device fabrication for applications in quantum Hall resistance metrology.

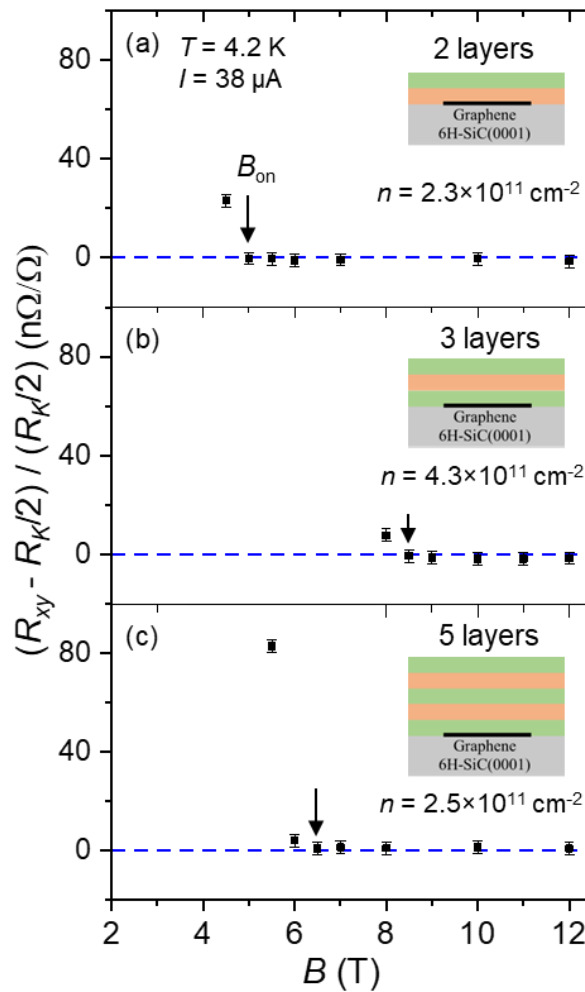


Figure 5.5 The relative deviation of the dc QH resistance R_{xy} from the quantized value $R_K/2$ obtained by CCC measurements at 4.2 K and $I = 38 \mu\text{A}$ of graphene-based QHR devices with (a) 2-layer, (b) 3-layer, and (c) 5-layer doping stacks. The insets sketch the corresponding doping stack with the doped layer (F4-TCNQ in PMMA host matrix) in red and the undoped co-polymer spacer and cap layer in green on top of the monolayer graphene (black).

5.2.3 Comparison to commercial QHR device

Graphensic AB, a Swedish company founded in 2011 as a start-up spin-off from Linköping University, is the first supplier of epitaxial graphene in Europe. They are world leaders in

providing high-quality epitaxial graphene and graphene-based devices, including epitaxial graphene QHR standards.

In this thesis, we compared the performance of our graphene QHR standard with that of the Graphensic QHR standard, as shown in Figure 5.6. Both devices have an electron density of $1.0 \times 10^{11} \text{ cm}^{-2}$. As previously mentioned, the quantization regime is defined by $\rho_{xx} = 0$ within the uncertainty $\pm 23 \mu\Omega$. The PTB QHR device exhibits zero longitudinal resistance within the error bar in a magnetic field range of 4 T to 12 T, indicating the quantization regime. The corresponding quantized Hall resistance with a relative deviation of $(R_{xy} - R_k/2)/(R_k/2) \leq (2.0 \pm 2.6) \text{ n}\Omega/\Omega$ at filling factor 2. The Graphensic QHR device showed that the longitudinal resistance deviates from zero by $\approx 50 \mu\Omega$ in the magnetic field range of 5 T to 12 T, indicating imperfect quantization of the Hall resistance. In contrast, the graphene QHR in this thesis showed vanishing longitudinal resistance within the uncertainty $\pm 23 \mu\Omega$ in a wide magnetic field range, speaking for a superior performance compared to the commercial QHR device.

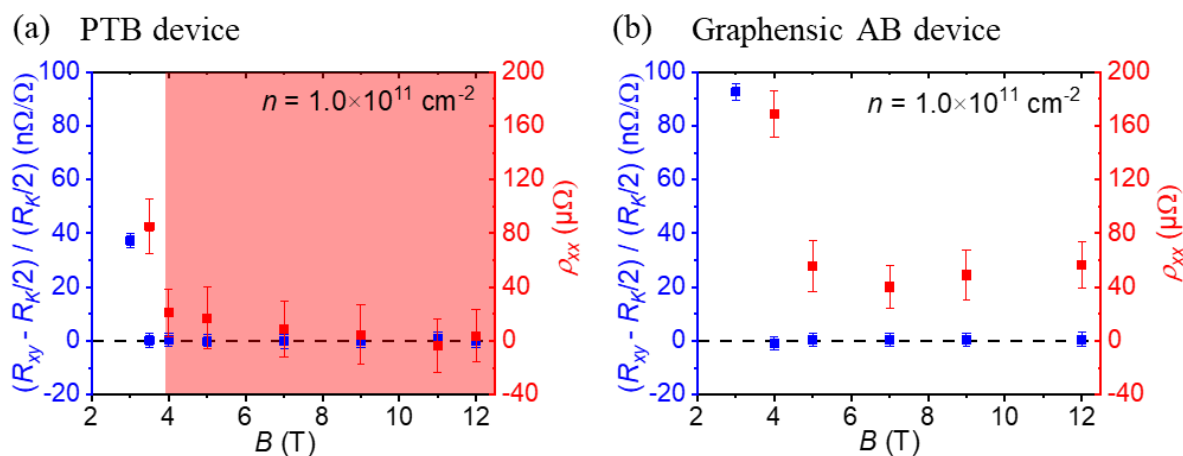


Figure 5.6 Relative deviation of $(R_{xy} - R_k/2)$ from $R_k/2$ and longitudinal resistivity of ρ_{xx} as a function of the magnetic field. The graphene QHR standard from (a) this thesis is compared with (b) the commercial counterpart from the Graphensic AB company. Both devices have the same electron density of $1.0 \times 10^{11} \text{ cm}^{-2}$. The high-accuracy measurements are performed at a current of $38.7 \mu\text{A}$ and a temperature of 4.2 K .

The nonvanishing small ρ_{xx} in the commercial device may be attributed to a second conducting path in the F4-TCNQ doping layer or graphene/SiC interface. Another possible explanation is that the disorder in the Graphensic QHR device exhibits larger energy fluctuations, which result in a wider broadening of the Landau level and wider localized states. When the Fermi energy

is close to the mobility edge of the extended state of the Landau level, variable range hopping transport may contribute to the longitudinal resistance.

In the high-accuracy measurements, $(R_{xy} - R_k/2)/(R_k/2) = 0$ within the uncertainty indicates that the QHR has achieved accuracy on the $n\Omega/\Omega$ level for the application of resistance metrology. The PTB QHR device achieves accuracy on the $n\Omega/\Omega$ level in a magnetic field as low as 3.5 T, while the Graphensic QHR device achieves the same accuracy in a higher magnetic field, starting at 4.0 T. At the same electron density, the PTB QHR device achieved the $n\Omega/\Omega$ accuracy at a lower magnetic field. At a magnetic field of 3.0 T, the value of $(R_{xy} - R_k/2)/(R_k/2)$ of the PTB device slightly increases to 37 $n\Omega/\Omega$. This value is smaller than that of the Graphensic device (≈ 92 $n\Omega/\Omega$). A possible explanation for these two results is that the lower fluctuation of disorder energy of the PTB QHR device results in a smaller broadening of the Landau level. Therefore, the quantized Hall resistance is observed in a lower magnetic field.

The high-accuracy measurement results demonstrate that the graphene QHR device in this thesis exhibits quantized Hall resistance with $n\Omega/\Omega$ accuracy at lower magnetic fields and lower longitudinal resistance compared to the Graphensic QHR device. Thus, our QHR device presents advanced performance for resistance metrology applications in NMIs and industry.

5.3 Contour plot of the quantization regime of the *n*-type graphene QHR standards

The systematic high-accuracy measurements from devices with different carrier densities found that the onsets of the deviation and quantization regimes are correlated with the electron density. Figure 5.7 presents the deviation and quantization regimes as a function of the corresponding electron density in the contour plot. The electron density of $n_e = 1.0 \times 10^{11} \text{ cm}^{-2}$ is a special point in the contour plot, where the Hall resistance quantization is observed at the lowest magnetic field of 4.0 T at 4.2 K. In the region of electron density $n_e \geq 1.0 \times 10^{11} \text{ cm}^{-2}$, as the electron density decreases, the onset of the quantization regime shifts to lower magnetic fields, while the end of the quantization regime extends at least up to 12 T, which is the maximum magnetic field in the setup. In the region of electron density between $0.5 \times 10^{11} \text{ cm}^{-2}$ and $1.0 \times 10^{11} \text{ cm}^{-2}$, as the electron density decreases, the width of the quantization regime gradually shrinks in the high-accuracy measurement (accuracy on the level of $n\Omega/\Omega$), even though the very wide plateau is still observed in magnetotransport. Specifically, the finite width of the quantization regime is observed in a magnetic field range from 5 T to 12 T at an electron density

5.3 Contour plot of the quantization regime of the n-type graphene QHR standards

of $n_e = 9.3 \times 10^{10} \text{ cm}^{-2}$ and from 6 T to 8 T at an electron density of $n_e = 6.7 \times 10^{10} \text{ cm}^{-2}$. The onsets (ends) of the quantization regime are marked by filled (open) symbols in Figure 5.7. At electron densities below $0.5 \times 10^{11} \text{ cm}^{-2}$, the quantum Hall resistance deviates from the theoretical value R_K , resulting in a loss of the high accuracy level of $n\Omega/\Omega$. Moreover, the longitudinal resistance deviates significantly from zero to a few hundreds of $\mu\Omega$ in the high-accuracy measurements.

Figure 5.7 illustrates the correlation between the quantization regime and the electron density (zero field) that is valid for the 5L doping stack devices. The quantization regime of the 3L and 2L doping stack devices were also evaluated using the same high-accuracy measurements, and the corresponding data is consistent with the results of the 5L devices. This indicates that the observed correlation between the quantization regime and the electron density is a general behavior of the state-of-the-art epitaxial graphene QHR standards.

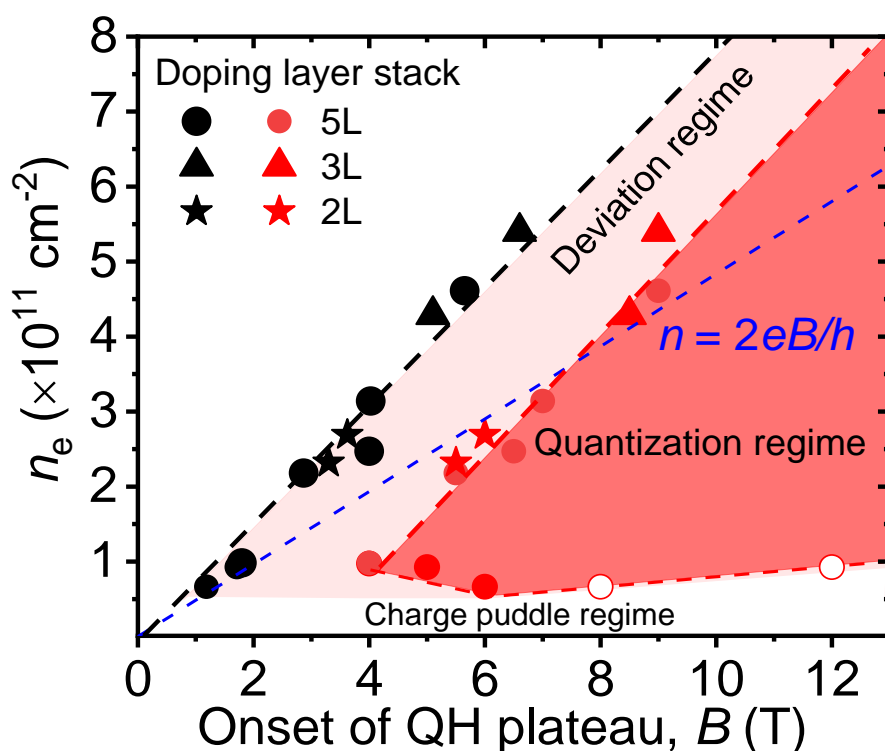


Figure 5.7 The contour plot presents the deviation and quantization regime as a function of the electron density and magnetic field for *n*-type graphene QHR standards, which include the devices with 5L-, 3L, and 2L doping stacks. The onset of the deviation and quantization regime is determined by the longitudinal resistivity $\rho_{xx} \leq 100 \text{ m}\Omega$ and $\rho_{xx} = 0$ within uncertainty, respectively. The open symbols mark the end of the quantization regime. The blue dashed line represents the carrier density for the filling factor $\nu = 2$ in the absence of charge transfer. Adapted from the Ref. [51]

In the absence of electron transfer process in graphene, the center position of the Hall plateau in a magnetic field is a function of electron density, as shown by the blue line in Figure 5.7. [44] However, the existing theory fails to describe the center position of the Hall plateau ($\nu = 2$) in a magnetic field. Epitaxial graphene exhibits an extraordinarily broad Hall plateau ($\nu = 2$), and the center position of the Hall plateau shifts to a higher magnetic field due to the charge transfer in a magnetic field. [111,141] Currently, there is no comprehensive theory or model to describe the correlation between the quantization regime and the electron density in epitaxial graphene. According to the systematic experimental results, the contour plot serves as a two-dimensional map that guides the deviation and quantization regime in a magnetic field. Thus, the contour plot is a benchmark for evaluating the quantization regime of an epitaxial graphene QHR standard with a specific electron density. This provides a highly practical benefit for the application of graphene QHR standards in quantum resistance metrology.

The field-dependent charge transfer model has been used to describe the Fermi energy pinning of epitaxial graphene in quantum transport. [111,141,142] The contour plot of the quantization regime provides further experimental evidence supporting this model. In the absence of charge transfer, the center position of the Hall plateau at the filling factor ν as a function of carrier density and magnetic field is described by the relation $n = \nu eB/h$. This linear dependence relationship is plotted as the blue dashed line for the filling factor $\nu = 2$ in Figure 5.7. This relation determines the centers of the QH plateau of classical semiconductors, e.g., GaAs/AlGaAs, 2DEG devices with constant carrier density. The contour plot shows that the quantization regime (extended beyond 12 T) is observed on the right side of the blue dashed line, indicating the centers of the Hall plateau at $\nu = 2$ located at a higher magnetic field (right side of the blue dashed line). This observation contradicts the theoretical model in the absence of charge transfer process. Based on the center of the Hall plateau ($\nu = 2$) to the right of the theoretical curve, we can deduce that the carrier density of epitaxial graphene in a magnetic field is much higher than the zero-field carrier density. This provides additional experimental evidence proving the existence of a magnetic field-dependent charge transfer process in epitaxial graphene, in addition to the evidence in the literature. [111,141]

In a graphene device with a specific electron density, the onset of the quantization regime is determined by the temperature and broadening of the extended state of the Landau level. The contour plot in Figure 5.4 shows the relationship between the quantization regime and the electron density but is only valid for the given temperature of $T = 4.2$ K and current of $I = 38$ μ A. Any change in temperature (or current) will directly impact the onset of the quantization

regime. The temperature-dependent high-accuracy measurements were carried out on the graphene QHR device. The results show a shift of the QH plateau (quantization regime) by about 1 T to higher B -values for a temperature change of 2 K (from 2.2 K to 4.2 K) [53]. This shift is typical for epitaxial graphene. [47,48,142] Thus, this result proves that reducing the temperature causes the onset of the quantization regime to shift to a lower magnetic field.

It should be possible that the onset of the quantization regime could shift to a lower magnetic field by reducing the disorder in epitaxial graphene. This is due to the less broadening of the extended state of the Landau level. According to the data presented in Figure 5.5, the width of the deviation regime is estimated to be about 2 - 3 T. The deviation of quantum Hall resistance in this regime is attributed to the disorder that caused the broadening of the Landau level. It is expected that by reducing disorder in epitaxial graphene, the regime of accurate resistance quantization can be achieved at even lower magnetic fields.

The Hall resistance quantization at 4.2 K and 4 T simplifies the experimental measurement set-up in quantum metrology compared to conventional GaAs-based resistance standards, which require 1.5 K and 10 T. It is further desirable to shift the quantized Hall regimes to lower field values. To achieve this, it is necessary to further reduce the disorder in epitaxial graphene, such as by suppressing the formation of charge puddles at low carrier densities.

5.4 *p*-type graphene QHR standards

The QHE is a universal phenomenon observed in a variety of materials, including two-dimensional conductors, silicon MOSFETs, [34] semiconductor heterostructures like AlGaAs/GaAs, [143] or metaloxides ZnO/Mg_xZn_{1-x}O. [144] Furthermore, the QHE has been observed not only in electrons but also in quasiparticle transport like composite fermions undergo Hall quantization and give rise to the fractional QHE. [145–147]

In 2004, a semimetal called graphene [16,32], enabled the investigation of QH physics of quasi-relativistic “massless” electrons, so-called Dirac fermions. [19] The specific band structure of this new material results in large energy splitting of the Landau levels which theoretically allow resistance quantization up to room temperature. [43] This aroused the interest of National Metrology Institutes around the world when considering that conventional QHR standards from AlGaAs/GaAs heterostructures need low temperatures of 1.5 K and magnetic fields of about 10 T for the realization of the unit ohm with a state-of-the-art accuracy on the level of 1 nΩ/Ω. [8,148–155]

The great progress achieved in the last decade has led to nowadays' graphene-based QHRS operating under relaxed experimental conditions, typically at 4.2 K, magnetic fields below 5 T, or improved current robustness. [51,53,139] Today's graphene QHR standards have *n*-type conductivity, which is related to the intrinsic properties of as-grown epitaxial graphene on SiC substrates. [29,126]

In this work, we investigate *p*-type epitaxial graphene QHRS for the realization of SI unit ohm. The *p*-type epitaxial graphene is molecularly doped by F4-TCNQ, as discussed in Chapter 4. The accurate resistance measurements indicate that the quantized resistance ($\nu = 2$) of all *p*-type QHR standards is in good agreement within a few $n\Omega/\Omega$ with the nominal value of $R_K/2$ over a wide QH plateau range. This result is consistent with the *n*-type counterpart. It shows that QHR standards for the practical realization of SI unit ohm can be fabricated from graphene with both polarities. This gives further confidence in the universality of the QHE as the basis of the ohm realization. A detailed comparison of both types of devices reveals differences, and possible origins are discussed.

The F4-TCNQ molecular doping technique can control the carrier density from the *n*-type to the *p*-type regime, enabling the creation of *p*-type devices for the QHR standard. In this section, the *n*-type graphene QHR devices are obtained through a combination of vacuum annealing and F4-TCNQ doping, while the *p*-type graphene QHR devices are obtained through F4-TCNQ doping without any annealing process. A 5-layer doping stack was spin-coated on the graphene surface to control the carrier density in graphene. The procedures for annealing and F4-TCNQ doping have been previously described. The doping layer consists of a mixture of F4-TCNQ/anisole and PMMA, with a volume ratio of 50% for *p*-type graphene and 25% for *n*-type graphene. The graphene growth, device fabrication, magnetotransport, and high-accuracy measurements follow the procedure described in Chapter 4.

5.4.1 Magnetotransport of *p*-type QHR standards

The F4-TCNQ doped graphene QHR devices show a clear signature of doping. Compared to the high electron density of up to $1 \times 10^{13} \text{ cm}^{-2}$ of as-grown epitaxial graphene, [29] the *n*-type device shows a strongly reduced value of $n_e = 1.10 \times 10^{11} \text{ cm}^{-2}$. The *p*-type device has a hole density of $n_h = 1.15 \times 10^{11} \text{ cm}^{-2}$, which indicates a Fermi level shift from *n*-type to *p*-type across the charge neutrality point. Because of the similar carrier density values of the *n*-type and the *p*-type device, the Hall curves show a similar mirror image behavior, see Figure 5.8. A broad QH Hall plateau at filling factor $\nu = 2$ (filled 0th Landau level) with a resistance value

corresponding to half of the von Klitzing constant is observed for both devices. The QH plateaus start at a magnetic field of about 3 T and extend at least up to 12 T, which is the maximum magnetic field of the cryostat.

Both graphene devices show a comparable weak localization peak at zero magnetic field in the longitudinal resistivity curves (inset of Figure 5.8). [156] The ρ_{xx} value of the *p*-type device is about twice as high as that of the *n*-type one, which results in a lower *p*-type Hall mobility value ($\mu_h = 4380 \text{ cm}^2/\text{Vs}$ compared to $\mu_e = 8954 \text{ cm}^2/\text{Vs}$) and indicates a different scattering behavior of holes and electrons in the low-temperature transport regime.

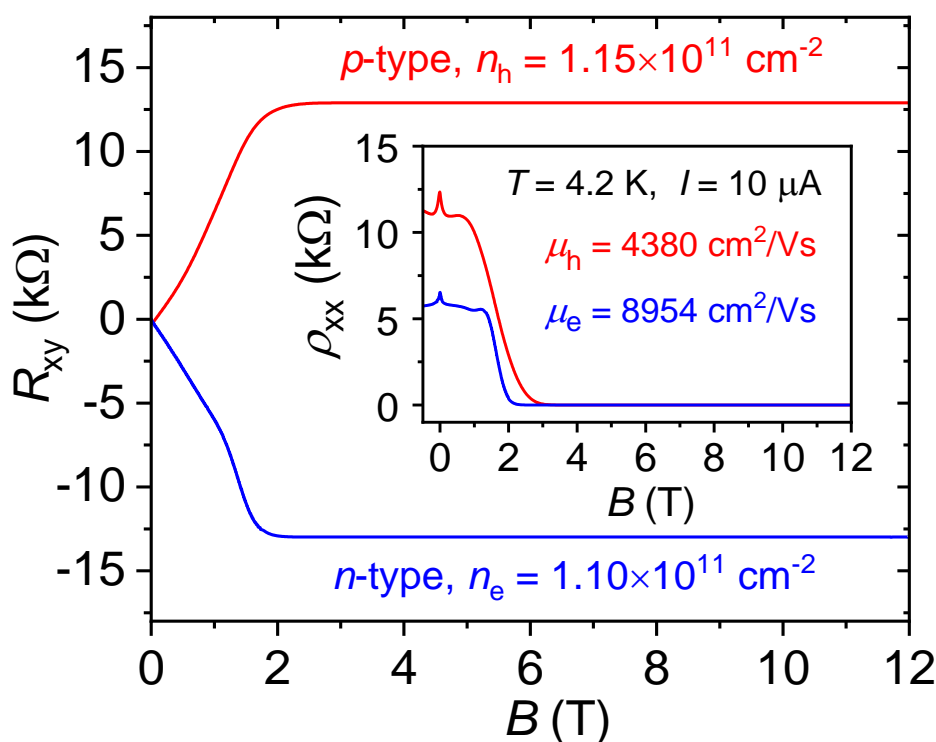


Figure 5.8 The QHE measurement of the *p*- and *n*-type graphene QHR device at 4.2 K. The different Hall slopes from the Hall measurement in low magnetic field indicate different charge carriers in graphene. Insert shows the longitudinal resistivity as a function of the magnetic field. The calculated mobility is $8954 \text{ cm}^2/\text{Vs}$ for electrons and $4380 \text{ cm}^2/\text{Vs}$ for holes.

At a low temperature of 4.2 K, the mobility in graphene is primarily affected by the charge impurity scattering and neutral atom defect scattering. [121,122,124,157] These scattering centers are the main sources of disorder in graphene, which modify the Fermi energy profiles of the graphene sheet at the local sites, resulting in the broadening of the Landau level in a magnetic field. Stronger scattering for *p*-type graphene gives rise to a larger broadening of the Landau level.

In the high magnetic field, the *p*-type devices exhibit a wide QH plateau at filling factor two, similar to the *n*-type device. In Figure 5.8, the Hall plateaus start at a magnetic field of about 2 T and extend up to 12 T, which is the maximum magnetic field of the system. Such wide QH plateaus are typically observed in epitaxial graphene devices due to the strong pinning of the Fermi level in magnetic field.

5.4.2 High-accuracy measurement of *p*-type QHR standards

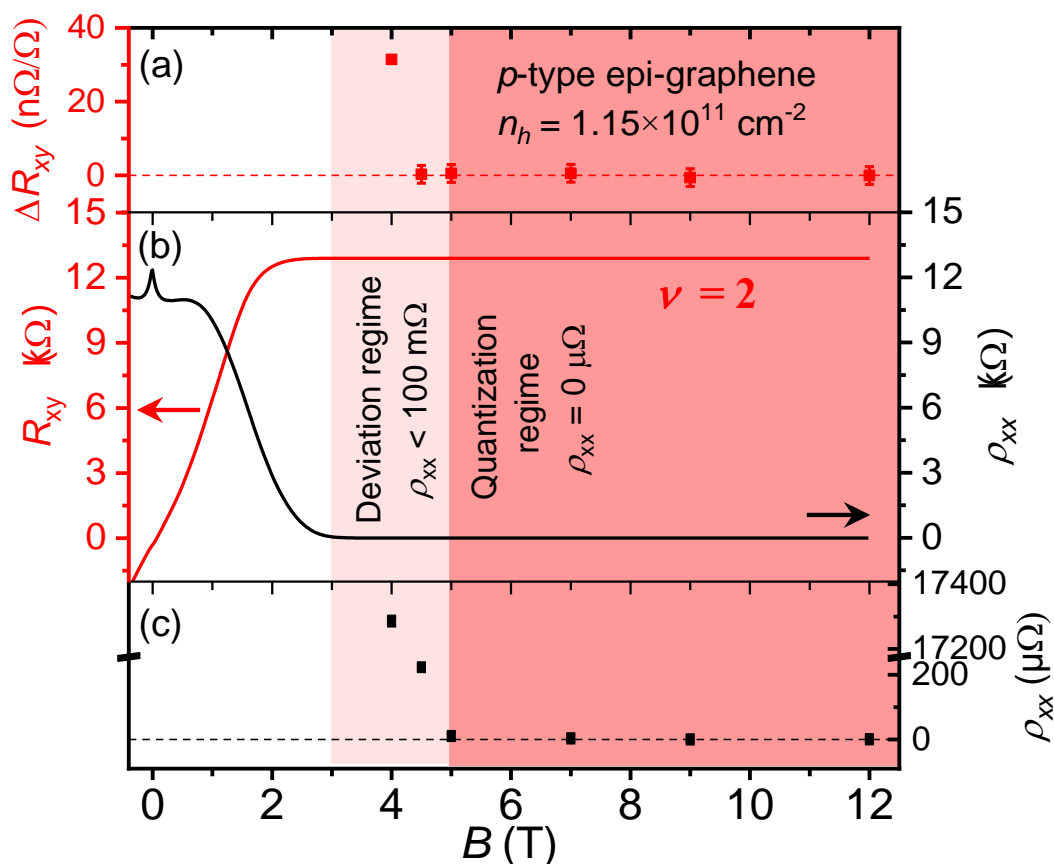


Figure 5.9 The magnetotransport (b) and high-accuracy (a, c) measurement of the *p*-type QHR device (G1491-I10-1_2Bath) doped by F4-TCNQ (5L doping stack). (b) Hall resistance R_{xy} and longitudinal resistivity ρ_{xx} as functions of the magnetic field from a graphene QHR device with hole density $1.15 \times 10^{11} cm^{-2}$ at 4.2 K. The deviation regime is at magnetic fields from 3.2 T to 5 T for this device, corresponding to the longitudinal resistivity $\rho_{xx} < 100 m\Omega$. High-accuracy measurement of (a) the Hall resistance deviation $(R_{xy} - R_K/2) / (R_K/2)$ and (c) the longitudinal resistivity ρ_{xx} on the $\nu = 2$ plateau at 4.2 K and $I = 38 \mu A$. The relative deviation of the Hall resistance R_{xy} from $R_K/2$ is less than $(0.6 \pm 2.4) n\Omega/\Omega$ ($k = 2$) in the magnetic field from 5 T to 12 T. The quantization regime is defined by $|\rho_{xx}| = 0 \mu\Omega$ with the uncertainty of $\pm 15 \mu\Omega$ ($k = 2$). Here, the onset of the quantization regime is at $B = 5$ T.

The results of the high-accuracy measurements of R_{xy} and ρ_{xx} of the *p*-type graphene QHR standard are presented in Figure 5.9(a) and (c). By contrast, Figure 5.9(b) shows the corresponding overview measurement (with a low accuracy of about 10^{-4}). The quantization regime, identified by $\rho_{xx} = 0$ within an uncertainty of $\pm 15 \mu\Omega$, is represented by a red area in Figure 5.9. The quantization regime starts at 5 T, and the excellent quantization continues up to 12 T, which is the technical limit of the setup. In this magnetic field range, the Hall resistance quantization achieves an accuracy of $|(R_{xy} - R_K/2) / (R_K/2)| < (0.6 \pm 2.4) \text{ n}\Omega/\Omega$, see Figure 5.9(a). This level of accuracy is equal to that of conventional GaAs-based [40,41,86] and *n*-type graphene QHR standards for the given measurement configuration. [8,48,139,158,159] This result verifies the high quality of the *p*-type graphene QHR standards being as good as the *n*-type counterpart for the realization of the SI ohm in quantum resistance metrology.

The high-accuracy measurements in the Hall plateau identify a deviation regime and a quantization regime, which was not recognized in graphene and GaAs QHR standards in previous studies in the literature. The deviation regime is defined by a longitudinal resistivity of $0 < \rho_{xx} < 100 \text{ m}\Omega$, as marked by the light red area. The measurements in Figures 5.9(b) and (c) show that the deviation regime (sketched as a light red area) spans from about 3 T to 5 T, in which the QHR deviates from the nominal $R_K/2$ value. This result reveals that the quantized Hall resistance R_{xy} with an accuracy of $\text{n}\Omega/\Omega$ starts at $B = 5.0 \text{ T}$ rather than 3.0 T in the very wide plateau ($\nu = 2$). In this *p*-type device, the onset of the deviation regime is about 2 T lower than that of the quantization regime, which is similar to the behavior observed in *n*-type QHR devices. The difference of about 2.0 T can be used to estimate the onset of the quantization regime from magnetotransport measurement with less accuracy.

Please note, although the longitudinal resistivity deviates from zero to $223 \mu\Omega$ at 4.5 T, the relative deviation of the Hall resistance is still $(0.6 \pm 2.4) \text{ n}\Omega/\Omega$, indicating that quantized resistance with an accuracy of $\text{n}\Omega/\Omega$ is still maintained at the magnetic field as low as 4.5 T, as shown in Figure 5.9 (c). This is due to the very small s parameter, which quantifies how strongly the emerged ρ_{xx} mixed into the R_{xy} in each QHR standard device. For this device, the minor longitudinal resistance $\rho_{xx} = 223 \mu\Omega$ at 4.5 T has a negligible contribution to the quantum Hall resistance. Thus, the highly accurate quantized resistance is maintained. At low temperatures, such a small value of ρ_{xx} is caused by the variable range hopping. This behavior has also been observed in *n*-type graphene QHR devices. [51]

5.4.3 Contour plot of *p*-type QHR standards

The Hall quantization of seven additional *p*-type graphene devices was investigated by accurate ρ_{xx} and R_{xy} measurements in the accessible magnet field range at intervals of 1 T and 4.2 K. The quantization and the deviation regime were again determined according to the above-mentioned criteria and the onset values are plotted in Figure 5.10.

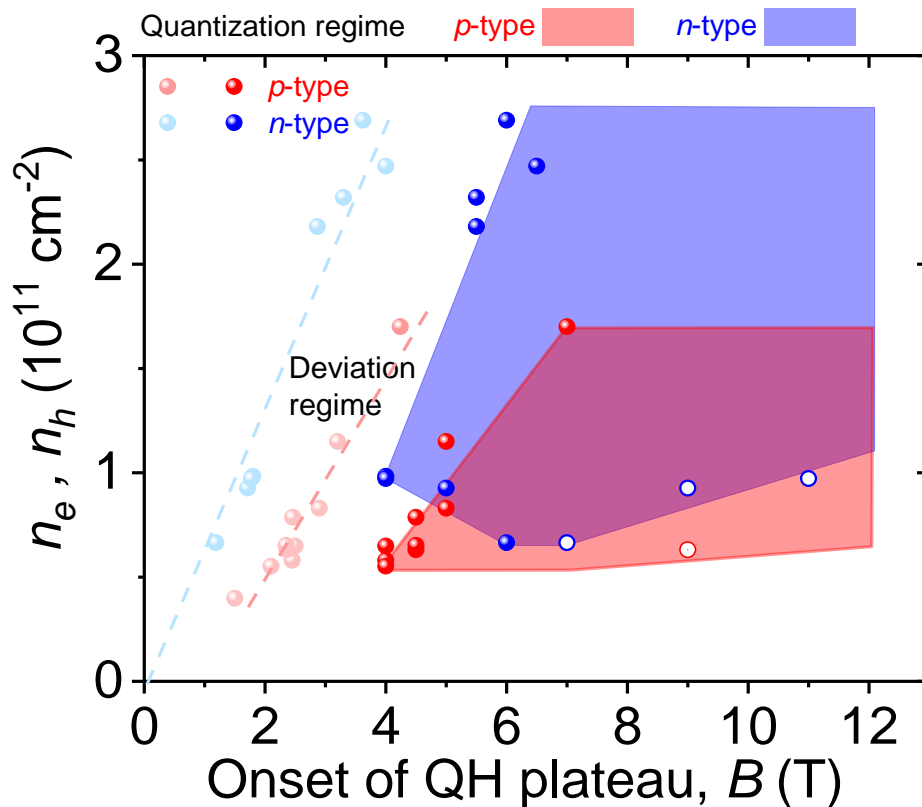


Figure 5.10 The contour plot of the deviation and quantization regimes as a function of the hole density and magnetic field for the 5L-doping stack QHR devices. The onsets of the deviation and quantization regimes are determined by the longitudinal resistivity $\rho_{xx} \leq 100 \text{ m}\Omega$ and $\rho_{xx} = 0$ within uncertainty, respectively. The blue symbols present the onsets of the deviation and quantization regimes of the *n*-type QHR devices. The red symbols present the onsets of the deviation and quantization regimes of the *p*-type QHR devices. The open symbols mark the end of the quantization regime. The onsets of deviation and quantization regimes of the *p*-type devices shift to the higher magnetic fields in comparison with that of the *n*-type devices.

The quantization regime (red area) of the QHR devices with different hole densities $n_h > 6 \times 10^{10} \text{ cm}^{-2}$ extends over a wide magnetic field range up to at least 12 T, akin to the result shown before in Figure 5.9 This convincing result proves that *p*-type graphene devices are excellently

suited as QHRS with an equal high accuracy as the *n*-type ones. Only for the lowest density device of $n_h = 5.5 \times 10^{10} \text{ cm}^{-2}$, the end of the quantization regime was observed at 9 T (open red dot). The minor emerged ρ_{xx} at $B > 9 \text{ T}$ can be explained as an incomplete filling of the 0th Landau level and a depletion of the charge reservoir in the charge transfer model. [160]

The quantization regime of *n*-type graphene devices is also plotted as a blue area in Figure 5.10 [51]. On the first view, the behavior of *n*- and *p*-type devices looks qualitatively similar. With increasing (zero-field) carrier density, the onsets of deviation and quantization regime shift to higher B field values. Another similarity of the *p*- and *n*-type devices can be observed in Figure 5.10. The width of the deviation regime is about 2 T for both *n*- and *p*-type devices. This allows to estimate the onset of the quantization regime from a simple magnetotransport measurement in resistance metrology.

Moreover, a very broad Hall plateau is also observed in the *p*-type epitaxial graphene, similar to the *n*-type graphene. The wide QH plateau ($\nu = 2$) in *n*-type epitaxial graphene was explained by the so-called charge-transfer model. [141,160,161] Due to strong pinning of the Fermi level in the magnetic field, the electrons persistently transfer from the charge reservoir to the graphene Landau level with increasing magnetic field. The charge reservoir originates from the donor-like states, which are located on the SiC surface and in the buffer layer. These donor-like states are partially filled (neutrality) and partially empty (positive charge). The charge transfer model suggested in *n*-type graphene can also be applied to the *p*-type epitaxial graphene. From the similarity, one can conclude an ambipolarity of these states, which can also transfer holes to *p*-type epitaxial graphene, e.g., the positively charged Silicon dangling bonds receive electrons (lost holes) from graphene.

At equal carrier density values, the onset of the deviation and quantization regimes is observed at higher magnetic fields for *p*-type graphene compared to the *n*-type counterpart. To explain the non-symmetric of the QH plateau in Figure 5.10, we provide two possible explanations. According to the charge transfer model, the carrier density in the Landau band is increasing at higher magnetic fields. Thus, the differences in the QH plateau onset could indicate a non-symmetric charge transfer for holes and electrons, e.g., by a different density of the charge-reservoir states at the different Fermi level positions or the higher density of acceptor states in the *p*-type devices which also play a role for the charge balancing in the graphene layer.

The observed non-symmetric onset of the deviation and quantization regimes could also be correlated with a higher degree of disorder of the *p*-type graphene, which results in a wider broadening of Landau levels in the QH transport. Therefore, we systematically investigated the

mobility as a function of the carrier density of the *n*- and *p*-type devices, as shown in Figure 4.2 previously. Each data point is extracted from an individual device and a Hall measurement at 4.2 K. We indeed observed an asymmetric dependence of mobility on carrier density for electrons and holes between 10^{10} and 10^{11} cm^{-2} . The lower mobility values of the *p*-type devices indicate a stronger charge carrier scattering, which suggests a higher degree of disorder in the transport channel. The stronger scattering in *p*-type epitaxial graphene was also observed in another paper. [162] The lower mobility in Figure 4.4 and the lower phase coherence length and localization length proved in Ref. [162] indicate a higher degree of disorder and wider broadening of Landau levels in *p*-type than *n*-type epitaxial graphene. The asymmetric scattering behavior of both carrier types is possibly related to different contributions of short-range and long-range Coulomb scattering. [124,163,164] To this point, the observed non-symmetric mobility of *n*- and *p*-type graphene is not yet clear, and the arising open questions stimulate further research, e.g., a comparison to the behavior of gated devices with electro-static charge-control.

5.5 Temperature-dependent QHE in high magnetic fields

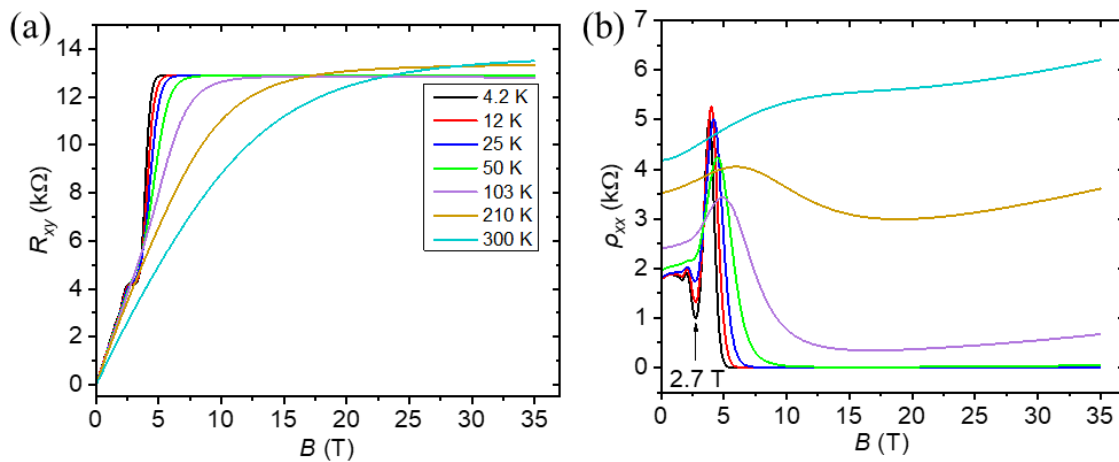


Figure 5.11 QHE measurements in high magnetic fields up to 35 T. (a) The Hall resistance R_{xy} and (b) the longitudinal resistivity ρ_{xx} as a function of magnetic field at temperatures from 4.2 to 300 K for device G1594-D6_3(chip1)2 HFML. The applied current is $10 \mu\text{A}$ in the QHE measurements.

We investigated the temperature dependence of the Hall resistance quantization in high magnetic fields up to 35 T during a measurement campaign in the High Field Magnet

5.5 Temperature-dependent QHE in high magnetic fields

Laboratory in Nijmegen, the Netherlands. Figure 5.11 plots a typical quantum Hall measurement (device G1594-D6_3(chip1)2 HFML) of a graphene QHR device at temperatures ranging from 4.2 to 300 K in high magnetic fields up to 35 T. The electron density of this device is $3.28 \times 10^{11} \text{ cm}^{-2}$ at 4.2 K. As the temperature increases, the longitudinal resistance deviates from zero, and the Hall resistance deviates from the quantized plateau $R_K/2$ in the quantum state. At temperatures above 103 K, dissipation transport causes the breakdown of the Hall plateau and the appearance of a non-zero longitudinal resistance in high magnetic fields.

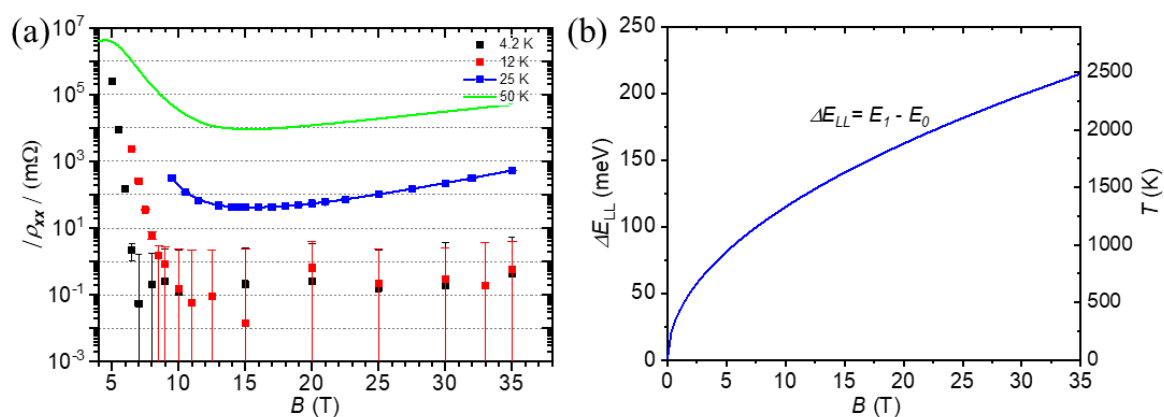


Figure 5.12 (a) The absolute longitudinal resistivity as a function of magnetic field at different temperatures in current reversal measurement. The applied current is 50 μA , and the measurement uncertainty is $\approx 2 \text{ m}\Omega$. At temperatures below 12 K, $\rho_{xx} = 0$ is observed at magnetic fields from 7 T to 35 T. At 25 K, a minimum longitudinal resistivity (30 m Ω) is observed at the magnetic field 15 T. (b) The difference energy ΔE_{LL} of the 1st and 0th Landau levels (left Y-axis) and the corresponding temperature T (right Y-axis) as a function of magnetic field.

The current reversal measurement technique can achieve an accuracy of resistance within an uncertainty of $\pm 2 \text{ m}\Omega$ at a current of 50 μA . Figure 5.12(a) shows the longitudinal resistivity as a function of magnetic fields at different temperatures. A zero longitudinal resistance is observed within an uncertainty of $\pm 2 \text{ m}\Omega$ at magnetic fields ranging from 8.5 T up to 35 T at temperatures below 12 K. As the temperature increases over 25 K, a minor longitudinal resistance starts to emerge in high magnetic field from 8 T up to 35 T, indicating the dissipative transport. This implies that the Hall resistance is not accurate quantization at temperatures above 25 K, even in very high magnetic fields with large Landau level splitting. The difference energy of the 1st and 0th Landau levels (left Y-axis) and the corresponding temperature (right Y-axis) as a function of magnetic field are shown in Figure 5.12 (b). At magnetic fields above

8 T, the difference energy of the 1st and 0th Landau levels is over 25 meV (300 K), which is far larger than 25 K.

The broadening of the Landau level is inevitable in real graphene QHR devices, due to the presence of disorder, such as charge impurities, atomic defects, atomic steps, and phonon scatterings. At low temperatures, the main sources of disorder are the charge impurities, atomic defects, and atomic steps in epitaxial graphene. At high temperatures, phonon scattering becomes the dominant disorder.

Recently, phonon-mediated room-temperature QH transport in ultra-clean hBN/graphene/hBN samples was observed. [165] In the condition of $k_B T \sim \Delta_{LL}$ and $k_B T \gg E_{ph}$, the graphene on hBN demonstrated the QHE, and electron-phonon scattering becomes the predominant mechanism in high magnetic fields. The phonon-mediated transport resulting in electron-phonon scattering can contribute to a finite longitudinal resistivity in high magnetic fields. In perpendicular magnetic fields, electron-phonon scattering requires lattice vibrations with a wave vector in the order of the inverse of the magnetic length ($l_B \approx 25 \text{ nm}/\sqrt{B[\text{T}]}$) [166]. The energy scale of phonon that contributes to electron-phonon scattering in high magnetic fields is defined as $E_{ph} = \hbar v_s/l_B$ (where v_s is the sound velocity in the material). [166] In conventional 2DESs, the QH effect is suppressed within a few K due to the small Δ_{LL} [167], where the E_{ph} -controlled phonon population can be considered negligible. In epitaxial graphene, the additional remotely interfacial phonon modes contribute to the phonon scattering in QH transport. When the graphene layer and buffer layer oscillate out-of-phase parallel to each other, a low-frequency horizontal phonon mode at 2 – 5 meV at the Γ -point [133] will occur in epitaxial graphene. As we discussed in Section 4.5.3, the low-frequency horizontal phonon E_{ph3} is about 2.0 meV, which is comparable to the thermal energy at 25 K. This mode contributes the minor resistance (30 m Ω ~ 10 Ω) in high magnetic fields at temperatures between 25 K and 100 K.

The electron density of device G1594-D6_3(chip1)2 HFML is extracted from the QH measurement at different temperatures. At 25 K (2.15 meV), the electron density is $4.05 \times 10^{11} \text{ cm}^{-2}$, corresponding to the Fermi level $E_F = 74.25 \text{ meV}$. Due to the electron transfers from the SiC to the graphene layer in the magnetic field [135,141], the Fermi level is pinned at the energy level of 74.25 meV at 15 T, as shown in Figure 5.13. In the magnetic field at 15 T, the difference energy of the 1st and 0th Landau levels is 140.49 meV. The broadening of LLs is considered as 12.00 meV in epitaxial graphene [130]. The energy gap between the Landau level mobility edge and the Fermi level is 52.24 meV, which is much larger than the thermal excitation energy at 25 K (2.15 meV). It can conclude $\Delta_{LL} \gg k_B T$ for the QH transport in epitaxial graphene at 15

T at 25 K. The thermal activation process has no contribution to the longitudinal resistivity in the 2D bulk. The emerged longitudinal resistivity at 25 K is attributed to the other reason.

As the temperature increases to 25 K, a minimum longitudinal resistivity of 30 mΩ is observed at a magnetic field of 15 T. As we discussed in Section 4.5.3, the remotely interfacial phonon $E_{ph3} = 2.0$ meV starts to dominate the scattering in epitaxial graphene at 25 K, resulting in a decrease in mobility, as shown in Figure 4.5. In QH transport at 15 T, the $E_{ph} \approx 1.76$ meV < E_{ph3} (2.0 meV) fulfills the required condition for electron-phonon scattering in a perpendicular magnetic field. Thus, at $T \geq 25$ K, the electron-phonon scattering is predominant in the QH transport. The emerged longitudinal resistivity at high magnetic fields can be explained by phonon-mediated dissipation. This implies that the dissipationless transport ($\rho_{xx} = 0$) in epitaxial graphene is limited by the remotely interfacial phonons E_{ph3} . As the temperature increases to 25 K, the phonon-mediated dissipation transport occurs in epitaxial graphene.

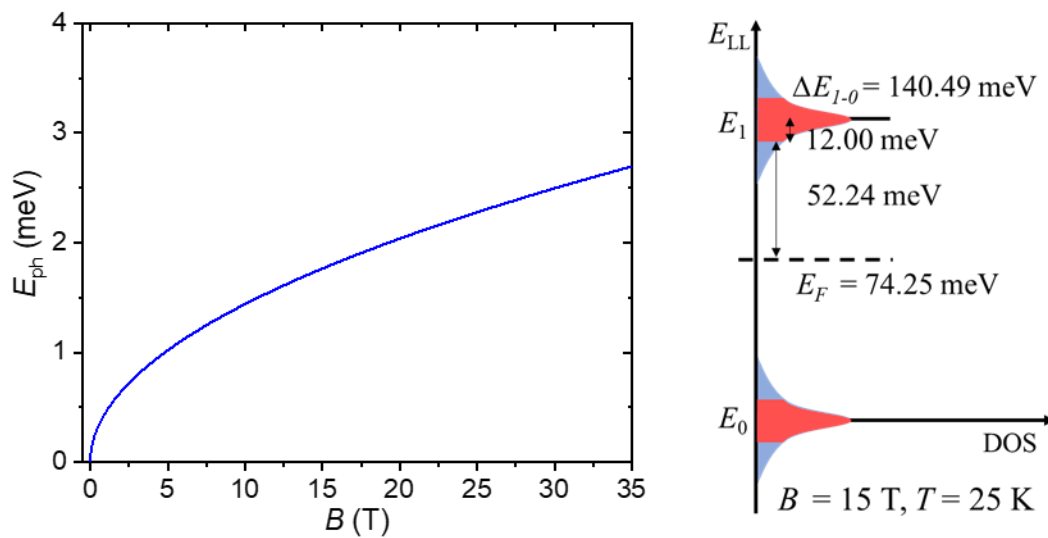


Figure 5.13 (left) the E_{ph} -controlled phonon population as a function of magnetic field. (right) The LL energy and Fermi level as a function of DOS in a magnetic field of 15 T at 25 K. The electron density at 25 K is $4.05 \times 10^{11} \text{ cm}^{-2}$, and the broadening of LLs is considered at 12.00 meV in epitaxial graphene [130].

Chapter 6. Realization of the unit ohm under relaxed experimental conditions

Quantum Hall resistance (QHR) standards play an essential role in the traceability route to the revised International System of Units (SI) ohm, farad, ampere, and kilogram (realized by a Kibble balance). The practical realization of the ohm is carried out by a conventional GaAs heterostructures QHR standard with the exact value $R_{xy} = h/2e^2$ (filling factor $\nu = 2$). In the past decade, epitaxial graphene on SiC has emerged as a promising alternative to GaAs heterostructures for QHR standards. Due to its wide splitting between the Landau levels and strong pinning of the Fermi level, epitaxial graphene allows for the realization of the SI unit of resistance under relaxed experimental conditions in terms of magnetic flux density B , current I and temperature T . Herein, we demonstrate that the epitaxial graphene QHR standards realize the SI unit ohm at $B = 4.5$ T, $I = 232.5$ μ A, and $T = 4.2$ K simultaneously. To the best of our knowledge, this is the best performance of graphene QHR standards obtained under (B, I, T) relaxed experimental conditions simultaneously. Repeated high-accuracy measurements demonstrate that the quantized resistance remained stable within an accuracy of (2 ± 3) n Ω / Ω over a period of 2.5 years, to date. Furthermore, the accuracy of the graphene QHR standards has been maintained without any indications of degradation, even after experiencing long-distance transport between two metrology institutes. It is expected that the superior performance of graphene QHR standards may lead to a broader dissemination of primary quantum standards beyond national metrology institutes, extending to calibration laboratories and industry on-site.

The content in this chapter is to be submitted to a journal. Some of the QHR devices were delivered to BIPM where the high-accuracy measurements were conducted by Dr. Pierre Gournay and Benjamin Rolland.

6.1 Introduction

To practically realize the electric SI units based on quantum physics, it is essential to develop the quantum Hall resistance (QHR) standard. This standard should be able to work under relaxed conditions simultaneously, including low magnetic field, high temperature, and high current. In addition, the QHR standard must be stable in storage conditions for a long time. Simplifying the operating conditions (B, I, T) will make the QHR standard device compatible with portable, compact, and cryogen-free setups. Improving the performance of the QHR

standard at low magnetic fields, high currents, and high temperatures can reduce calibration costs, leading to broader dissemination and proliferation of primary quantum standards beyond national metrology institutes and into the industry. However, relaxing these three experimental conditions (B , I , T) is very challenging due to the mutually constraining nature of the QHE physics. For example, to maintain the Hall resistance quantization with high accuracy, decreasing B competes against increasing I and T . Therefore, developing QHR standards that work under three relaxed experimental conditions while maintaining the high accuracy of R_{xy} quantization over the years is challenge and critical for the next generation of the practical QHR standards in metrological and industrial applications.

To address these bottlenecks of QHR standards, we developed scalable, reproducible, and long-term stable graphene QHR standards. They were fabricated from a high-quality monolayer of epitaxial graphene on SiC substrates, in which the carrier density was reduced by the F4-TCNQ molecular doping technique. These devices were stored in a closed chamber filled with a mixture of nitrogen (N_2) and dry air (humidity $\leq 40\%$) at room temperature for more than two years. From time to time, the chamber atmosphere was refreshed by pure N_2 to keep the humidity low. Regular high-accuracy measurements demonstrated that graphene QHR standards allow for the realization of the ohm at a low magnetic field of $B = 4.5$ T, a high current of $I = 232.5$ μ A, and a temperature of $T = 4.2$ K simultaneously. To the best of our knowledge, this is the best performance of the graphene QHR standards achieved under concurrent (B , I , T) relaxed experimental conditions to date. Meanwhile, repeated high-accuracy measurements have demonstrated the robustness of the QHR standards over multiple cool-down cycles and their long-term stability over several years. In particular, we demonstrated that the quantized Hall resistance has remained stable within an accuracy of (2 ± 3) $n\Omega/\Omega$ over a period of 2.5 years to date. Furthermore, this accuracy has been maintained without any indication of degradation, even after undergoing long-distance transport between the Physikalisch-Technische Bundesanstalt (PTB) and the International Bureau of Weights and Measures (BIPM). The improved performances of our graphene QHR standards are expected to facilitate a broader dissemination of primary quantum standards beyond the NMIs, extending to calibration laboratories and industry on-site.

6.2 Homogeneity of electron density and robustness of graphene QHR standard

Device Fabrication. The details of graphene QHR devices presented in this chapter follow the instructions in Chapter 4. Monolayer epitaxial graphene was grown on semi-insulating 6H-SiC(0001) SiC substrates. The Hall bar structure had a total length of 1600 μm and a width of 400 μm . Figure 6.1(a-b) depicts the resulting chip with twelve Hall bars. The Hall bar devices were coated with a 5-layer F4-TCNQ doping stack. The volume ratio of F4-TCNQ/anisole to PMMA in the doping layer is 25%. The contact resistances were found to be less than 1 Ω ensuring reliable high-accuracy QHR measurements. The graphene QHR standards were stored at room temperature in a closed chamber filled with a mixture gas of N_2 and air, maintaining the humidity below 40%.

Heating under elevated temperatures. The devices were mounted in a top-loading He4 cryostat with a sliding seal. There is a homemade vacuum chamber connected to the dewar port. The vacuum chamber is used for the device treatments under different conditions. The cryostat with this homemade vacuum chamber has the following capabilities: (1) the chamber can be pumped down to below 1 mbar; (2) gases such as He, N_2 , and air can be backfilled into the chamber without contamination by other gases; and (3) the device stored in the chamber can be heated up to 150 $^\circ\text{C}$ and immediately exposed to helium atmosphere for transport measurement at $T = 4.2$ K. To investigate the effect of exposure gas and heating temperature on the electron density and mobility, the device G42 was exposed in pure N_2 (He or air) and heating at elevated temperatures.

High-accuracy measurement. The high-accuracy measurements were performed using a commercial He-4 bath cryostat with a magnetic field of up to 12 T, a temperature of 4.2 K, and currents from 10 μA to 1000 μA . The s parameter, the deviation and quantization regimes are discussed in this chapter. The definition of deviation and quantization regimes was discussed in detail in Section 3.5 previously. Figure 6.1(c) presents a typical quantum Hall measurement of a graphene QHR device with an electron density of $1.1 \times 10^{11} \text{ cm}^{-2}$ at 4.2 K. Due to the low electron density reduced by F4-TCNQ doping, the onset of the QH plateau ($\nu = 2$) was observed at a magnetic field as low as 2 T. The longitudinal resistance is symmetric with respect to the magnetic field directions, indicating a homogeneous carrier density distribution across the large area of the Hall bars ($L = 1600 \mu\text{m}$, $W = 400 \mu\text{m}$).

6.2 Homogeneity of electron density and robustness of graphene QHR standard

A systematic measurement of the electron density was conducted on the twelve nominally identical Hall bar devices, as described above in Figure 6.1 (a-b). The average electron density measured was calculated to be $n = (1.2 \pm 0.2) \times 10^{11} \text{ cm}^{-2}$, with a small variation among the twelve devices, as shown in the histogram in Figure 6.1(d). This implies a uniform carrier density over the entire graphene chip ($10 \times 5 \text{ mm}^2$), which is attributed to the high quality of the epitaxial graphene layer obtained from the PASG growth technique, and the reliable control of the carrier density through the F4-TCNQ molecular doping.

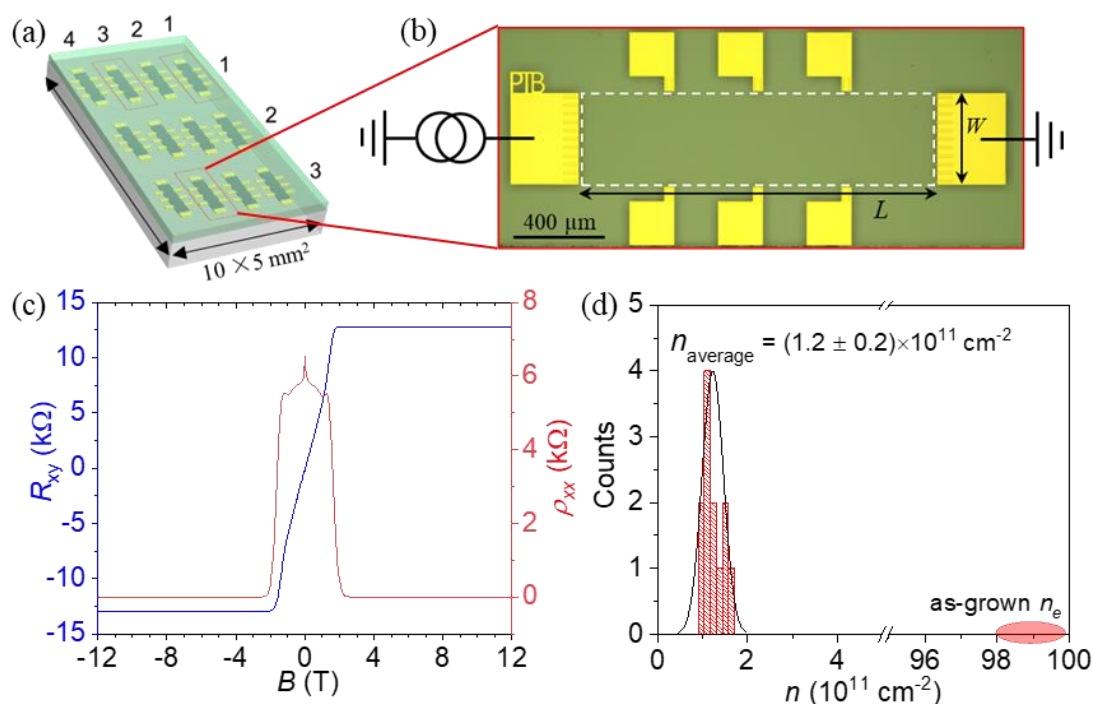


Figure 6.1 (a) Twelve graphene Hall bar devices with the index on SiC substrate ($5 \times 10 \text{ mm}^2$). (b) Optical microscopy image of a macroscopic Hall bar device with length $L = 1600 \text{ }\mu\text{m}$ and width $W = 400 \text{ }\mu\text{m}$. The white line indicates the area of monolayer epitaxial graphene. (c) Hall resistance R_{xy} and longitudinal resistivity ρ_{xx} as a function of magnetic field of an F4-TCNQ doped graphene QHR device with carrier density $1.1 \times 10^{11} \text{ cm}^{-2}$ at 4.2 K. (d) Statistical distribution of the carrier densities in the F4-TCNQ doped graphene Hall bars. The average carrier density of the twelve Hall bar devices is $(1.2 \pm 0.2) \times 10^{11} \text{ cm}^{-2}$.

To develop a practical graphene QHR standard, it is of the utmost importance that the carrier density remains stable over multiple cool-down cycles. The carrier density of an unprotected atomic-thin graphene is highly sensitive to its surrounding environment. Compared to other doping techniques such as corona discharge, ZEP-photochemical gating, and CrCO_3 functionalization that were used in the past [92,93,95], in this study several parallel experiments

were conducted to demonstrate the robustness and stability of our graphene QHR standards by molecular doping.

To assess the robustness of the carrier density stability against multiple cool-down cycles, a graphene QHR Device 42 was cooled down fifteen times successfully. Between the cooling cycles, Device 42 was annealed for different durations at different elevated temperatures up to 110 °C in gas atmospheres of air, helium, and nitrogen. Figure 6.2 summarizes the results of the cool-down cycles. The derived electron density (blue) and mobility (red) are plotted against the number of cool-down cycles. The annealing parameters prior to each cooling down are marked at the top of the figure. Throughout all cool-down cycles, the electron density of the device remained within a window of $\Delta n_{42} = 0.40 \times 10^{11} \text{ cm}^{-2}$. Meanwhile, the carrier mobility remained sufficiently stable.

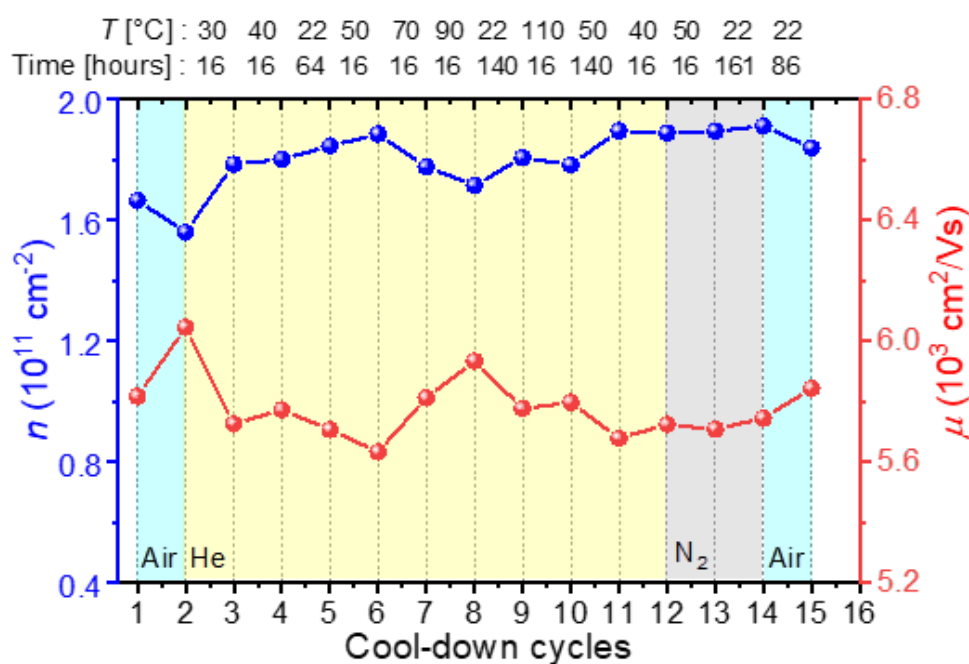


Figure 6.2 Variation of the electron density and mobility of device G42 at 4.2 K in fifteen cooling cycles. Between each magnetotransport measurement, the device was warmed up to room temperature and annealed for different durations at different elevated temperatures up to 110 °C in gas atmospheres of air (light blue), helium (yellow), and nitrogen (gray) between the cooling cycles. The annealing parameters prior to each cooling down are marked on top. The electron density of the device slightly varies around the average value of $1.8 \times 10^{11} \text{ cm}^{-2}$ within a window of $\Delta n_{42} = 0.40 \times 10^{11} \text{ cm}^{-2}$ throughout the entire treatment period.

In addition, other QHR devices from different graphene chips were fabricated with the same procedure. In total, twenty devices were conducted magnetotransport and high-accuracy measurements to test their robustness in multiple cooling cycles over a period of 2.5 years. All devices remained stable and robust, with no mechanical damage to the doping stack or significant changes in carrier density. These results demonstrate that the F4-TCNQ doped graphene QHR devices are highly reliable and robust in multiple cool-down cycles. Specifically, three devices designated G11, G31, and G33 (the numbers corresponding to the device index on the chip in Figure 6.1(a)) were continuously monitored, and the high-accuracy measurement results are presented below. These results demonstrate that the F4-TCNQ doped graphene QHR standards are highly reliable and robust devices in multiple cool-down cycles.

6.3 Long-term temporal stability of carrier density

Between cryogenic measurements, our graphene QHR devices were stored in a closed chamber with a mixture of N₂ and air at room temperature and ambient pressure. Typical results from device G11 are shown in Figure 6.3, including five measurements in a He-flow cryostat and four in a He-4 bath cryostat, each at 4.2 K over a period of more than 2.5 years. Figure 6.3(a) shows R_{xy} and R_{xx} measurements for each cool-down cycle. Very broad R_{xy} plateaus ($\nu = 2$) with an onset at 2.0 T to 2.5 T were observed for each measurement, accompanied by a decrease in the longitudinal resistance R_{xx} to zero. Figure 6.3(a) presents the symmetry of the longitudinal resistance with respect to the magnetic field direction, which is consistent with the result in Figure 6.1(c). This indicates that the electron density distribution in graphene remained homogeneous over the 2.5 years observation. These results demonstrate that the investigated graphene QHR devices are as reliable and stable as GaAs-based devices under the given storage conditions, making them a practical option for resistance metrology.

Table 6-1 and Figure 6.3(b) summarize the electron densities n and mobilities μ for each cool-down cycle. The electron density was observed to be stable, exhibiting only slight variations around a mean value, rather than exhibiting a clear drift in a particular direction. Indeed, the arbitrary shifts in the plateau onsets observed over the nine measurements suggest that the variation in carrier density does not continuously drift in a given direction. The density values vary by about $\pm 0.2 \times 10^{11} \text{ cm}^{-2}$ ($\pm 16\%$) around the average value of $n = 1.2 \times 10^{11} \text{ cm}^{-2}$. We presume that storing the device in a closed chamber with low humidity at room temperature helped to maintain a stable electron density within a window of $\Delta n = 0.4 \times 10^{11} \text{ cm}^{-2}$ over the

study period. The F4-TCNQ doped graphene QHR standard, subjected to the specified storage conditions, proved to be a reliable method to prevent significant drift of the electron density in either direction. This observation is consistent with the recent report on the stability of other epitaxial graphene devices. [49,52]

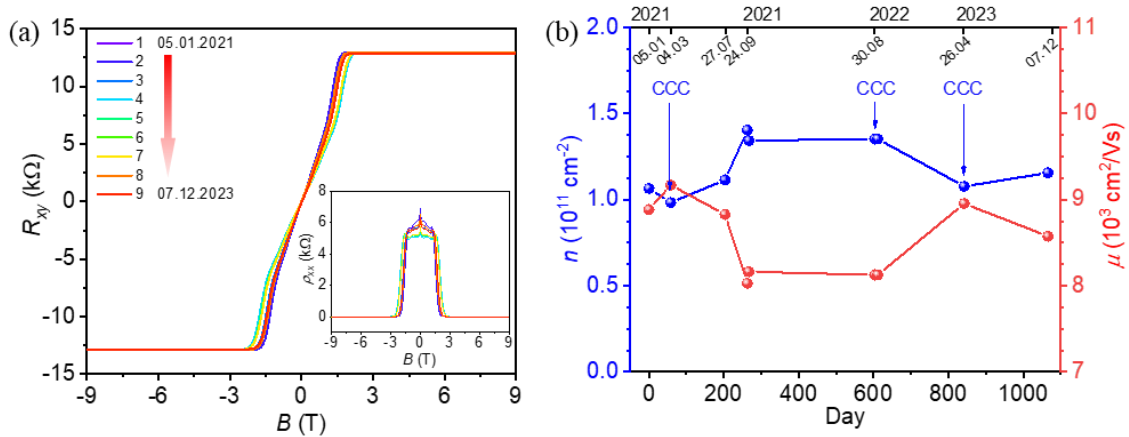


Figure 6.3 Repeated quantum Hall measurements of device G11 at 4.2 K over a period of more than 2.5 years. (a) The Hall resistance and longitudinal resistivity (insert) as a function of the magnetic field in nine times measurements. (b) Variation of carrier density and mobility as a function of time. The blue arrows indicate the dates of CCC-based high-accuracy measurements at a current of $38.7 \mu\text{A}$ and a temperature of 4.2 K. On August 30th, 2022, the device was subjected to current-dependent measurements at different currents: $38.7 \mu\text{A}$, $155.0 \mu\text{A}$, and $232.5 \mu\text{A}$.

Table 6-1. Electron density and mobility of device G11 over nine successive cool-down cycles over a period of two years. The average electron density is $(1.20 \pm 0.16) \times 10^{11} \text{ cm}^{-2}$. The electron density varies within a window of $\Delta n_{11} = 0.40 \times 10^{11} \text{ cm}^{-2}$ over the entire period.

Cool-down cycles	Date	Time [day]	n [cm^{-2}]	μ [$\text{cm}^2\text{V}^{-1}\text{s}^{-1}$]
1	05.01.2021	0	1.07×10^{11}	8884
2_CCC	04.03.2021	58	1.00×10^{11}	9167
3	27.07.2021	203	1.12×10^{11}	8829
4	24.09.2021	263	1.40×10^{11}	8029
5	28.09.2021	267	1.34×10^{11}	8164
6_CCC	30.08.2022	603	1.35×10^{11}	8127
7_CCC	07.09.2022	611	1.35×10^{11}	8127
8_CCC	26.04.2023	842	1.08×10^{11}	8954
9	07.12.2023	1066	1.16×10^{11}	8575
Average	--	--	1.20×10^{11}	8540

6.4 Long-term temporal stability of $n\Omega/\Omega$ -level quantization

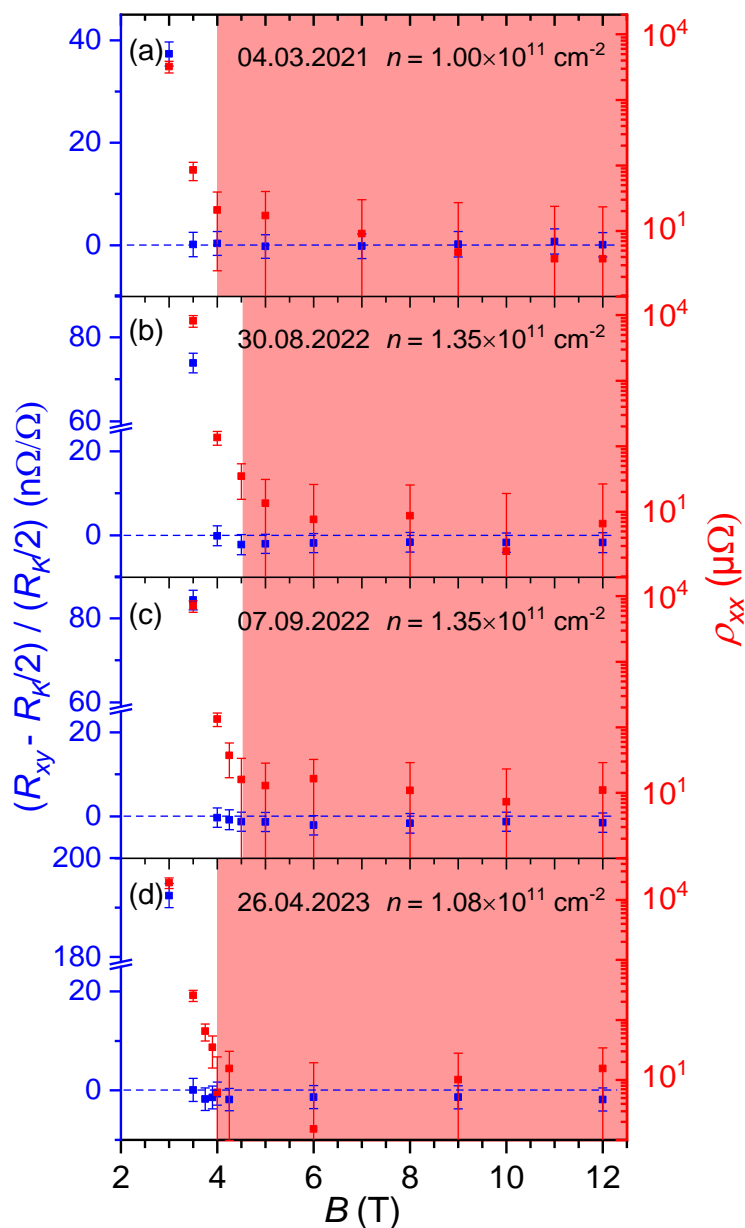


Figure 6.4 Dependence of the Hall resistance quantization on magnetic field for device G11 at $T = 4.2$ K and $I = 38.7 \mu\text{A}$. Device G11 was stored in an N_2 container at PTB for over two years. The relative deviation of R_{xy} from $R_K/2$ and the longitudinal resistivity ρ_{xx} as a function of magnetic field were investigated over the same time as the electron density, which experienced some variations with time: (a) $1.00 \times 10^{11} \text{ cm}^{-2}$, (b - c) $1.35 \times 10^{11} \text{ cm}^{-2}$ and (d) $1.08 \times 10^{11} \text{ cm}^{-2}$. The quantization of the Hall resistance achieved the $n\Omega/\Omega$ -level accuracy in the area highlighted in red (R_{xy} deviates from $R_K/2$ by less than $(2 \pm 3) n\Omega/\Omega$ ($k = 2$)). The measurements were carried out using a CCC resistance bridge.

To investigate the long-term stability of Hall resistance quantization with $n\Omega/\Omega$ -level accuracy, high-accuracy measurements of ρ_{xx} and R_{xy} were conducted on several graphene QHR devices. The results from Devices G11, G31, and G33 are presented below. Device G11 was stored and measured at PTB for over two years in order to investigate its stability at a fixed location. Devices G31 and G33 were transported from PTB to BIPM, where sequential high-accuracy measurements were carried out independently using different CCC bridges and GaAs reference QHR standards. Device G31 was packed in an N_2 container, while device G33 was packed in a plastic box- in the air - with inner and outer foam protection and shipped at ambient temperature. Both devices were transported between PTB and BIPM using a commercial express service.

As previously discussed in Section 3.5, the deviation regime was defined by a criterion of a low but non-zero longitudinal resistivity $\rho_{xx} \leq 100 \text{ m}\Omega$, and the quantization regime was defined by the criteria $|\rho_{xx}| = 0 \text{ }\mu\Omega$ within the uncertainty $\pm 23 \text{ }\mu\Omega$. The definition of the quantization regime presented here is relatively conservative. For a given QHR standard with a small s parameter, a small non-zero longitudinal resistance below a few hundred micro-ohms could still guarantee the relative deviation $(R_{xy} - R_K/2) / (R_K/2) \leq (2 \pm 3) \text{ n}\Omega/\Omega$ in metrology, which will be discussed below.

Table 6-2. Electron density and mobility of device G33 in four cool-down cycles. The carrier density was very stable even though the device was shipped from PTB to BIPM. The average of electron density is $(1.37 \pm 0.10) \times 10^{11} \text{ cm}^{-2}$. The electron density varies within a window of $\Delta n_{33} = 0.28 \times 10^{11} \text{ cm}^{-2}$ over the entire period.

Cool-down cycles	Date	Time [day]	n [cm^{-2}]	μ [$\text{cm}^2\text{V}^{-1}\text{s}^{-1}$]
1_PTB	18.01.2022	0	1.37×10^{11}	6292
2_PTB (CCC)	12.09.2022	238	1.50×10^{11}	6628
3_PTB (CCC)	25.04.2023	463	1.40×10^{11}	6757
4_BIPM (CCC)	14.09.2023	605	1.22×10^{11}	7180
Average	--	--	1.37×10^{11}	6714

Figure 6.4(a) presents the quantization regime of Device G11 in magnetic fields ranging from 4 T to 12 T. Within this range, the QHR is equal to $R_K/2$ with an accuracy of $(2 \pm 3) \text{ n}\Omega/\Omega$ ($k=2$), as measured through high-accuracy measurements. The maximum applied field of 12 T corresponds to the upper limit of the superconducting magnet. It is expected that the quantization regime would persist at higher magnetic fields since no breakdown of the Hall

resistance quantization was observed at 12 T. Moreover, in the repeatable measurements carried out to date, the quantization regime over a magnetic field from ≈ 4 T to 12 T (red background) has been maintained without any degradation over two years. This result demonstrates the excellent long-term stability of the graphene QHR standards for disseminating the SI unit ohm.

The $n\Omega/\Omega$ accuracy of QHR has been maintained not only over years in the laboratory but also after an international shipment between PTB and BIPM. Device G33 was stored at PTB over one year, and then delivered to BIPM. The carrier density and mobility were measured in both institutes as shown in Table 6-2. In the monitoring period of 463 days, the electron density of Device 33 is as stable as Device G11 at PTB, as previously discussed. After the shipment between PTB and BIPM, the carrier density only has a small decrease of $0.18 \times 10^{11} \text{ cm}^{-2}$. Considering the entire period of 605 days, the carrier density varied around the average value of $n = 1.37 \times 10^{11} \text{ cm}^{-2}$ within a window of $\Delta n_{33} = 0.28 \times 10^{11} \text{ cm}^{-2}$. The variations in electron densities of Devices G33 and G11 are comparable.

Figure 6.5 presents the accuracy of the quantized Hall resistance of Device G33. The QHR is equal to $R_K/2$ with an accuracy of $(2 \pm 3) n\Omega/\Omega$ ($k=2$) in magnetic fields from approximately 4 T to 12 T, even though experiencing a long-distance transport between PTB and BIPM. In the monitoring period of 605 days, the QHR accuracy of $(2 \pm 3) n\Omega/\Omega$ was maintained with no degradation. These results further demonstrate the long-term stability of the investigated graphene QHR standards regarding the time and long-distance shipment. Additional data on device G31 leading to similar conclusions is shown in the Appendix 1.

Another study of the stability of graphene QHR standards after long-distance shipping between metrology institutes was recently reported in the reference [50], in which the traveling devices were shipped in a specific chamber filled with argon. The onset of the quantization regime obviously shifted to a higher magnetic field after transport over a long distance [50], whereas this was not observed in our devices. This is attributed to the improved stability of the carrier density.

In this study, the investigated graphene QHR devices can easily achieve a $n\Omega/\Omega$ quantization level at a magnetic field as low as 4 T and over a wide field range of at least 8 T at 4.2 K. In contrast, a typical GaAs QHR device only exhibits this level of accuracy at the center of its Hall plateau, which is about 1 T wide around 10.8 T ($\nu = 2$) at 1.3 K. [84,138,168] The wider Hall resistance quantization in epitaxial graphene is due to magnetic field-dependent charge transfer between the interfacial layer and graphene. [48,111,135,169] Therefore, epitaxial graphene offers a distinctive advantage in resistance metrology due to its remarkably broad Hall plateau

at $\nu = 2$. This enables the realization of the SI unit ohm at a low magnetic field and high temperature (4.2 K).

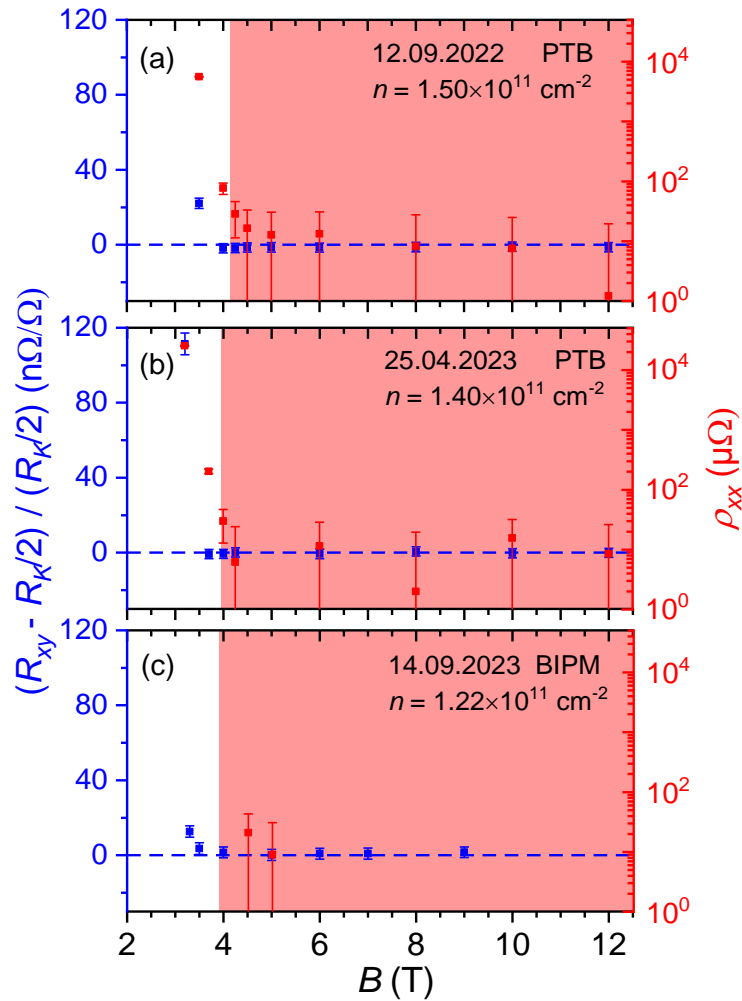


Figure 6.5 Dependence of the Hall resistance quantization on magnetic field for device G33 at $T = 4.2$ K and $I = 38.7$ μA at PTB and BIPM. Device G33 was stored in an N_2 container at PTB for seven months and then delivered to BIPM. The relative deviation of R_{xy} from $R_K/2$ and the longitudinal resistivity ρ_{xx} are plotted as functions of magnetic field. The electron densities determined by measurements at PTB are (a) 1.50×10^{11} cm^{-2} and (b) 1.40×10^{11} cm^{-2} , respectively, the corresponding value determined at BIPM is (c) 1.22×10^{11} cm^{-2} . The onset of the quantization regime (achieving $n\Omega/\Omega$ accuracy) was observed at about 4 T in all the measurements. Again, the quantization regime for the Hall resistance is indicated by the area highlighted in red.

The long-term temporal stability of quantization at the $n\Omega/\Omega$ level has been independently confirmed by two metrology institutes after long-distance transport. This further substantiates the viability of utilizing graphene QHR standards as traveling reference standards, akin to

GaAs-based QHR standards. These superior performances render graphene QHR standards viable replacement candidates for GaAs QHR standards, which are currently used in primary resistance metrology.

6.5 Realization of the SI ohm under relaxed conditions of B , I , and T simultaneously

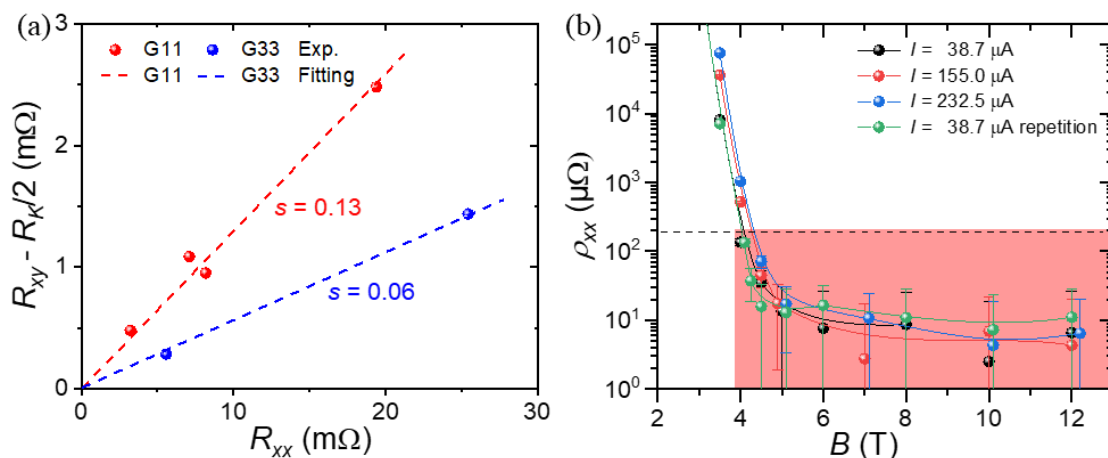


Figure 6.6 (a) Variation of $R_{xy}(B) - (R_K/2)$ as a function of the experimental longitudinal resistance $R_{xx}(B)$ for different B values for Devices G11 and G33. The s -parameter of 0.13 for Device G11 and 0.06 for Device G33 are extracted from the linear fit. (b) Dependence of the longitudinal resistivity ρ_{xx} on the magnetic field at the following currents $I = 38.7, 155.0, 232.5$, and again $38.7 \mu A$, for Device G11 at 4.2 K. The dashed line corresponds to $\rho_{xx} = 200 \mu\Omega$, below which the relative deviation of R_{xy} from $R_K/2$ remains less than $2 \text{ n}\Omega/\Omega$. The error bars represent to the combined expanded uncertainty ($k = 2$).

For magnetic field $B < 4.5 \text{ T}$, as shown in Figures 6.4 and 6.5, the measured relative deviation $(R_{xy} - R_K/2) / (R_K/2)$ remains below $(2 \pm 3) \text{ n}\Omega/\Omega$ ($k = 2$), while the longitudinal resistivity ρ_{xx} increases from zero to a few hundred $\mu\Omega$ as the magnetic field decreases. This indicates that the quantum Hall resistance retains its $\text{n}\Omega/\Omega$ accuracy, even though the longitudinal resistivity ρ_{xx} deviates slightly from zero. The small longitudinal resistivity ρ_{xx} observed in epitaxial graphene at 4.2 K is caused by variable range hopping transport. [111]

This small, but finite longitudinal resistance is accounted for by the s parameter. The s parameter, or coupling factor, is defined as $R_{xy}(B) - (R_K/2) = s \times R_{xx}(B)$. [46,84] This definition implies that the emerged non-zero R_{xx} is partially mixed into the quantum Hall resistance R_{xy} ,

thus inducing an error in the quantized Hall resistance R_{xy} and resulting in the relative deviation $(R_{xy} - R_K/2) / (R_K/2)$. [84,170] The s parameter quantifies the extent to which R_{xx} is mixed into the quantum Hall resistance R_{xy} for a given QHR device. The small s parameter of the graphene QHR devices in this study allows for the quantized R_{xy} (at $\nu = 2$) to maintain an accuracy of $(2 \pm 3) \text{ n}\Omega/\Omega$, even though ρ_{xx} increases to $200 \mu\Omega$. However, as the magnetic field decreases further and ρ_{xx} increases to a few thousand of $\mu\Omega$, the relative deviation $(R_{xy} - R_K/2) / (R_K/2)$ increases to several tens of $\text{n}\Omega/\Omega$.

Figure 6.6(a) shows the experimental variation of $R_{xy}(B) - (R_K/2)$ as a function of $R_{xx}(B)$ for magnetic fields below 4.5 T at a given temperature (4.2 K) and current ($38.7 \mu\text{A}$). This variation is consistent with the expected linear dependence of the slope s , as evidenced by the linear fitting superimposed on the experimental data. For Device G11, the coupling factor derived from the linear fit is equal to $s = 0.13$. For this value, an upper limit of $\rho_{xx} \leq 200 \mu\Omega$ ensure that the relative deviation of the quantized Hall resistance remained within $(2 \pm 3) \text{ n}\Omega/\Omega$, which is validated by the measurement of the relative deviation of $R_{xy}(B)$ from $R_K/2$ in the experiment as shown in Figures 6.4 and 6.5 Device G33 has an even smaller coupling factor of 0.06, as determined from the linear fit.

Figure 6.6(b) shows the longitudinal resistivity of the device G11 as a function of the magnetic field measured for the following currents: $I = 38.7 \mu\text{A}$, $155.0 \mu\text{A}$, $232.5 \mu\text{A}$, and again $38.7 \mu\text{A}$. The longitudinal resistivity remains well below $200 \mu\Omega$ - indicating that the device remains in agreement with $R_K/2$ with an accuracy of $(R_{xy} - R_K/2) / (R_K/2) \leq (2 \pm 3) \text{ n}\Omega/\Omega$ - over a wide magnetic field range from $B = 4.5$ to 12 T, up to the maximum current of $232.5 \mu\text{A}$. Note that the current value of $232.5 \mu\text{A}$ is the maximum current that our CCC current source can provide. The breakdown current at 4.2 K, which results in a significant deviation of R_{xy} from $R_K/2$, is expected to be even higher than this value.

At the lower limit of the quantization regime ($B \leq 4.5 \text{ T}$, $I = 38.7 \mu\text{A}$), the longitudinal resistivity increases with current, due to a small self-heating effect at high currents. Upon resetting the current to its initial value of $38.7 \mu\text{A}$, the longitudinal resistivity returned to its initial values within the uncertainty, regardless of the magnetic field. The reversibility of ρ_{xx} indicates that the graphene QHR device quantization is robust against currents up to $232.5 \mu\text{A}$.

As previously stated, since the three experimental conditions (B , I , T) are mutually constrained in the physics of the QHE, it is challenging to operate QHR standards under the relaxed experimental conditions in terms of B , I , and T simultaneously. To achieve $\text{n}\Omega/\Omega$ accuracy of R_{xy} , the GaAs QHR standard typically requires a magnetic field of $B \approx 10 \text{ T}$, a temperature of T

≈ 1.3 K, and a measurement current of I not exceeding $50 \mu\text{A}$. [41] The previous results presented graphene QHR standards that were operating in a single relaxed condition, while the rest of the other two were not. [8] [47–53] The investigated graphene QHR standard was demonstrated to realize the SI ohm with an accuracy of $(2 \pm 3) \text{ n}\Omega/\Omega$ under the relaxed conditions of $B = 4.5$ T, $I = 232.5 \mu\text{A}$, and $T = 4.2$ K simultaneously. To the best of our knowledge, the fabricated graphene QHR devices described in this study present the best performance yet reported considering concurrent relaxed conditions, $B = 4.5$ T, $I = 232.5 \mu\text{A}$, and $T = 4.2$ K. These performances far exceed the operational conditions of the GaAs QHR standards by a factor of three to ten.

Practically, operating the QHR standard at such high currents can improve and simplify resistance measurement by allowing for a higher signal-to-noise ratio. Furthermore, operating at such low magnetic fields only requires a simplified superconducting magnet, which can be easily integrated into a table-top cryo-cooler system. [171] The $\text{n}\Omega/\Omega$ accurate QHR achieved at low magnetic field (≤ 6 T), high current, and high temperature (4.2 K) provide further confidence to realize graphene QHR standards integrated into a compact, cryogen-free, table-top setup for industrial applications and on-site calibrations.

6.6 Limits of quantization as a function of electron density

For the investigated QHR devices, it was observed that the onsets of the deviation and quantization regimes are reversible as the variation in electron density. Specifically, as the electron density increases (or decreases), the onset of the quantization regime shifts to a higher (or lower) magnetic field. For instance, the results of Device G11 are shown in Figure 6.4. The onset of the quantization regime shifts from 3 T to 4 T as the electron density increases from $1.00 \times 10^{11} \text{ cm}^{-2}$ to $1.35 \times 10^{11} \text{ cm}^{-2}$. In Figure 6.4(d), the onset of the quantization regime shifts back to 3.5 T as the electron density decreases to $1.08 \times 10^{11} \text{ cm}^{-2}$. Similar behavior is observed from Device G33 in Figure 6.5 and Device G31 in Figure A2.

Indeed, previous studies have already shown that the dependence of the quantization regime onset on the carrier density in epitaxial graphene QHR devices [51]. In Ref. [51] the deviation regime was defined by a longitudinal resistivity $0 < \rho_{xx} \leq 100 \text{ m}\Omega$ and the quantization regime by $\rho_{xx} = 0$ within the uncertainty for a current of $38.7 \mu\text{A}$ and a temperature of 4.2 K. Figure 6.7 presents the onsets of the deviation (light blue) and quantization (bright blue) regimes in the magnetic fields as a function of electron density. Each bright (light) blue data point corresponds

to a high-accuracy (magnetotransport) measurement from Devices G11, G31, and G33. These results are in accordance with the contour plot (red and dark points) presented in Ref. [51].

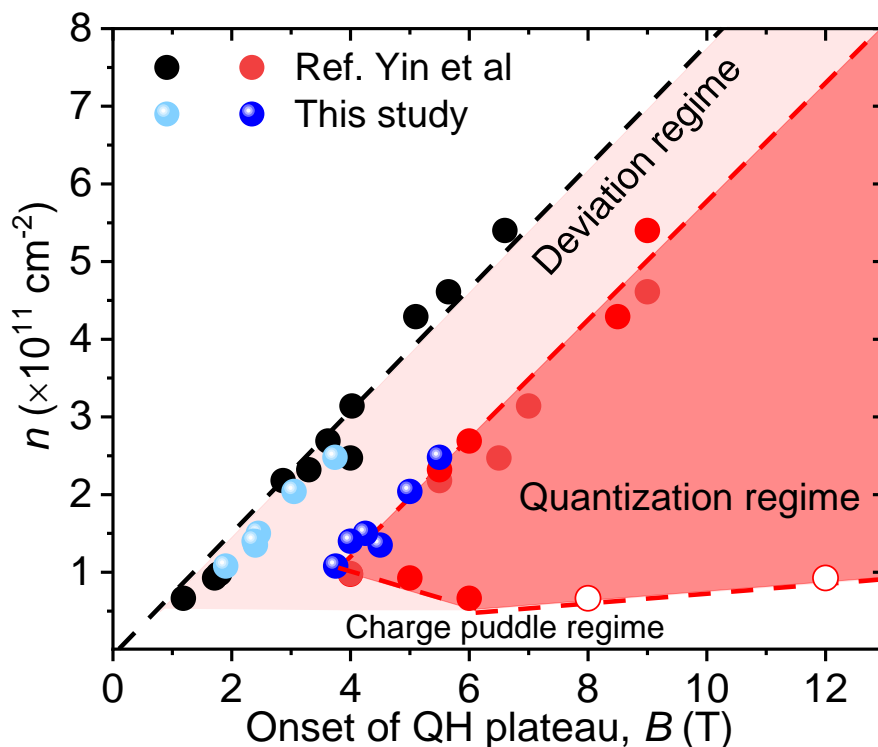


Figure 6.7 Deviation and quantization regimes as a function of the electron density (at zero field) in epitaxial graphene QHR standards. The red and black data points are the results in the reference [51]. The light and bright blue points are the measurement data from the devices in Chapter 6. Each data point corresponds to an individual measurement. The onset of the deviation regime is extracted from the QHE measurement, and the onset of the quantization regime is extracted from the high-accuracy measurement. The experimental data of this study are in agreement with the contour plot drawn from the reference. [51]

In the region of carrier densities $n \geq 1.00 \times 10^{11} \text{ cm}^{-2}$, the onset of the quantization regime is linearly dependent on the electron density with a coefficient of $0.75 \times 10^{11} \text{ cm}^{-2}/\text{T}$. As the electron density increases by $0.75 \times 10^{11} \text{ cm}^{-2}$, the onset of the quantization regime increases by 1 T. Furthermore, the contour plot in Figure 6.7 presents the width of the deviation regime as approximately 2 T in the region of electron densities $n \geq 1.00 \times 10^{11} \text{ cm}^{-2}$. The contour plot is a 2D map of the deviation and quantization regimes for the epitaxial graphene QHR standards. According to the electron density in epitaxial graphene, the deviation and quantization regimes in magnetic field regions can be predicted. For instance, it is necessary to control the carrier density below $2.5 \times 10^{11} \text{ cm}^{-2}$, if an epitaxial graphene QHR standard was operated in a table-

top cryogen-free setup with a simplified superconducting magnet below 6 T. The contour plot can serve as a benchmark for the epitaxial graphene QHR standards, allowing users to evaluate the quality of a new QHR device.

6.7 Current-dependent measurement by the current reversal technique

To investigate the breakdown current and the onset/end of the Hall plateau in QHR device, we performed the current-dependent measurement in another Device G1594-D6_3(chip1)2 HFML at a high magnetic field up to 35 T. The onset of longitudinal resistance $\rho_{xx} \sim 0$ is the boundary between the classical and quantum Hall states. The method of current reversal measurement can measure the longitudinal resistance within the uncertainty below 2 m Ω .

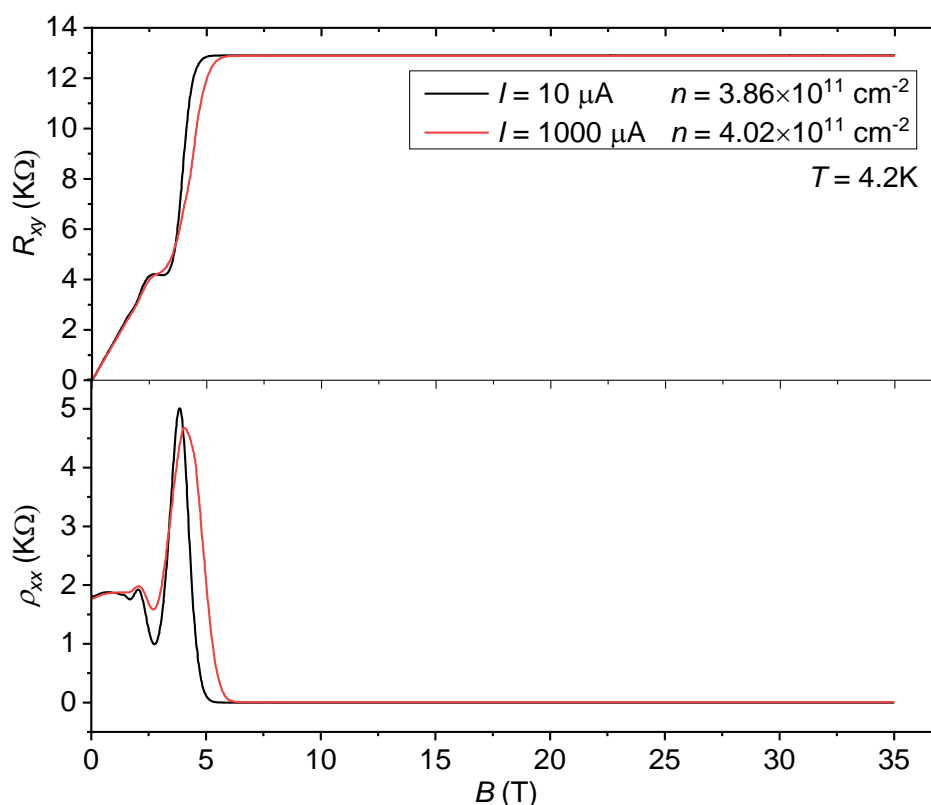


Figure 6.8 The quantum Hall effect measurement with the applied current of 10 μA (black) and 1000 μA (red) in the Hall channel in a high magnetic field up to 35 T.

The quantum Hall effect measurement with the applied current of 10 μA (black) and 1000 μA (red) in magnetic field up to 35 T is presented in Figure 6.8. Even though 1000 μA current is applied, the very wide Hall plateau and zero longitudinal resistance are observed in the magnetic field range over 18 T. A strong breakdown effect was not observed in such a high

current, except that the onset of Hall plateau and zero longitudinal resistance slightly shifted to higher magnetic fields.

The onset of zero longitudinal resistivity at currents of 50 μA , 300 μA , and 1000 μA using the current reversal measurement is shown in Figure 6.9(a). The uncertainty is higher for low current because the signal-to-noise is less for lower current.

The onset of zero longitudinal resistance slowly shifts to 8.5 T as the current increases to 1000 μA . However, in such a high current, zero longitudinal resistance is maintained in magnetic fields from 8.5 T up to 35 T without dissipation transport. Considering the width of the Hall bar is 400 μm , the graphene QHR can sustain the current density as high as 2.5 A/m and preserve the Hall plateau at filling factor 2 in magnetic fields from 8.5 T to 35 T at 4.2 K. The sustainable current density in our device is one order of magnitude higher than the result in the literature [111].

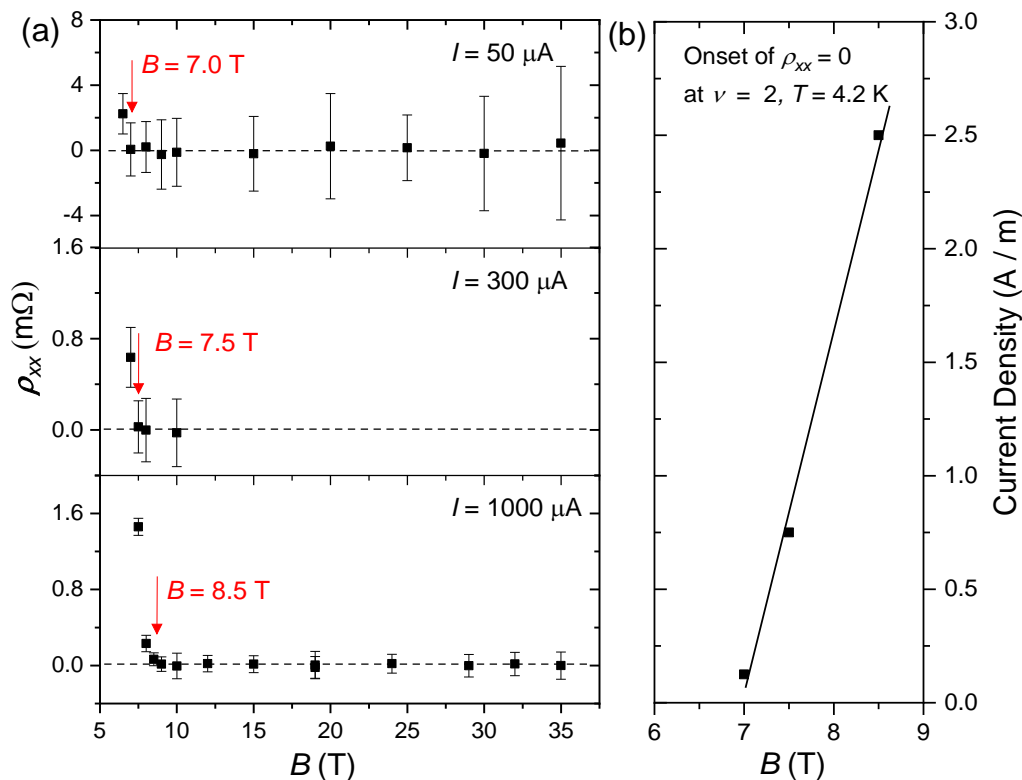


Figure 6.9 (a) The onset of zero longitudinal resistivity at currents of 50 μA , 300 μA , and 1000 μA using the current reversal measurement. The onset of zero longitudinal resistivity slowly shifts to 8.5 T as the current increases to 1000 μA . Zero longitudinal resistivity is maintained from 8.5 T up to 35 T without dissipation transport. (b) Current density in the Hall channel as a function of the magnetic field for the onset of zero longitudinal resistivity.

The onsets of zero longitudinal resistance in different current densities as a function of the magnetic field were plotted in Figure 6.9 (b). The linear fitting implies the boundary of the Hall plateau at filling factor 2 is linearly dependent on the current density. It was estimated that the current density increased by 1.58 A/m, and the onset of zero longitudinal resistance in magnetic fields shifted 1 T.

6.8 Conclusion

Our findings demonstrate that the investigated graphene QHR devices enable the use of resistance standards to facilitate the realization of the SI ohm under relaxed experimental conditions due to their long-term stability and robustness. The performance of the graphene QHR standard is robust and reproducible over multiple cool-down cycles. When stored in a mixture of N₂ and air with low humidity at room temperature, our graphene QHR standards exhibit Hall resistance quantization with an accuracy of $(2 \pm 3) \text{ n}\Omega/\Omega$ over a wide magnetic field range from 4 T to 12 T at 4.2 K. This $\text{n}\Omega/\Omega$ -level accuracy in the wide magnetic field range has been maintained for more than two years to date, even after a long-distance transport between PTB and BIPM where it was independently measured. Furthermore, the graphene QHR showed agreement with $R_K/2$ under the simultaneously relaxed conditions $B = 4.5 \text{ T}$, $I = 232.5 \text{ }\mu\text{A}$, and $T = 4.2 \text{ K}$, thereby substantiating their advanced performance. To the best of our knowledge, this is the most advanced performance ever achieved by graphene QHR standards for resistance metrology to date. The graphene QHR standards, representing a new generation of QHR standards capable of operating under relaxed conditions, are ideally suited for integration into a table-top cryocooler system. Such a compact QHR system is not only capable of replacing conventional GaAs-based standards for the practical realization of the SI unit ohm in NMIs but also provides on-site access to commercial calibration laboratories and industry.

Chapter 7. Summary and outlook

7.1 Summary

One of the goals of electrical quantum metrology is to provide resistance standards at the fingertips of the end-users. Simplifying the operation conditions of QHR standards can shorten the calibration chain from primary resistance standards to the final product, resulting in higher accuracy for end users in science, technology, and industry. Developing a new generation of QHR standards that can operate at relaxed conditions of B , I , and T is the cornerstone of the electrical quantum standards.

This thesis showed that epitaxial graphene is a promising alternative material to GaAs heterostructures for developing advanced QHR standards. Four core questions must be addressed when developing epitaxial graphene QHR standards for practical resistance metrology. (1) How to grow a high-quality, large-scale, homogeneous monolayer epitaxial graphene sheet on a semi-insulating substrate. (2) How to develop a technique for the graphene QHR device fabrication, which is cost-effective, efficient, and compatible with semiconductor techniques. (3) How to control the extremely high electron density of as-grown epitaxial graphene to the desired value for the QHR standards. (4) How to make sure the graphene QHR standards can achieve an accuracy of $n\Omega/\Omega$ (10^{-9}) at low magnetic fields $B < 6$ T, high currents $I > 100$ μ A, and high temperatures $T > 4.2$ K, and to maintain it over years or decades. Previous studies have demonstrated that high-quality, large-scale, and metrology-grade monolayer graphene can be grown on semi-insulating SiC substrates by epitaxial growth at high temperatures, which is the footstone for developing graphene QHR devices. This thesis has addressed the remaining three core questions.

Technique for graphene QHR device fabrication

A simple, efficient, and cost-effective fabrication process was developed to fabricate scalable, multiple, and integrated graphene QHR devices on a piece of graphene chip. The device fabrication is based on optical lithography, rather than the more expensive electron beam lithography that is commonly used by other groups in the fabrication of graphene QHR standards. For further technology transfer for commercial QHR devices, this fabrication process is compatible with the semiconductor technology.

Control the electron density of epitaxial graphene for QHR standards

A molecular doping technique based on F4-TCNQ molecules was developed to control the carrier density of as-grown epitaxial graphene. The magnetotransport measurement results demonstrated that the molecular doping technique successfully reduced the intrinsic carrier density of epitaxial graphene. By precisely adjusting F4-TCNQ concentration in PMMA, the carrier densities were controlled to the desired values in a wide range from *n*-type to *p*-type graphene. The lowest controllable electron (hole) density obtained is $6.7 \times 10^9 \text{ cm}^{-2}$ ($6.0 \times 10^9 \text{ cm}^{-2}$) in *n*-type (*p*-type) epitaxial graphene. The observation of asymmetric mobility behavior as a function of carrier density for electron and hole indicated distinct scattering strengths of charge carriers in *n*- and *p*-type epitaxial graphene. A doping model based on the experiment and DFT simulation was established to explain the electron transfer between the F4-TCNQ and epitaxial graphene/SiC surface in the molecular doping process. The F4-TCNQ doping technique is thus a stable and permanent method for tailoring the carrier density in epitaxial graphene.

The graphene QHR standards with accuracy of $n\Omega/\Omega$ (10^{-9})

The superior performance of the *n*- and *p*-type graphene QHR standards was characterized by high-accuracy measurements using a CCC bridge in magnetic fields up to 12 T at 4.2 K. The high-accuracy measurements identify the deviation ($0 < \rho_{xx} \leq 100 \text{ m}\Omega$) and quantization ($\rho_{xx} = 0$ within the error bar) regimes in the broad Hall plateau of epitaxial graphene, which was not described in the literature yet. An extensive investigation from both *n*- and *p*-type devices has observed that the onset of the deviation regime was 2 T lower than the onset of the quantization regime. In the deviation regime, the QHR deviated from the nominal value $R_K/2$. In the quantization regime, the QHR was in agreement with the nominal value $R_K/2$ within the accuracy of $(1 \pm 3) \text{ n}\Omega/\Omega$. Thus, the investigated graphene QHR standards guarantee a metrology-grade accuracy of $n\Omega/\Omega$ for primary resistance standards.

The *n*-type QHR standards exhibited the quantized resistance with an accuracy of $(1 \pm 3) \text{ n}\Omega/\Omega$ (10^{-9}) in magnetic fields from 3.5 T up to 12 T at 4.2 K. This demonstrated the high quality and performance of our graphene QHR devices. The *n*-type graphene QHR standards with 5-, 3-, and 2-layers of doping stacks achieved an accuracy of $(1 \pm 3) \text{ n}\Omega/\Omega$ at 4.2 K in high-accuracy measurements. There is no preference for any of the three investigated layer sequences as long as the required carrier density is obtained. Moreover, a systematic investigation of the *n*-type graphene QHR standards with different carrier densities was conducted by the high-accuracy measurements at 4.2 K. By controlling the carrier densities of *n*-type graphene QHR devices,

the onset of the quantization regime was measured as a function of carrier density. Furthermore, a 2D contour plot of the quantization regime as a function of electron density and magnetic field in *n*-type QHR devices revealed the correlation between the quantization regime and the electron density and the magnetic field. This represents the first detailed study of the electron density-dependent quantization regime of epitaxial graphene.

The *p*-type QHR standards also exhibited the quantized resistance with an accuracy of $(1 \pm 3) \text{ n}\Omega/\Omega$ (10^{-9}) at the lowest magnetic field of 3.5 T at 4.2 K. A contour plot of the quantization regime in *p*-type QHR devices was derived for comparison with that of *n*-type devices. The correlation between the quantization regime and the electron densities was also observed in *p*-type QHR standards. The magnetotransport measurements observed the hole mobility is smaller than the electron mobility at the same carrier density. In the high-accuracy measurements, the onsets of deviation and quantization regimes of the *p*-type QHR devices were observed at higher magnetic fields than that of the *n*-type QHR devices. Thus, the 2D contour plot of *n*- and *p*-type QHR devices was formed to be asymmetric with respect to the carrier density. These results are attributed to the stronger scattering in *p*-type epitaxial graphene.

Currently, no comprehensive theory or model describes the correlation between the quantization regime and the electron density in *n*- and *p*-type epitaxial graphene. According to the systematic experimental results, the 2D contour plot serves as a two-dimensional map that guides the deviation and quantization regime in a magnetic field. Thus, the contour plot is a benchmark for the community to evaluate the quantization regime of an epitaxial graphene QHR standard with a specific electron density. This provides a highly practical benefit for the application of graphene QHR standards in quantum resistance metrology.

Stable accuracy of quantized Hall resistance over the years

The graphene QHR standards in this thesis facilitated the long-term stable and robust realization of the SI ohm under relaxed experimental conditions. The performance of the graphene QHR standard was shown to be robust, reproducible, and reliable over multiple cool-down cycles. When stored in a mixture of N₂ and air with low humidity at room temperature, our graphene QHR standards exhibit Hall resistance quantization with an accuracy of $(2 \pm 3) \text{ n}\Omega/\Omega$ over a wide magnetic field range from 4 T to 12 T at 4.2 K. This $\text{n}\Omega/\Omega$ -level quantization in the wide magnetic field has been maintained for more than two years to date, even after a long-distance transport between PTB and BIPM where it was independently measured. Furthermore, the graphene QHR standards achieved an accuracy of $\text{n}\Omega/\Omega$ in realizing the SI ohm under the

simultaneously relaxed conditions $B = 4.5$ T, $I = 232.5$ μA , and $T = 4.2$ K, underlying their advanced performance. To the best of our knowledge, this is the most advanced performance ever achieved by graphene QHR standards for resistance metrology to date. The graphene QHR standards, representing a new generation of QHR standards capable of operating under relaxed conditions, are ideally suited for integration into a table-top cryocooler system. Such a compact QHR system should not only be capable of replacing conventional GaAs QHR standards for the practical realization of the SI ohm in NMIs but also could be readily accessible to commercial calibration laboratories and industry for on-site primary resistance calibration.

7.2 Outlook

Reviewing the history of graphene QHR standards, two landmarks have been achieved in the history of graphene QHR standards. In the years 2010 to 2012, it was demonstrated that the $\text{n}\Omega/\Omega$ -level accuracy of the quantum Hall resistance can be achieved in epitaxial [8] and exfoliated [140] graphene QHR standards. However, the $\text{n}\Omega/\Omega$ -level accuracy of the quantum Hall resistance was only achieved at high magnetic fields ($B > 10$ T) and mK temperatures due to the low quality of graphene. The second landmark was in the years from 2019 to 2024. The graphene QHR standards are now capable of achieving the $\text{n}\Omega/\Omega$ -level accuracy at $B < 6$ T and $T = 4.2$ K. The next landmark would be developing the graphene QHR standard at $T \geq 4.2$ K and $B < 3$ T, which is the magnetic field of the permanent magnet can reach. Here, two ideas are discussed to achieve this goal.

1. Monolayer epitaxial graphene QHR standard worked in permanent magnet ($B < 3$ T)

In the past, the epitaxial graphene QHR standards should be operated in high magnetic fields ($B > 6$ T) at liquid temperature (4.2 K), not to speak of the conventional GaAs QHR standards. In this case, expensive superconducting magnets are required to be immersed in liquid helium to generate high magnetic fields. Only advanced laboratories in universities and metrology institutes can operate the QHR standards in experiments. Another important barrier is the expertise needed to run the system. In this thesis, the epitaxial graphene QHR standards achieved the $\text{n}\Omega/\Omega$ -level accuracy of the quantum Hall resistance at a magnetic field of 4.0 T at liquid helium temperature (4.2 K). This performance allows for the graphene QHR standards to operate in a cryogen-free, table-top system for resistance calibration. In this compact system, the heavy superconducting magnet is replaced by a very small superconducting magnet that is 7.5 cm tall with an outer diameter of 6 cm [171], which can reach magnetic fields up to 6 T.

We can thus observe a big progress of the graphene QHR standard. However, this is not the end of the graphene QHR standards. There is still potential to improve the performance of graphene QHR standards and simplify the resistance calibration system. One of the goals of modern-day metrology is to provide quantum standards at the fingertips of the end-users.

Nowadays, permanent magnets can reach 3 T at room temperature. [172–174] Hence, the next landmark is to develop a QHR standard that can operate in such a permanent magnet. According to the prediction in the contour plot in Figure 6.7, to operate the epitaxial graphene QHR in magnetic fields below 3.0 T, the electron density would be reduced to $5 \times 10^{10} \text{ cm}^{-2}$. However, for the epitaxial graphene on a 6H-SiC substrate with electron density $\leq 5 \times 10^{10} \text{ cm}^{-2}$, the $n\Omega/\Omega$ -level accuracy of quantized resistance deviates from the theory value $R_K/2$. This is due to the disorder in epitaxial graphene, resulting in the broadening of the Landau level. The energy strength of disorder in epitaxial graphene with low electron density is estimated at about 12 meV in experiments [130], which is comparable with Fermi energy $E_F \approx 26 \text{ meV}$ ($n_e = 5 \times 10^{10} \text{ cm}^{-2}$). The disorder in epitaxial graphene originates from the variation of electron density on different types of terraces, the charge puddles, and charge impurities.

It has been reported that the SiC stacking order can induce doping variation in different terraces in epitaxial graphene on 6H-SiC substrate. [175] Epitaxial graphene exhibits periodic ≈ 0.25 and ≈ 0.50 nm step heights on 6H-SiC substrate, as shown in Figure 3.4. The periodic sequence of the non-identical SiC terraces leads to the termination-dependent polarization doping, resulting in the variation of doping levels and electron densities on different types of terraces. Therefore, the carrier density periodically varies on the non-identical terraces in epitaxial graphene on 6H-SiC substrate. The inhomogeneous polarization doping and electron densities are the disorders in epitaxial graphene that result in the broadening of Landau levels.

The epitaxial graphene grown on 4H-SiC substrates has an identical polarization doping since the equivalent terrace terminations on the overlying graphene layer. There is no variation of electron density in graphene on 4H-SiC substrate, which would have less disorder compared with the graphene on 6H-SiC. The graphene on 4H-SiC substrate for QHR standards would achieve the $n\Omega/\Omega$ -level accuracy of quantized Hall resistance in a magnetic field below 3 T. The epitaxial graphene on 4H-SiC is thus a promising candidate for developing QHR standards operating at permanent magnets at $T \geq 4.2 \text{ K}$.

2. Graphene on hBN for QHR standards

As shown in Figure 5.10, the quantization regime of *n*- and *p*-type epitaxial graphene on SiC is limited at a magnetic field ≈ 4.0 T. As the magnetic field decreases further, the $n\Omega/\Omega$ -level accuracy of the quantized Hall resistance is destroyed due to the inevitable disorder in the epitaxial/SiC hybrid system. To achieve a highly accurate quantized Hall resistance in a lower magnetic field, it requires to reduce the energy strength of the disorder as low as possible. Epitaxial graphene on hBN could be an ideal hybrid system.

It is well-known that exfoliated graphene on hBN results in very high mobility and very low disorder due to the hBN strongly screening the charged impurities in the substrate. There are two options to obtain the epitaxial graphene/hBN hybrid system for the QHR standards. (1) Transfer of large-scale monolayer epitaxial graphene to the hBN substrates to fabricate graphene QHR standards. Such exfoliated graphene is widely used to transfer to hBN substrates. However, the size of exfoliated graphene is limited in micro-meter flakes with arbitrary shapes by the transfer process. Due to the original milli-meter size of epitaxial graphene (10×5 mm²), it should be possible to obtain large-scale epitaxial graphene on hBN substrate by a transfer process. (2) Growth of graphene on hBN substrates directly. It has been reported that the graphene was grown on hBN by CVD growth. [176] The large-scale graphene on hBN grown by CVD could become a promising platform for accurate QHR standards in the future.

3. Graphene QHR standards at high temperatures, $T > 77$ K

In the future, one could explore the QHR standards based on new materials, which can work at magnetic fields below 3.5 T and temperatures above 77 K, the liquid N₂ temperature. Liquid N₂ is much cheaper and much easier to access than liquid He. To obtain such QHR standards operating above 77 K at magnetic fields below 3.5 T, quasi-free-standing monolayer graphene or graphene on hBN substrates could be explored.

For the monolayer epitaxial graphene, the accuracy of quantized Hall resistance above 25 K degrades due to the remote interfacial phonons scattering in QH transport. The remote interfacial phonons originate from the oscillation between the graphene and buffer layer. There is no buffer layer between graphene and SiC layers in quasi-free-standing monolayer graphene. Therefore, remote interfacial phonons do not exist. The main challenge in quasi-free-standing monolayer graphene is the high hole density ($\sim 5 \times 10^{12}$ cm⁻²). [177] Prior to the development of QHR standards, it is necessary to find a suitable strong donor molecular to reduce the hole density to 10^{11} cm⁻². The quasi-free-standing monolayer graphene with hole density on this

level could be a candidate to observe the highly accurate quantized Hall resistance at high temperatures.

4. Universality of R_K with comparison graphene QHE against topological insulator QAHE

The QHE is a fascinating macroscopic quantum effect occurring in two-dimensional (2D) conductors that has become one of the cornerstones of the worldwide reference system for scientific and industrial measurements. [84] In theory, the quantum Hall resistance is considered to be a topological invariant, not altered by electron-electron interaction, spin-orbit coupling, or hyperfine interaction with nuclei, and insensitive to the much more subtle influences of gravity. [178] In 2009, a theory work predicted a quantum electrodynamical correction to the von Klitzing constant of the order of 10^{-20} for practical magnetic field values. [179] The hypothesis of resistance quantization units of h/ve^2 and its invariance in terms of material, electronic property, and different types of quantum Hall effect (integer quantum Hall effect and quantum anomalous Hall effect) must be tested experimentally. Because of the fundamental nature of the Hall resistance quantization, experimental tests of its universality are of the utmost importance, especially for improving our knowledge of two fundamental quantities of nature: the electron charge and Planck's constant.

The universality of integer quantum Hall effect in epitaxial graphene with that in GaAs/AlGaAs heterostructures has been demonstrated with the relative standard uncertainty of 8.6×10^{-11} . [45,139] This is the most stringent test of the universality of the QHE in terms of material independence. However, the uncertainty of the resistance quantization observed in the experiment (10^{-11}) is nine orders of magnitude higher than that predicted in theory (10^{-20}). Moreover, the accurate comparison of resistance quantization in epitaxial graphene and GaAs/AlGaAs heterostructures is based on the same type of quantum Hall state, the integer QHE. It is worth implementing an accurate comparison measurement that can further prove the universality of R_K with higher accuracy over 10^{-11} and the universality of R_K in terms of different types of quantum hall states and materials simultaneously.

At PTB, excellent graphene QHR devices are available, which showed 10^{-9} accuracy of $R_K/2$ based on the integer QHE. Colleagues from PTB also demonstrated that the excellent topological insulator BiSbTe device from Würzburg can achieve 10^{-9} accuracy of R_K based on QAHE. [180]

By connecting a topological insulator device to one side of the CCC bridge, and two graphene devices in series to the other side of the CCC bridge, one could directly compare the universality of R_K in terms of graphene and topological insulator BiSbTe. In this measurement, it should be possible to achieve accuracy of R_K on the level of 10^{-11} or lower. Further, this experiment will demonstrate how accurate the universality of R_K can reach and where the limit of the quantum frontier of R_K is.

The graphene QHR standard is based on the integer QHE, while the topological insulator BiSbTe is based on QAHE. Such experiment could further prove the universality of R_K over two independent materials (devices) and two independent Hall effects (QAHE and QHE) with sharing impact both on metrology and fundamental research. This would be a milestone in the field of quantum Hall effect and resistance metrology.

Appendix

A.1 Stability of quantization after long-distance transport: Device G31

The device G31 was shipped from PTB to BIPM and finally returned to PTB. During the shipment, the device was packed in a glass bottle filled with N₂. Magnetotransport and high-accuracy measurements of the device G31 were performed in both institutes over a period of about two years. Broad R_{xy} plateaus ($\nu = 2$) in magnetic fields above 4 T are observed in each measurement, accompanied by a vanishing longitudinal resistance.

Table A1.1 and Figure A1.1 present the variation of electron density and mobility in seven successive cool-down cycles measured at PTB and BIPM. At BIPM, the device was stored in air with high humidity (80%) between the two cool-down cycles. The electron density was observed reduced from $2.31 \times 10^{11} \text{ cm}^{-2}$ to $1.09 \times 10^{11} \text{ cm}^{-2}$. It has been reported that water vapor has a *p*-type doping effect on graphene surfaces. The slight reduction in electron density could be explained by the diffusion of the water vapor through the doping stacks. However, this *p*-type doping is not stable. The doping effect is reversible when the water vapor is desorbed from the doping stack. At PTB, the device was stored in an N₂ container without humidity at room temperature. When the device was returned to PTB and stored in a dry environment, the electron density slowly increased to a value above $2.00 \times 10^{11} \text{ cm}^{-2}$ and then fluctuated around a mean value of $2.30 \times 10^{11} \text{ cm}^{-2}$ in the following period of over 1.5 years.

Table A1-1. Carrier density and mobility of Device G31 in seven cool-down cycles. Device G31 was shipped from PTB to BIPM and finally returned to PTB.

Cool-down cycles	Time [day]	n [cm ⁻²]	μ [cm ² V ⁻¹ s ⁻¹]
1_PTB	0	9.06×10^{10}	9420
2_BIPM (CCC)	30	2.31×10^{11}	6537
3_BIPM (CCC)	56	1.09×10^{11}	9362
4_PTB	74	1.56×10^{11}	7425
5_PTB	136	2.09×10^{11}	6598
6_PTB (CCC)	486	2.48×10^{11}	6679
7_PTB (CCC)	714	2.04×10^{11}	6689

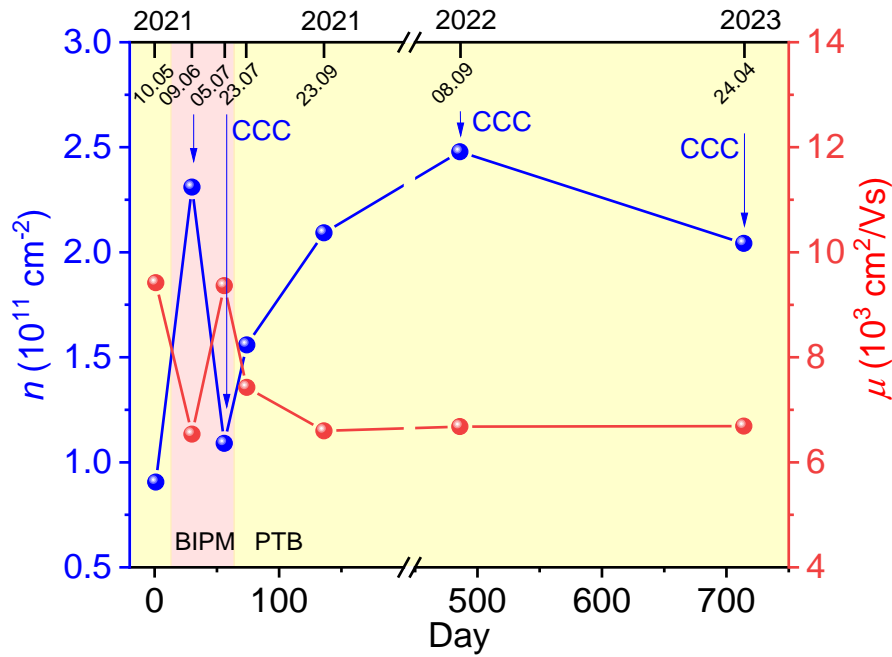


Figure A1.1 Variation of carrier density and mobility of Device G31 as a function of time. The blue arrows indicate the dates of CCC-based high-accuracy measurements at a current of $38.7 \mu\text{A}$ and temperature of 4.2 K . Device D31 was stored in a closed chamber with the mixture of N_2 and air at a low humidity below 40% at room temperature at PTB. Subsequently, the device was placed in a glass bottle filled with N_2 and transported from PTB to BIPM by commercial express. Device D31 was stored in air at a high humidity range from 50% to 80% at room temperature at BIPM. Upon its return to PTB, the device was once again stored in the closed chamber with low humidity at room temperature for the long-term stability investigation.

Figure A1.2 presents the high-accuracy measurements of Device G31 at a temperature of 4.2 K and a current of $38.7 \mu\text{A}$ in two metrology institutes, PTB and BIPM. The quantization regime was observed at $\approx 5.5 \text{ T}$, as marked in red. The accuracy of the graphene QHR standard has remained at both institutes without any sign of degradation. In Figure A1.2(b), the quantization regime shifts to 4.0 T because the electron density is reduced from $2.31 \times 10^{11} \text{ cm}^{-2}$ to $1.09 \times 10^{11} \text{ cm}^{-2}$, which is consistent with the contour plot in Figure 6.7. With the electron density increasing, the quantization regime is shifted to $\approx 5.5 \text{ T}$ again, as shown in Figure A1.2(c). The onset of the quantization regime is correlated with the electron density.

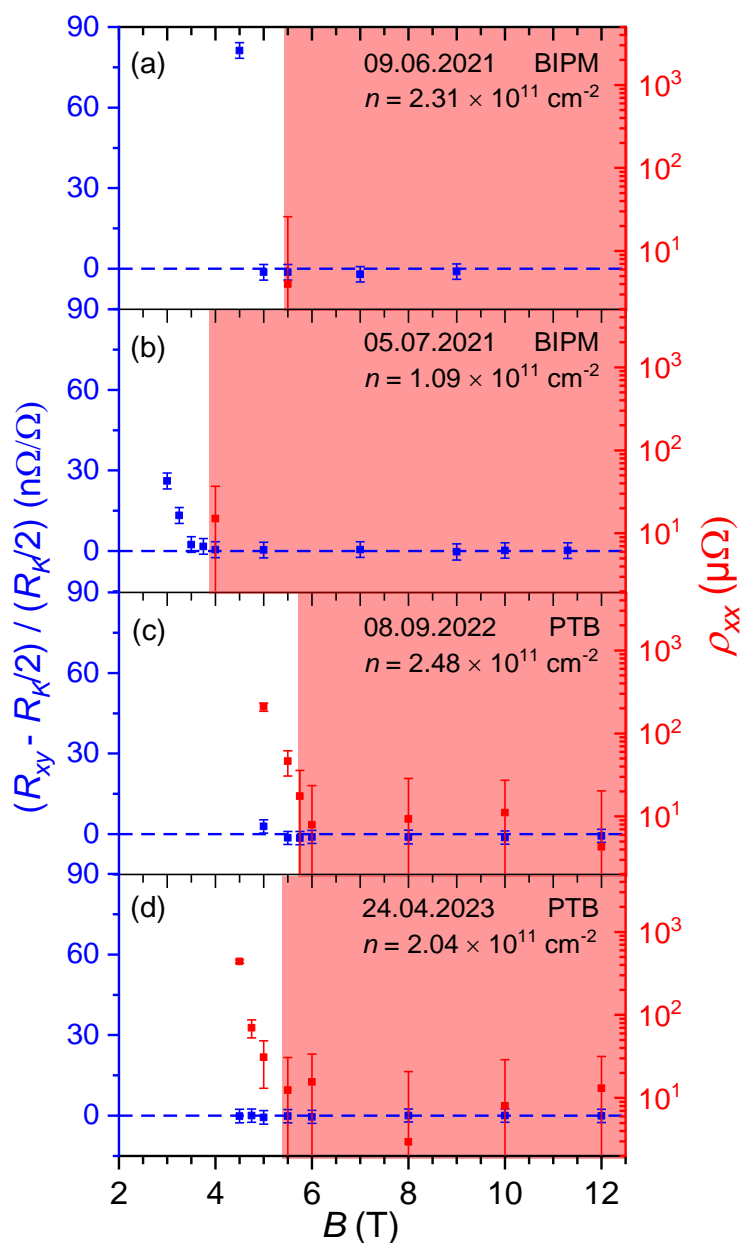


Figure A1.2. Dependence of the Hall resistance quantization on magnetic field for device G31 at $T = 4.2$ K and $I = 38.7$ μA at two metrology institutes, PTB and BIPM. Device G31 was stored in an N_2 container at PTB and then delivered to BIPM. The relative deviation of R_{xy} from $R_K/2$ and the longitudinal resistivity ρ_{xx} are plotted as functions of the magnetic field. The electron density values measured at BIPM are (a) $2.31 \times 10^{11} \text{ cm}^{-2}$ and (b) $1.09 \times 10^{11} \text{ cm}^{-2}$, respectively; the values measured at PTB are (c) $2.48 \times 10^{11} \text{ cm}^{-2}$ and (d) $2.04 \times 10^{11} \text{ cm}^{-2}$. The onset of the $n\Omega/\Omega$ -level quantization was observed at about 4 – 6 T in all the measurements. Again, the magnetic field ranges in which a $n\Omega/\Omega$ -level quantization is reached are highlighted in red.

A.2 Metal and insulating behavior of F4-TCNQ doped graphene

The density-dependent and temperature-dependent conductivity (resistivity) in exfoliated graphene have been widely investigated in experiments and theory. The temperature dependence of the graphene conductivity (resistivity) arises from many competing mechanisms, even without considering any phonon effects, such as thermal excitation of carriers from the valence band to the conduction band, temperature-dependent screening, thermal activation across the potential fluctuations associated with the electron-hole puddles. [181] Due to the additional interaction between the graphene and the buffer layer/SiC, the density-dependent and temperature-dependent resistivity in epitaxial graphene exhibits unique transport properties.

Here, the temperature-dependent sheet resistance was investigated in epitaxial graphene with different electron densities. By precise adjustment of the F4-TCNQ concentration, the carrier density in epitaxial graphene can be tuned to different levels, as discussed in Chapter 4. Figure A2 presents the sheet resistance as a function of temperature for different electron density Hall bar devices. At the temperature below 30 K, the sheet resistance increases as the temperature decreases. This increasing sheet resistance at $T < 30$ K in epitaxial graphene is attributed to the Aronov-Altshuler electron-electron correction and weak localized contribution. [182] At the temperature from 30 K to 300 K, the sheet resistance of graphene exhibits metal behavior for the high electron densities ($n_e \geq 1.11 \times 10^{11} \text{ cm}^{-2}$), and insulating behavior for the low electron density ($n_e = 5.47 \times 10^{10} \text{ cm}^{-2}$).

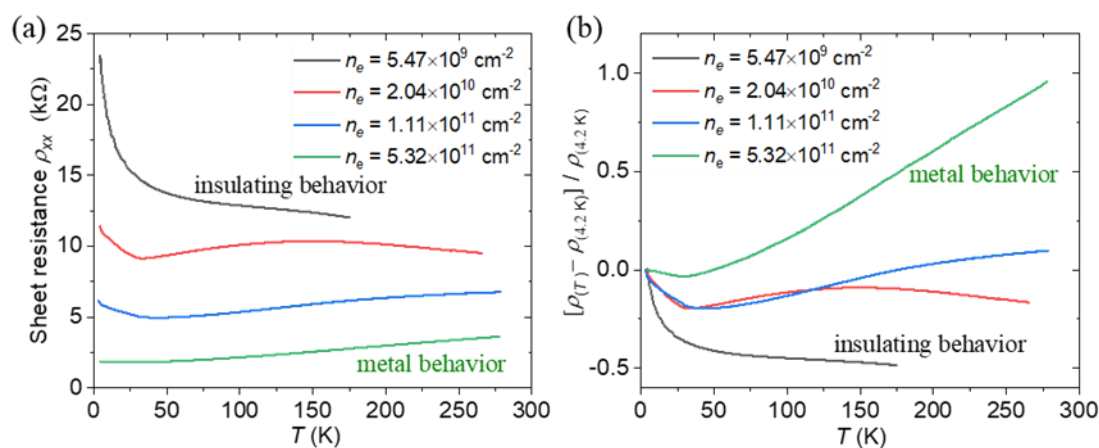


Figure A2 Temperature dependence of sheet resistance ρ of the F4-TCNQ doped epitaxial graphene with different electron densities. (a) The sheet resistance, and (b) the ratio of sheet resistance as a function of temperature for the F4-TCNQ doped epitaxial graphene.

A.3 Observation of the breakdown of Fermi-level pinning

Here, we observed the breakdown of the Fermi level pinning in epitaxial graphene with extremely low electron and hole densities. At the electron density on the level of 10^{11} cm^{-2} , a very broad plateau was observed in magnetic fields up to 35 T at 4.2 K, as shown in Figure A3(a). As the electron density decreases to the level of 10^{10} cm^{-2} , the very broad plateau still exists. The data didn't present here. However, as the electron density decreases to the level of 10^9 cm^{-2} , the plateau starts to be observed at 0.3 T and breaks down at 5 T. A similar result was also observed in the *p*-type graphene. The extremely high density of epitaxial graphene obtained by F4-TCNQ doping. In Figure A3, the Hall plateau onset is observed at 0.5 T, and the plateau starts to break down at 1.3 T. In contrast to the well-known wide and robust Hall plateau in high electron density ($\sim 10^{11} \text{ cm}^{-2}$), the rather narrow plateaus at $\nu = 2$ in low electron and hole densities ($\sim 10^9 \text{ cm}^{-2}$) were observed. The narrow plateau indicates the breakdown of the Fermi level pinning in the epitaxial graphene with extremely low carrier density.

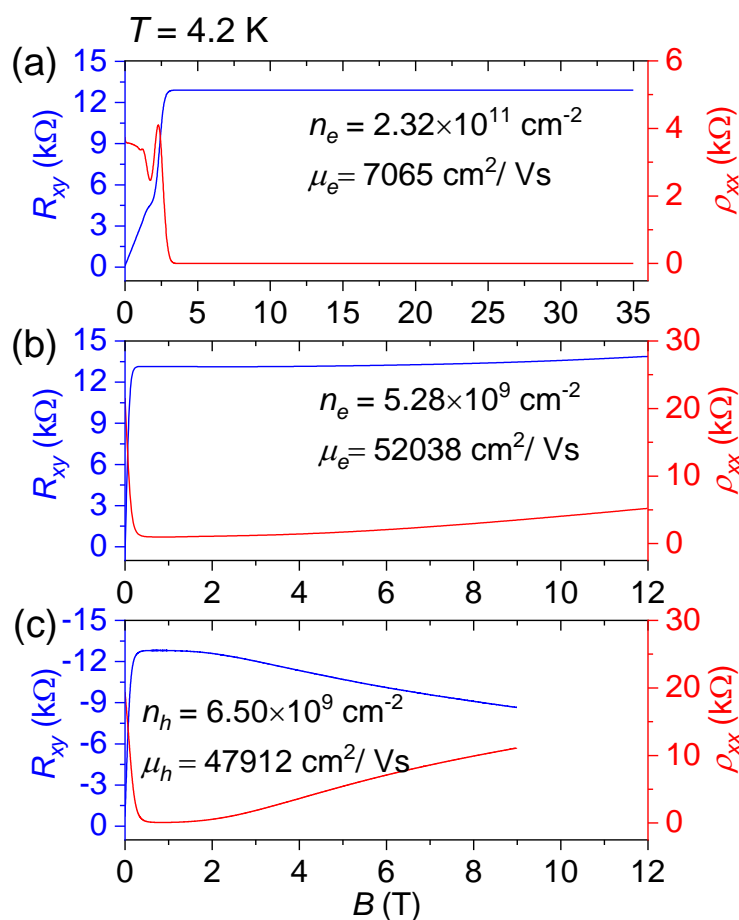


Figure A3 The breakdown of the Fermi level pinning in epitaxial graphene. The QHE measurements of epitaxial graphene with an electron density of (a) $2.32 \times 10^{11} \text{ cm}^{-2}$, (b) $5.28 \times 10^9 \text{ cm}^{-2}$, and hole density of (c) $6.50 \times 10^9 \text{ cm}^{-2}$ at 4.2 K.

A.4 Temperature-dependent QHE of *p*-type epitaxial graphene

Figure A4 presents the temperature-dependent QHR of *p*-type epitaxial graphene. The carrier density is reduced by F4-TCNQ doping to an extremely low value in *p*-type, $n_h = 5.14 \times 10^9 \text{ cm}^{-2}$ ($E_F = 8.4 \text{ meV}$) at 1.4 K. The hole density increases as the temperature increases, as shown in Table A4-1. At temperatures above 77 K, the thermal excitation of carriers from the valence band to the conduction band dominates the Hall slopes. Due to the ambipolar carrier transport (coexistence of electrons and holes by thermal excitation) at $T > 77 \text{ K}$ (6.6 meV), the absolute values of Hall slopes dramatically decrease, and the Hall plateau is destroyed. At temperatures below 77 K, only holes dominate the QH transport, while the thermal excited electron can be ignored.

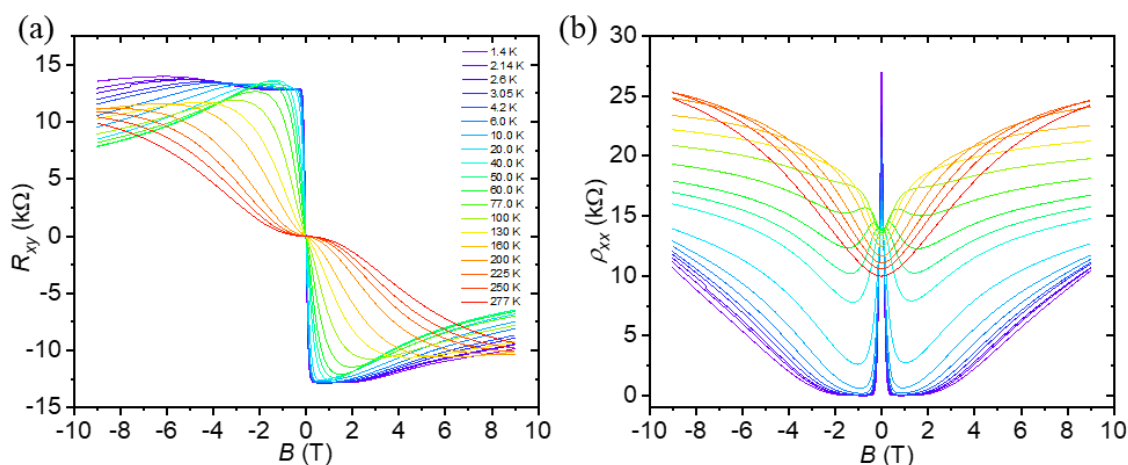


Figure A4 (a) The Hall resistance R_{xy} and (b) the longitudinal resistivity ρ_{xx} as a function of the magnetic field at temperatures from 1.4 K to 277 K in magnetic fields up to 9 T for *p*-type epitaxial graphene. The current is 1 μA in the quantum Hall effect measurement.

Table A4-1 presents the hole density (in zero magnetic fields) of *p*-type epitaxial graphene at $T \leq 77 \text{ K}$. The carrier density is calculated from the Hall slopes. In the absence of charge transfer process, in theory, the central position (B) of the Hall plateau at $\nu = 2$ in magnetic fields is presented in the Table. The value B is calculated from the theory $B = n_h h / (2e)$, where n_h is the hole density, h the Plank constant, and e the elementary charge. The experimental central position (B^*) of the Hall plateau at $\nu = 2$ is determined at the minimum longitudinal resistance in magnetic fields. The central position is larger in experiment (B^*) than in theory (B). This can be explained by the charge transfer model in epitaxial graphene. [111,135,141] According to the experimental value of B^* , the hole density in magnetic fields can be deduced, $n_h(B^*) = 2eB^*/h$, as presented in Table A4-1. Thus, the amounts of holes transferred from the SiC substrate to graphene in a magnetic field are calculated by $\Delta n_h = n_h(B^*) - n_h$.

Table A4-1. The temperature-dependent QHE measurements. The hole density of *p*-type epitaxial graphene increases as temperature increases. The experimental central position (B^*) of the Hall plateau at $\nu = 2$ is determined at the minimum longitudinal resistance in a magnetic field. The amount of charge transfer in magnetic fields at different temperatures is calculated.

T (K)	$n_h(B=0)$ (cm^{-2})	Central position of plateau at $\nu = 2$		$n_h^*(B^*)$ (cm^{-2})	$\Delta n_h =$ $n_h^* - n_h$ (cm^{-2})
		Theory B (T)	Exp. B^* (T)		
1.4	5.14×10^9	0.106	0.720	3.48×10^{10}	2.97×10^{10}
2.1	5.55×10^9	0.115	0.780	3.77×10^{10}	3.22×10^{10}
3.0	6.11×10^9	0.126	0.820	3.97×10^{10}	3.36×10^{10}
4.2	6.50×10^9	0.134	0.845	4.09×10^{10}	3.44×10^{10}
6.0	7.04×10^9	0.146	0.870	4.21×10^{10}	3.50×10^{10}
10	8.07×10^9	0.167	0.913	4.42×10^{10}	3.61×10^{10}
20	1.07×10^{10}	0.221	1.042	5.04×10^{10}	3.97×10^{10}
40	1.98×10^{10}	0.409	1.276	6.17×10^{10}	4.20×10^{10}
50	2.69×10^{10}	0.555	1.414	6.84×10^{10}	4.15×10^{10}
60	3.56×10^{10}	0.736	1.532	7.41×10^{10}	3.85×10^{10}
77	6.00×10^{10}	1.241	1.700	8.22×10^{10}	2.22×10^{10}

Bibliography

- [1] A. C. Neto, F. Guinea, and N. M. Peres, *Drawing Conclusions from Graphene*, Phys. World **19**, 33 (2006).
- [2] K. C. Yung, W. M. Wu, M. P. Pierpoint, and F. V. Kusmartsev, *Introduction to Graphene Electronics – a New Era of Digital Transistors and Devices*, Contemp. Phys. **54**, 233 (2013).
- [3] G. Yazdi, T. Iakimov, and R. Yakimova, *Epitaxial Graphene on SiC: A Review of Growth and Characterization*, Crystals **6**, 53 (2016).
- [4] A. H. Castro Neto, F. Guinea, N. M. R. Peres, K. S. Novoselov, and A. K. Geim, *The Electronic Properties of Graphene*, Rev. Mod. Phys. **81**, 109 (2009).
- [5] K. S. Novoselov, A. K. Geim, S. V. Morozov, D. Jiang, M. I. Katsnelson, I. V. Grigorieva, S. V. Dubonos, and A. A. Firsov, *Two-Dimensional Gas of Massless Dirac Fermions in Graphene*, Nature **438**, 197 (2005).
- [6] Y. M. Lin, C. Dimitrakopoulos, K. A. Jenkins, D. B. Farmer, H. Y. Chiu, A. Grill, and P. Avouris, *100-GHz Transistors from Wafer-Scale Epitaxial Graphene*, Science (80-.). **327**, 662 (2010).
- [7] F. Schedin, A. K. Geim, S. V. Morozov, E. W. Hill, P. Blake, M. I. Katsnelson, and K. S. Novoselov, *Detection of Individual Gas Molecules Adsorbed on Graphene*, Nat. Mater. **6**, 652 (2007).
- [8] A. Tzalenchuk, S. Lara-Avila, A. Kalaboukhov, S. Paolillo, M. Syväjärvi, R. Yakimova, O. Kazakova, T. J. B. M. Janssen, V. Fal'ko, and S. Kubatkin, *Towards a Quantum Resistance Standard Based on Epitaxial Graphene*, Nat. Nanotechnol. **5**, 186 (2010).
- [9] C. Schafhaeutl, *Ueber Die Verbindungen Des Kohlenstoffes Mit Silicium, Eisen Und Anderen Metallen, Welche Die Verschiedenen Gallungen von Roheisen, Stahl Und Schmiedeeisen Bilden*, J. Für Prakt. Chemie **21**, 129 (1840).
- [10] D. R. Dreyer, R. S. Ruoff, and C. W. Bielawski, *From Conception to Realization: An Historical Account of Graphene and Some Perspectives for Its Future*, Angew. Chemie Int. Ed. **49**, 9336 (2010).
- [11] *XIII. On the Atomic Weight of Graphite*, Philos. Trans. R. Soc. London **149**, 249 (1859).

- [12] B. C. Brodie, *XXIII.—Researches on the Atomic Weight of Graphite*, Q. J. Chem. Soc. London **12**, 261 (1860).
- [13] H. P. Boehm, A. Clauss, G. O. Fischer, and U. Hofmann, *Dünnste Kohlenstoff-Folien*, Zeitschrift Fur Naturforsch. - Sect. B J. Chem. Sci. **17**, 150 (1962).
- [14] A. J. Van Bommel, J. E. Crombeen, and A. Van Tooren, *LEED and Auger Electron Observations of the SiC(0001) Surface*, Surf. Sci. **48**, 463 (1975).
- [15] H.-S. Choo et al., *Tailoring Graphite with the Goal of Achieving Single Sheets*, Nanotechnology **10**, 269 (1999).
- [16] K. S. Novoselov, A. K. Geim, S. V. Morozov, D. Jiang, Y. Zhang, S. V. Dubonos, I. V. Grigorieva, and A. A. Firsov, *Electric Field Effect in Atomically Thin Carbon Films*, Science **306**, 666 (2004).
- [17] A. K. Geim, *Random Walk to Graphene (Nobel Lecture)*, Angew. Chemie Int. Ed. **50**, 6966 (2011).
- [18] B. Lang, *A LEED Study of the Deposition of Carbon on Platinum Crystal Surfaces*, Surf. Sci. **53**, 317 (1975).
- [19] A. K. Geim and K. S. Novoselov, *The Rise of Graphene*, Nat. Mater. **6**, 183 (2007).
- [20] P. R. Wallace, *The Band Theory of Graphite*, Phys. Rev. **71**, 622 (1947).
- [21] D. P. DiVincenzo and E. J. Mele, *Self-Consistent Effective-Mass Theory for Intralayer Screening in Graphite Intercalation Compounds*, Phys. Rev. B **29**, 1685 (1984).
- [22] Y. H. Wu, T. Yu, and Z. X. Shen, *Two-Dimensional Carbon Nanostructures: Fundamental Properties, Synthesis, Characterization, and Potential Applications*, J. Appl. Phys. **108**, 71301 (2010).
- [23] X. Li, W. Cai, L. Colombo, and R. S. Ruoff, *Evolution of Graphene Growth on Ni and Cu by Carbon Isotope Labeling*, Nano Lett. **9**, 4268 (2009).
- [24] P. W. Sutter, J. I. Flege, and E. A. Sutter, *Epitaxial Graphene on Ruthenium*, Nat. Mater. 2008 75 **7**, 406 (2008).
- [25] P. R. Somani, S. P. Somani, and M. Umeno, *Planer Nano-Graphenes from Camphor by CVD*, Chem. Phys. Lett. **430**, 56 (2006).
- [26] Y. M. Tairov and V. F. Tsvetkov, *Investigation of Growth Processes of Ingots of Silicon*

- Carbide Single Crystals*, J. Cryst. Growth **43**, 209 (1978).
- [27] Y. M. Tairov and V. F. Tsvetkov, *General Principles of Growing Large-Size Single Crystals of Various Silicon Carbide Polytypes*, J. Cryst. Growth **52**, 146 (1981).
- [28] A. Nagashima, K. Nuka, K. Satoh, H. Itoh, T. Ichinokawa, C. Oshima, and S. Otani, *Electronic Structure of Monolayer Graphite on Some Transition Metal Carbide Surfaces*, Surf. Sci. **287**, 609 (1993).
- [29] K. V Emtsev et al., *Towards Wafer-Size Graphene Layers by Atmospheric Pressure Graphitization of Silicon Carbide*, Nat. Mater. **8**, 203 (2009).
- [30] S. K. Lilov, *Study of the Equilibrium Processes in the Gas Phase during Silicon Carbide Sublimation*, Mater. Sci. Eng. B **21**, 65 (1993).
- [31] G. G. Jernigan, B. L. VanMil, J. L. Tedesco, J. G. Tischler, E. R. Glaser, A. Davidson, P. M. Campbell, and D. K. Gaskill, *Comparison of Epitaxial Graphene on Si-Face and C-Face 4H SiC Formed by Ultrahigh Vacuum and RF Furnace Production*, Nano Lett. **9**, 2605 (2009).
- [32] C. Berger et al., *Ultrathin Epitaxial Graphite: 2D Electron Gas Properties and a Route toward Graphene-Based Nanoelectronics*, J. Phys. Chem. B **108**, 19912 (2004).
- [33] G. Landwehr, *The Discovery of the Quantum Hall Effect*, Metrologia **22**, 118 (1986).
- [34] K. V. Klitzing, G. Dorda, and M. Pepper, *New Method for High-Accuracy Determination of the Fine-Structure Constant Based on Quantized Hall Resistance*, Phys. Rev. Lett. **45**, 494 (1980).
- [35] C.-C. Kalmbach, J. Schurr, F. J. Ahlers, A. Müller, S. Novikov, N. Lebedeva, and A. Satrapinski, *Towards a Graphene-Based Quantum Impedance Standard*, Appl. Phys. Lett. **105**, 073511 (2014).
- [36] M. Marzano, Y. Pimsut, M. Kruskopf, Y. Yin, M. Kraus, V. D'Elia, L. Callegaro, M. Ortolano, S. Bauer, and R. Behr, *PTB–INRIM Comparison of Novel Digital Impedance Bridges with Graphene Impedance Quantum Standards*, Metrologia **59**, 065001 (2022).
- [37] W. Poirier, F. Lafont, S. Djordjevic, F. Schopfer, and L. Devoille, *A Programmable Quantum Current Standard from the Josephson and the Quantum Hall Effects*, J. Appl. Phys. **115**, 044509 (2014).
- [38] A. Laucht et al., *Roadmap on Quantum Nanotechnologies*, Nanotechnology **32**, 162003

- (2021).
- [39] J. H. Sanders and A. H. Wapstra, editors, *Atomic Masses and Fundamental Constants 5* (Springer US, Boston, MA, 1976).
- [40] F. Schopfer and W. Poirier, *Quantum Resistance Standard Accuracy Close to the Zero-Dissipation State*, J. Appl. Phys. **114**, 064508 (2013).
- [41] F. Delahaye and B. Jeckelmann, *Revised Technical Guidelines for Reliable Dc Measurements of the Quantized Hall Resistance*, Metrologia **40**, 217 (2003).
- [42] Y. Zhang, Y.-W. Tan, H. L. Stormer, and P. Kim, *Experimental Observation of the Quantum Hall Effect and Berry's Phase in Graphene*, Nature **438**, 201 (2005).
- [43] K. S. Novoselov, Z. Jiang, Y. Zhang, S. V Morozov, H. L. Stormer, U. Zeitler, J. C. Maan, G. S. Boebinger, P. Kim, and A. K. Geim, *Room-Temperature Quantum Hall Effect in Graphene*, Science **315**, 1379 (2007).
- [44] T. J. B. M. Janssen, A. Tzalenchuk, S. Lara-Avila, S. Kubatkin, and V. I. Fal'ko, *Quantum Resistance Metrology Using Graphene*, Reports Prog. Phys. **76**, 104501 (2013).
- [45] T. J. B. M. Janssen, N. E. Fletcher, R. Goebel, J. M. Williams, A. Tzalenchuk, R. Yakimova, S. Kubatkin, S. Lara-Avila, and V. I. Fal'ko, *Graphene, Universality of the Quantum Hall Effect and Redefinition of the SI System*, New J. Phys. **13**, 093026 (2011).
- [46] T. J. B. M. Janssen, J. M. Williams, N. E. Fletcher, R. Goebel, A. Tzalenchuk, R. Yakimova, S. Lara-Avila, S. Kubatkin, and V. I. Fal'ko, *Precision Comparison of the Quantum Hall Effect in Graphene and Gallium Arsenide*, Metrologia **49**, 294 (2012).
- [47] R. Ribeiro-Palau et al., *Quantum Hall Resistance Standard in Graphene Devices under Relaxed Experimental Conditions*, Nat. Nanotechnol. **10**, 965 (2015).
- [48] F. Lafont et al., *Quantum Hall Resistance Standards from Graphene Grown by Chemical Vapour Deposition on Silicon Carbide*, Nat. Commun. **6**, 6806 (2015).
- [49] H. He et al., *Polymer-Encapsulated Molecular Doped Epigraphene for Quantum Resistance Metrology*, Metrologia **56**, 045004 (2019).
- [50] D.-H. Chae et al., *Investigation of the Stability of Graphene Devices for Quantum Resistance Metrology at Direct and Alternating Current*, Meas. Sci. Technol. **33**, 065012 (2022).

-
- [51] Y. Yin, A. Chatterjee, D. Momeni, M. Kruskopf, M. Götz, S. Wundrack, F. Hohls, K. Pierz, and H. W. Schumacher, *Tailoring Permanent Charge Carrier Densities in Epitaxial Graphene on SiC by Functionalization with F4-TCNQ*, *Adv. Phys. Res.* **1**, 2200015 (2022).
- [52] N. Shetty, T. Bergsten, G. Eklund, S. L. Avila, S. Kubatkin, K. Cedergren, and H. He, *Long-Term Stability of Molecular Doped Epigraphene Quantum Hall Standards: Single Elements and Large Arrays ($R_K/236 \approx 109 \Omega$)*, *Metrologia* **60**, 055009 (2023).
- [53] A. Chatterjee et al., *Performance and Stability Assessment of Graphene-Based Quantum Hall Devices for Resistance Metrology*, *IEEE Trans. Instrum. Meas.* **72**, 1 (2023).
- [54] N. J. Huang, *Magnetotransport in Graphene and Related Two-Dimensional Systems*, Ph.D. dissertation, University of Oxford, 2016.
- [55] M.-M. Dubois, Z. Zanolli, X. Declerck, and J.-C. Charlier, *Electronic Properties and Quantum Transport in Graphene-Based Nanostructures*, *Eur. Phys. J. B* **72**, 1 (2009).
- [56] R. Saito, M. Fujita, G. Dresselhaus, and M. S. Dresselhaus, *Electronic Structure of Chiral Graphene Tubules*, *Appl. Phys. Lett.* **60**, 2204 (1992).
- [57] S. Reich, J. Maultzsch, C. Thomsen, and P. Ordejón, *Tight-Binding Description of Graphene*, *Phys. Rev. B - Condens. Matter Mater. Phys.* **66**, 354121 (2002).
- [58] R. S. Deacon, K. C. Chuang, R. J. Nicholas, K. S. Novoselov, and A. K. Geim, *Cyclotron Resonance Study of the Electron and Hole Velocity in Graphene Monolayers*, *Phys. Rev. B - Condens. Matter Mater. Phys.* **76**, 2 (2007).
- [59] E. H. Hall, *On a New Action of the Magnet on Electric Currents*, *Am. J. Math.* **2**, 287 (1879).
- [60] K. I. Bolotin, F. Ghahari, M. D. Shulman, H. L. Stormer, and P. Kim, *Observation of the Fractional Quantum Hall Effect in Graphene*, *Nature* **462**, 196 (2009).
- [61] D. Vaquero et al., *Phonon-Mediated Room-Temperature Quantum Hall Transport in Graphene*, *Nat. Commun.* **14**, 318 (2023).
- [62] SI Brochure: The International System of Units (SI), 9th Edition, 2022.
- [63] L. D. Landau and E. M. Lifshitz, *Quantum Mechanics : Non-Relativistic Theory*. Second edition, revised and enlarged, Pergamon Press Led. 1965.

- [64] B. I. Halperin, *Quantized Hall Conductance, Current-Carrying Edge States, and the Existence of Extended States in a Two-Dimensional Disordered Potential*, Phys. Rev. B **25**, 2185 (1982).
- [65] M. Büttiker, *Absence of Backscattering in the Quantum Hall Effect in Multiprobe Conductors*, Phys. Rev. B **38**, 9375 (1988).
- [66] Y. Zhang, Z. Jiang, J. P. Small, M. S. Purewal, Y.-W. Tan, M. Fazlollahi, J. D. Chudow, J. A. Jaszczak, H. L. Stormer, and P. Kim, *Landau-Level Splitting in Graphene in High Magnetic Fields*, Phys. Rev. Lett. **96**, 136806 (2006).
- [67] J. Chan, A. Venugopal, A. Pirkle, S. McDonnell, D. Hinojos, C. W. Magnuson, R. S. Ruoff, L. Colombo, R. M. Wallace, and E. M. Vogel, *Reducing Extrinsic Performance-Limiting Factors in Graphene Grown by Chemical Vapor Deposition*, ACS Nano **6**, 3224 (2012).
- [68] C. Virojanadara, M. Syväjarvi, R. Yakimova, L. I. Johansson, A. A. Zakharov, and T. Balasubramanian, *Homogeneous Large-Area Graphene Layer Growth on 6H-SiC(0001)*, Phys. Rev. B **78**, 245403 (2008).
- [69] M. Ostler, F. Speck, M. Gick, and T. Seyller, *Automated Preparation of High-quality Epitaxial Graphene on 6H-SiC(0001)*, Phys. Status Solidi **247**, 2924 (2010).
- [70] M. Kruskopf, *Epitaxial Graphene on SiC for Quantum Resistance Metrology*, PhD dissertation. Technischen Universität Braunschweig, 2017.
- [71] M. Kruskopf et al., *Comeback of Epitaxial Graphene for Electronics: Large-Area Growth of Bilayer-Free Graphene on SiC*, 2D Mater. **3**, 041002 (2016).
- [72] M. Kruskopf, K. Pierz, D. M. Pakdehi, S. Wundrack, R. Stosch, A. Bakin, and H. W. Schumacher, *A Morphology Study on the Epitaxial Growth of Graphene and Its Buffer Layer*, Thin Solid Films **659**, 7 (2018).
- [73] D. Momeni Pakdehi, *Optimization of Epitaxial Graphene Growth for Quantum Metrology*, PhD dissertation, Leibniz Universität Hannover, 2020.
- [74] K. V Emtsev, F. Speck, T. Seyller, L. Ley, and J. D. Riley, *Interaction, Growth, and Ordering of Epitaxial Graphene on SiC(0001) Surfaces: A Comparative Photoelectron Spectroscopy Study*, Phys. Rev. B - Condens. Matter Mater. Phys. **77**, 155303 (2008).
- [75] J. B. Hannon, M. Copel, and R. M. Tromp, *Direct Measurement of the Growth Mode of*

-
- Graphene on SiC(0001) and SiC(0001)*, Phys. Rev. Lett. **107**, 166101 (2011).
- [76] J. B. Pawley, *Handbook of Biological Confocal Microscopy: Third Edition* (Springer US, 2006).
- [77] Evident GmbH, *Introduction to Confocal Microscopy*, <https://www.olympus-lifescience.com/en/microscope-resource/primer/techniques/confocal/confocalintro/>.
- [78] Park System, *AFM Works*, <https://www.parksystems.com/learning-center/nano-academy/how-afm-works>.
- [79] Y. Yang, L. Huang, Y. Fukuyama, F. Liu, M. A. Real, P. Barbara, C. Liang, D. B. Newell, and R. E. Elmquist, *Low Carrier Density Epitaxial Graphene Devices On SiC*, Small **11**, 90 (2015).
- [80] M. Kruskopf, A. F. Rigosi, A. R. Panna, D. K. Patel, H. Jin, M. Marzano, M. Berilla, D. B. Newell, and R. E. Elmquist, *Two-Terminal and Multi-Terminal Designs for Next-Generation Quantized Hall Resistance Standards: Contact Material and Geometry*, IEEE Trans. Electron Devices **66**, 3973 (2019).
- [81] C. Chuang, Y. Yang, S. Pookpanratana, C. A. Hacker, C.-T. Liang, and R. E. Elmquist, *Chemical-Doping-Driven Crossover from Graphene to “Ordinary Metal” in Epitaxial Graphene Grown on SiC*, Nanoscale **9**, 11537 (2017).
- [82] A. J. M. Giesbers, P. Procházka, and C. F. J. Flipse, *Surface Phonon Scattering in Epitaxial Graphene on 6H-SiC*, Phys. Rev. B **87**, 195405 (2013).
- [83] C. Coletti, C. Riedl, D. S. Lee, B. Krauss, L. Patthey, K. von Klitzing, J. H. Smet, and U. Starke, *Charge Neutrality and Band-Gap Tuning of Epitaxial Graphene on SiC by Molecular Doping*, Phys. Rev. B **81**, 235401 (2010).
- [84] B. Jeckelmann and B. Jeanneret, *The Quantum Hall Effect as an Electrical Resistance Standard*, Reports Prog. Phys. **64**, 1603 (2001).
- [85] J. M. Williams, T. J. B. M. Janssen, G. Rietveld, and E. Houtzager, *An Automated Cryogenic Current Comparator Resistance Ratio Bridge for Routine Resistance Measurements*, Metrologia **47**, 167 (2010).
- [86] K. Pierz, M. Gotz, E. Pesel, F.-J. Ahlers, and H. W. Schumacher, *Quantum Hall Resistance Standards With Good Quantization at High Electron Mobilities*, IEEE Trans. Instrum. Meas. **60**, 2455 (2011).

-
- [87] M. Sprinkle, P. Soukiassian, W. A. de Heer, C. Berger, and E. H. Conrad, *Epitaxial Graphene: The Material for Graphene Electronics*, Phys. Status Solidi - Rapid Res. Lett. **3**, A91 (2009).
- [88] M. Beshkova, L. Hultman, and R. Yakimova, *Device Applications of Epitaxial Graphene on Silicon Carbide*, Vacuum **128**, 186 (2016).
- [89] I. Gierz, C. Riedl, U. Starke, C. R. Ast, and K. Kern, *Atomic Hole Doping of Graphene*, Nano Lett. **8**, 4603 (2008).
- [90] P. Willke, J. A. Amani, A. Sinterhauf, S. Thakur, T. Kotzott, T. Druga, S. Weikert, K. Maiti, H. Hofsäss, and M. Wenderoth, *Doping of Graphene by Low-Energy Ion Beam Implantation: Structural, Electronic, and Transport Properties*, Nano Lett. **15**, 5110 (2015).
- [91] T. Shen, J. J. Gu, M. Xu, Y. Q. Wu, M. L. Bolen, M. A. Capano, L. W. Engel, and P. D. Ye, *Observation of Quantum-Hall Effect in Gated Epitaxial Graphene Grown on SiC (0001)*, Appl. Phys. Lett. **95**, 172105 (2009).
- [92] A. Lartsev, T. Yager, T. Bergsten, A. Tzalenchuk, T. J. B. M. Janssen, R. Yakimova, S. Lara-Avila, and S. Kubatkin, *Tuning Carrier Density across Dirac Point in Epitaxial Graphene on SiC by Corona Discharge*, Appl. Phys. Lett. **105**, 063106 (2014).
- [93] S. Lara-Avila, K. Moth-Poulsen, R. Yakimova, T. Bjørnholm, V. Fal'ko, A. Tzalenchuk, and S. Kubatkin, *Non-Volatile Photochemical Gating of an Epitaxial Graphene/Polymer Heterostructure*, Adv. Mater. **23**, 878 (2011).
- [94] Y. Yang et al., *Epitaxial Graphene Homogeneity and Quantum Hall Effect in Millimeter-Scale Devices*, Carbon N. Y. **115**, 229 (2017).
- [95] S. M. Mhatre, N. T. M. Tran, H. M. Hill, D. Saha, A. R. Hight Walker, C.-T. Liang, R. E. Elmquist, D. B. Newell, and A. F. Rigosi, *Dynamics of Transient Hole Doping in Epitaxial Graphene*, Phys. Rev. B **105**, 205423 (2022).
- [96] A. Tadich, M. T. Edmonds, L. Ley, F. Fromm, Y. Smets, Z. Mazej, J. Riley, C. I. Pakes, T. Seyller, and M. Wanke, *Tuning the Charge Carriers in Epitaxial Graphene on SiC(0001) from Electron to Hole via Molecular Doping with C60F48*, Appl. Phys. Lett. **102**, 241601 (2013).
- [97] E. Pallecchi, M. Ridene, D. Kazazis, C. Mathieu, F. Schopfer, W. Poirier, D. Mailly, and

- A. Ouerghi, *Observation of the Quantum Hall Effect in Epitaxial Graphene on SiC(0001) with Oxygen Adsorption*, Appl. Phys. Lett. **100**, 253109 (2012).
- [98] S. Novikov, N. Lebedeva, K. Pierz, and A. Satrapinski, *Fabrication and Study of Large-Area QHE Devices Based on Epitaxial Graphene*, IEEE Trans. Instrum. Meas. **64**, 1533 (2015).
- [99] T. Oe, A. F. Rigosi, M. Kruskopf, B.-Y. Wu, H.-Y. Lee, Y. Yang, R. E. Elmquist, N.-H. Kaneko, and D. G. Jarrett, *Comparison Between NIST Graphene and AIST GaAs Quantized Hall Devices*, IEEE Trans. Instrum. Meas. **69**, 3103 (2020).
- [100] A. F. Rigosi et al., *Gateless and Reversible Carrier Density Tunability in Epitaxial Graphene Devices Functionalized with Chromium Tricarbonyl*, Carbon N. Y. **142**, 468 (2019).
- [101] J. A. Robinson, M. LaBella, K. A. Trumbull, X. Weng, R. Cavellero, T. Daniels, Z. Hughes, M. Hollander, M. Fanton, and D. Snyder, *Epitaxial Graphene Materials Integration: Effects of Dielectric Overlayers on Structural and Electronic Properties*, ACS Nano **4**, 2667 (2010).
- [102] J. Hu et al., *Towards Epitaxial Graphene P-n Junctions as Electrically Programmable Quantum Resistance Standards*, Sci. Rep. **8**, 15018 (2018).
- [103] M. S. Bresnehan, M. J. Hollander, R. L. Marucci, M. LaBella, K. A. Trumbull, R. Cavellero, D. W. Snyder, and J. A. Robinson, *Advancing Quasi-Freestanding Epitaxial Graphene Electronics through Integration of Wafer Scale Hexagonal Boron Nitride Dielectrics*, **846207**, 846207 (2012).
- [104] A. F. Rigosi et al., *Examining Epitaxial Graphene Surface Conductivity and Quantum Hall Device Stability with Parylene Passivation*, Microelectron. Eng. **194**, 51 (2018).
- [105] J. Park, K.-G. Lim, and D.-H. Chae, *Glass Encapsulation of Molecular-Doped Epitaxial Graphene for Quantum Resistance Metrology*, Meas. Sci. Technol. **33**, 115019 (2022).
- [106] W. Chen, S. Chen, D. C. Qi, X. Y. Gao, and A. T. S. Wee, *Surface Transfer P-Type Doping of Epitaxial Graphene*, J. Am. Chem. Soc. **129**, 10418 (2007).
- [107] J. T. Sun, Y. H. Lu, W. Chen, Y. P. Feng, and A. T. S. Wee, *Linear Tuning of Charge Carriers in Graphene by Organic Molecules and Charge-Transfer Complexes*, Phys. Rev. B **81**, 155403 (2010).

- [108] J. Jobst, D. Waldmann, F. Speck, R. Hirner, D. K. Maude, T. Seyller, and H. B. Weber, *Quantum Oscillations and Quantum Hall Effect in Epitaxial Graphene*, Phys. Rev. B - Condens. Matter Mater. Phys. **81**, 195434 (2010).
- [109] H. He et al., *Uniform Doping of Graphene Close to the Dirac Point by Polymer-Assisted Assembly of Molecular Dopants*, Nat. Commun. **9**, 3956 (2018).
- [110] M. Kruskopf and R. E. Elmquist, *Epitaxial Graphene for Quantum Resistance Metrology*, Metrologia **55**, R27 (2018).
- [111] J. A. Alexander-Webber et al., *Giant Quantum Hall Plateaus Generated by Charge Transfer in Epitaxial Graphene*, Sci. Rep. **6**, 30296 (2016).
- [112] X. Tian, J. Xu, and X. Wang, *Band Gap Opening of Bilayer Graphene by F4-TCNQ Molecular Doping and Externally Applied Electric Field*, J. Phys. Chem. B **114**, 11377 (2010).
- [113] S. Tanabe, Y. Sekine, H. Kageshima, M. Nagase, and H. Hibino, *Carrier Transport Mechanism in Graphene on SiC(0001)*, Phys. Rev. B **84**, 115458 (2011).
- [114] S. Cho and M. S. Fuhrer, *Charge Transport and Inhomogeneity near the Minimum Conductivity Point in Graphene*, Phys. Rev. B **77**, 081402 (2008).
- [115] R. P. Tiwari and D. Stroud, *Model for the Magnetoresistance and Hall Coefficient of Inhomogeneous Graphene*, Phys. Rev. B **79**, 165408 (2009).
- [116] M. Knap, J. D. Sau, B. I. Halperin, and E. Demler, *Transport in Two-Dimensional Disordered Semimetals*, Phys. Rev. Lett. **113**, 186801 (2014).
- [117] J. Ping, I. Yudhistira, N. Ramakrishnan, S. Cho, S. Adam, and M. S. Fuhrer, *Disorder-Induced Magnetoresistance in a Two-Dimensional Electron System*, Phys. Rev. Lett. **113**, 047206 (2014).
- [118] M. Yang et al., *Puddle-Induced Resistance Oscillations in the Breakdown of the Graphene Quantum Hall Effect*, Phys. Rev. Lett. **117**, 237702 (2016).
- [119] S. V. Morozov, K. S. Novoselov, M. I. Katsnelson, F. Schedin, D. C. Elias, J. A. Jaszczak, and A. K. Geim, *Giant Intrinsic Carrier Mobilities in Graphene and Its Bilayer*, Phys. Rev. Lett. **100**, 016602 (2008).
- [120] K. Nomura and A. H. MacDonald, *Quantum Transport of Massless Dirac Fermions*, Phys. Rev. Lett. **98**, 1 (2007).

-
- [121] S. Adam, E. H. Hwang, V. M. Galitski, and S. Das Sarma, *A Self-Consistent Theory for Graphene Transport*, Proc. Natl. Acad. Sci. U. S. A. **104**, 18392 (2007).
- [122] E. H. Hwang, S. Adam, and S. Das Sarma, *Carrier Transport in Two-Dimensional Graphene Layers*, Phys. Rev. Lett. **98**, 186806 (2007).
- [123] J.-H. Chen, C. Jang, S. Adam, M. S. Fuhrer, E. D. Williams, and M. Ishigami, *Charged-Impurity Scattering in Graphene*, Nat. Phys. **4**, 377 (2008).
- [124] C. R. Dean et al., *Boron Nitride Substrates for High-Quality Graphene Electronics*, Nat. Nanotechnol. **5**, 722 (2010).
- [125] D. S. Novikov, *Numbers of Donors and Acceptors from Transport Measurements in Graphene*, Appl. Phys. Lett. **91**, 102102 (2007).
- [126] J. Ristein, S. Mammadov, and T. Seyller, *Origin of Doping in Quasi-Free-Standing Graphene on Silicon Carbide*, Phys. Rev. Lett. **108**, 246104 (2012).
- [127] J. Chen, C. Jang, S. Xiao, M. Ishigami, and M. S. Fuhrer, *Intrinsic and Extrinsic Performance Limits of Graphene Devices on SiO₂*, Nat. Nanotechnol. **3**, 206 (2008).
- [128] V. Perebeinos and P. Avouris, *Inelastic Scattering and Current Saturation in Graphene*, Phys. Rev. B **81**, 195442 (2010).
- [129] K. Zou, X. Hong, D. Keefer, and J. Zhu, *Deposition of High-Quality HfO₂ on Graphene and the Effect of Remote Oxide Phonon Scattering*, Phys. Rev. Lett. **105**, 126601 (2010).
- [130] J. Huang et al., *Physics of a Disordered Dirac Point in Epitaxial Graphene from Temperature-Dependent Magnetotransport Measurements*, Phys. Rev. B **92**, 075407 (2015).
- [131] J. Červenka, K. van de Ruit, and C. F. J. Flipse, *Giant Inelastic Tunneling in Epitaxial Graphene Mediated by Localized States*, Phys. Rev. B **81**, 205403 (2010).
- [132] J. Červenka, K. van de Ruit, and C. F. J. Flipse, *Local Enhancement of Inelastic Tunnelling in Epitaxial Graphene on SiC(0001)*, Phys. Status Solidi **247**, 2992 (2010).
- [133] L. Vitali, M. A. Schneider, K. Kern, L. Wirtz, and A. Rubio, *Phonon and Plasmon Excitation in Inelastic Electron Tunneling Spectroscopy of Graphite*, Phys. Rev. B **69**, 121414 (2004).
- [134] W. Chen, D. Qi, X. Gao, and A. T. S. Wee, *Surface Transfer Doping of Semiconductors*,

- Prog. Surf. Sci. **84**, 279 (2009).
- [135] S. Kopylov, A. Tzalenchuk, S. Kubatkin, and V. I. Fal'ko, *Charge Transfer between Epitaxial Graphene and Silicon Carbide*, Appl. Phys. Lett. **97**, 112109 (2010).
- [136] C. Wu, F. Li, and T. Guo, *Efficient Tristable Resistive Memory Based on Single Layer Graphene/Insulating Polymer Multi-Stacking Layer*, Appl. Phys. Lett. **104**, 183105 (2014).
- [137] F. Delahaye, D. Dominguez, F. Alexandre, J. P. Andre, J. P. Hirtz, and M. Razeghi, *Precise Quantized Hall Resistance Measurements in GaAs/Al_xGa_{1-x}As and In_xGa_{1-x}As/InP Heterostructures*, Metrologia **22**, 103 (1986).
- [138] F. Piquemal, G. Geneves, F. Delahaye, J.-P. Andre, J.-N. Patillon, and P. Frijlink, *Report on a Joint BIPM-EUROMET Project for the Fabrication of QHE Samples by the LEP*, IEEE Trans. Instrum. Meas. **42**, 264 (1993).
- [139] R. Ribeiro-Palau et al., *Quantum Hall Resistance Standard in Graphene Devices under Relaxed Experimental Conditions*, Nat. Nanotechnol. **10**, 965 (2015).
- [140] M. Woszczyzna, M. Friedemann, M. Götz, E. Pesel, K. Pierz, T. Weimann, and F. J. Ahlers, *Precision Quantization of Hall Resistance in Transferred Graphene*, Appl. Phys. Lett. **100**, (2012).
- [141] T. J. B. M. Janssen, A. Tzalenchuk, R. Yakimova, S. Kubatkin, S. Lara-Avila, S. Kopylov, and V. I. Fal'ko, *Anomalously Strong Pinning of the Filling Factor $\nu = 2$ in Epitaxial Graphene*, Phys. Rev. B **83**, 233402 (2011).
- [142] J. A. Alexander-Webber, A. M. R. Baker, T. J. B. M. Janssen, A. Tzalenchuk, S. Lara-Avila, S. Kubatkin, R. Yakimova, B. A. Piot, D. K. Maude, and R. J. Nicholas, *Phase Space for the Breakdown of the Quantum Hall Effect in Epitaxial Graphene*, Phys. Rev. Lett. **111**, 096601 (2013).
- [143] D. C. Tsui and A. C. Gossard, *Resistance Standard Using Quantization of the Hall Resistance of GaAs-Al_xGa_{1-x}As Heterostructures*, Appl. Phys. Lett. **38**, 550 (1981).
- [144] M. K. A. Tsukazaki, A. Ohtomo, T. Kita, Y. Ohno, H. Ohno, *Quantum Hall Effect in Polar Oxide Heterostructures*, Science **315**, 1388 (2007).
- [145] D.C. Tsui, H.L. Stormer, A.C. Gossard, *Two-Dimensional Magnetotransport in the Extreme Quantum Limit*, Phys. Rev. Lett. **48**, 1559 (1982).

-
- [146] J. K. Jain, *Composite-Fermion Approach for the Fractional Quantum Hall Effect*, Phys. Rev. Lett. **63**, 199 (1989).
- [147] F. J. Ahlers, M. Götz, and K. Pierz, *Direct Comparison of Fractional and Integer Quantized Hall Resistance*, Metrologia **54**, 516 (2017).
- [148] F. Lafont et al., *Quantum Hall Resistance Standard Based on Graphene Grown by Chemical Vapor Deposition on Silicon Carbide*, Nat. Commun. **6**, 6806 (2015)
- [149] T. J. B. M. Janssen, A. Tzalenchuk, S. Lara-Avila, S. Kubatkin, and V. I. Fal'Ko, *Quantum Resistance Metrology Using Graphene*, Reports Prog. Phys. **76**, (2013).
- [150] M. A. Real, E. A. Lass, F. H. Liu, T. Shen, G. R. Jones, J. A. Soons, D. B. Newell, A. V. Davydov, and R. E. Elmquist, *Graphene Epitaxial Growth on SiC(0001) for Resistance Standards*, IEEE Trans. Instrum. Meas. **62**, 1454 (2013).
- [151] A. C. Betz et al., *Hot Electron Cooling by Acoustic Phonons in Graphene*, Phys. Rev. Lett. **109**, 2 (2012).
- [152] A. J. M. Giesbers, G. Rietveld, E. Houtzager, U. Zeitler, R. Yang, K. S. Novoselov, A. K. Geim, and J. C. Maan, *Quantum Resistance Metrology in Graphene*, Appl. Phys. Lett. **93**, 2 (2008).
- [153] M. Woszczyzna, M. Friedemann, M. Götz, E. Pesel, K. Pierz, T. Weimann, and F. J. Ahlers, *Precision Quantization of Hall Resistance in Transferred Graphene*, Appl. Phys. Lett. **100**, 16 (2012).
- [154] M. Kruskopf, *Epitaxial Graphene on SiC for Quantum Resistance Metrology* (2017).
- [155] A. Satrapinski, S. Novikov, and N. Lebedeva, *Precision Quantum Hall Resistance Measurement on Epitaxial Graphene Device in Low Magnetic Field*, Appl. Phys. Lett. **103**, (2013).
- [156] A. M. R. Baker et al., *Weak Localization Scattering Lengths in Epitaxial, and CVD Graphene*, Phys. Rev. B **86**, 235441 (2012).
- [157] W. Zhu, V. Perebeinos, M. Freitag, and P. Avouris, *Carrier Scattering, Mobilities, and Electrostatic Potential in Monolayer, Bilayer, and Trilayer Graphene*, Phys. Rev. B **80**, 235402 (2009).
- [158] KTH Royal Institute of Technology, *Lift Mode Surface Potential Imaging (AM-KPFM)*, 2 (2019).

- [159] H. He et al., *Polymer-Encapsulated Molecular Doped Epigraphene for Quantum Resistance Metrology*, *Metrologia* **56**, (2019).
- [160] J. A. Alexander-Webber et al., *Giant Quantum Hall Plateaus Generated by Charge Transfer in Epitaxial Graphene*, *Sci. Rep.* **6**, 1 (2016).
- [161] S. V. Kopylov, A. Tzalenchuk, S. Kubatkin, and V. I. Fal'Ko, *Charge Transfer between Epitaxial Graphene and Silicon Carbide*, *Appl. Phys. Lett.* **97**, 2 (2010).
- [162] X. Wan , X. Fan, C. Zhai, Z. Yang , L. Hao, L. Li, Y. Lu, and C. Zeng, *Contrasting Transport Performance of Electron- and Hole-Doped Epitaxial Graphene for Quantum Resistance Metrology*, *Chinese Phys. Lett.* **40**, 107201 (2023).
- [163] E. H. Hwang, S. Adam, and S. Das Sarma, *Transport in Chemically Doped Graphene in the Presence of Adsorbed Molecules*, *Phys. Rev. B - Condens. Matter Mater. Phys.* **76**, 1 (2007).
- [164] E. H. Hwang, S. Adam, and S. Das Sarma, *Carrier Transport in Two-Dimensional Graphene Layers*, *Phys. Rev. Lett.* **98**, 2 (2007).
- [165] D. Vaquero et al., *Phonon-Mediated Room-Temperature Quantum Hall Transport in Graphene*, *Nat. Commun.* **14**, 318 (2023).
- [166] A. M. Alexeev, R. R. Hartmann, and M. E. Portnoi, *Two-Phonon Scattering in Graphene in the Quantum Hall Regime*, *Phys. Rev. B - Condens. Matter Mater. Phys.* **92**, 195431 (2015).
- [167] S. Sarma and A. Pinczuk, *Perspectives in Quantum Hall Effects: Novel Quantum Liquids in Low-Dimensional Semiconductor Structures* (1997).
- [168] W. Poirier and F. Schopfer, *Resistance Metrology Based on the Quantum Hall Effect*, *Eur. Phys. J. Spec. Top.* **172**, 207 (2009).
- [169] T. J. B. M. Janssen, A. Tzalenchuk, R. Yakimova, S. Kubatkin, S. Lara-Avila, S. V. Kopylov, and V. I. Fal'Ko, *Anomalously Strong Pinning of the Filling Factor $\nu=2$ in Epitaxial Graphene*, *Phys. Rev. B - Condens. Matter Mater. Phys.* **83**, 233402 (2011).
- [170] M. Furlan, *Electronic Transport and the Localization Length in the Quantum Hall Effect*, *Phys. Rev. B* **57**, 14818 (1998).
- [171] T. J. B. M. Janssen, S. Rozhko, I. Antonov, A. Tzalenchuk, J. M. Williams, Z. Melhem, H. He, S. Lara-Avila, S. Kubatkin, and R. Yakimova, *Operation of Graphene Quantum*

-
- Hall Resistance Standard in a Cryogen-Free Table-Top System*, 2D Mater. **2**, 035015 (2015).
- [172] E. A. Mironov, A. V. Voitovich, and O. V. Palashov, *Permanent-Magnet Faraday Isolator with the Field Intensity of More than 3 Tesla*, Laser Phys. Lett. **17**, 015001 (2020).
- [173] Zheng Wang, Wen Hui Yang, Xiao Bing Zhang, Li Li Hu, Hui Xian Wang, and Yu Xia Zhang, *Design and Manufacture of a Near 3 T High Field Permanent Magnet Assembly*, IEEE Trans. Appl. Supercond. **22**, 4302304 (2012).
- [174] F. Bloch, O. Cugat, G. Meunier, and J. C. Toussaint, *Innovating Approaches to the Generation of Intense Magnetic Fields: Design and Optimization of a 4 Tesla Permanent Magnet Flux Source*, IEEE Trans. Magn. **34**, 2465 (1998).
- [175] D. Momeni Pakdehi et al., *Silicon Carbide Stacking-Order-Induced Doping Variation in Epitaxial Graphene*, Adv. Funct. Mater. **30**, 1 (2020).
- [176] C. Jiang, L. Chen, H. Wang, C. Chen, X. Wang, Z. Kong, Y. Wang, H. Wang, and X. Xie, *Increasing Coverage of Mono-Layer Graphene Grown on Hexagonal Boron Nitride*, Nanotechnology **34**, 165601 (2023).
- [177] F. Speck, J. Jobst, F. Fromm, M. Ostler, D. Waldmann, M. Hundhausen, H. B. Weber, and T. Seyller, *The Quasi-Free-Standing Nature of Graphene on H-Saturated SiC(0001)*, Appl. Phys. Lett. **99**, 122106 (2011).
- [178] F. W. Hehl, Y. N. Obukhov, and B. Rosenow, *Is the Quantum Hall Effect Influenced by the Gravitational Field?*, Phys. Rev. Lett. **93**, 096804 (2004).
- [179] A. A. Penin, *Quantum Hall Effect in Quantum Electrodynamics*, Phys. Rev. B **79**, 113303 (2009).
- [180] D. K. Patel et al., *Zero External Magnetic Field Quantum Standard of Resistance at the 10^{-9} Level*, arXiv:2410.13365, (2024).
- [181] Q. Li, E. H. Hwang, and S. Das Sarma, *Disorder-Induced Temperature-Dependent Transport in Graphene: Puddles, Impurities, Activation, and Diffusion*, Phys. Rev. B - Condens. Matter Mater. Phys. **84**, (2011).
- [182] S. Lara-Avila, A. Tzalenchuk, S. Kubatkin, R. Yakimova, T. J. B. M. Janssen, K. Cedergren, T. Bergsten, and V. Fal'ko, *Disordered Fermi Liquid in Epitaxial Graphene*

from Quantum Transport Measurements, Phys. Rev. Lett. **107**, 166602 (2011).

Curriculum vitae

2019 – 2024 Physikalisch-Technische Bundesanstalt, Braunschweig, Germany
Leibniz University Hannover, Hannover, Germany
Ph.D. Candidate

2017 – 2019 Paul-Drude-Institute, Berlin, Germany

2013 – 2016 Fudan University, Shanghai, China
Master of Science, Condensed Matter Physics, Department of Physics

2009 – 2013 Shanghai University, Shanghai, China
Bachelor of Engineering, Microelectronics, Department of Physics

List of Publications

The thesis is based on the work contained in the following publications.

1. **Y. Yin**, M. Kruskopf, S. Bauer, T. Tschirner, K. Pierz, F. Hohls, R. J. Haug, and H. W. Schumacher, Quantum Hall resistance standards based on epitaxial graphene with p -type conductivity, *Appl. Phys. Lett.*, 125, 064001 (2024)
2. **Y. Yin**, M. Kruskopf, A. Chatterjee, S. Bauer, T. Tschirner, M. Götz, F. Hohls, K. Pierz, and H. W. Schumacher, Quantum Hall Resistance Standards Based on Epitaxial Graphene with Different Doping Layer Sequence, *2024 Conference on Precision Electromagnetic Measurements (CPEM)*, Denver, CO, USA, pp. 1-2, (2024), doi: 10.1109/CPEM61406.2024.10646126.
3. **Y. Yin**, A. Chatterjee, D. Momeni, M. Kruskopf, M. Götz, S. Wundrack, F. Hohls, K. Pierz, and H. W. Schumacher, Tailoring permanent charge carrier densities in epitaxial Graphene on SiC by functionalization with F4-TCNQ, *Adv. Physics Res.* 1, 2200015 (2022)
4. **Y. Yin**, M. Kruskopf, P. Gournay, B. Rolland, M. Götz, E. Pesel, T. Tschirner, D. Momeni, A. Chatterjee, F. Hohls, K. Pierz, H. Scherer, R. J. Haug, and H. W. Schumacher, Graphene quantum Hall resistance standard for realizing the unit of resistance under relaxed experimental conditions, *Phys. Rev. Applied*, 2024 (accepted)

Other publications

5. F. Overney, A. L. Eichenberger, S. Bauer, M. Ortolano, M. Marzano, **Y. Yin**, and M. Kruskopf, Longitudinal Impedance Measurements on Graphene QHE Devices, *2024 Conference on Precision Electromagnetic Measurements (CPEM)*, Denver, CO, USA, pp. 1-2, (2024), doi: 10.1109/CPEM61406.2024.10645982
6. Chatterjee, M. Kruskopf, M. Götz, **Y. Yin**, E. Pesel, P. Gournay, B. Rolland, J. Kucera, S. Bauer, K. Pierz, B. Schumacher, and H. Scherer, Performance and Stability Assessment of Graphene-Based Quantum Hall Devices for Resistance Metrology, *IEEE Transactions on Instrumentation and Measurement*, 72, pp.1-6, 1502206 (2023)
7. M. Marzano, Y. Pimsut, M. Kruskopf, **Y. Yin**, M. Kraus, M. Ortolano, S. Bauer, R. Behr, L. Callegaro, Mutual validation of PTB's Josephson and INRIM-POLITO's

- electronic impedance bridges for the realization of the farad from graphene quantum standards, *25th IMEKO TC4 Symposium and 23rd International Workshop on ADC and DAC Modelling and Testing (IWADC)*, Brescia, Italy, 12 – 14, September 2022, doi: 10.21014/tc4-2022.44
8. M. Marzano, Y. Pimsut, M. Kruskopf, **Y. Yin**, M. Kraus, V. D'Elia, L. Callegaro, M. Ortolano, S. Bauer, and R. Behr, PTB–INRIM comparison of novel digital impedance bridges with graphene impedance quantum standards, *Metrologia* 59, 065001 (2022)
 9. D.-H. Chae, M. Kruskopf, J. Kucera, J. Park, N. T. M. Tran, D. B. Kim, K. Pierz, M. Götz, **Y. Yin**, P. Svoboda, P. Chrobok, F. Couëdo, and F. Schopfer, Investigation of the stability of graphene devices for quantum resistance metrology at direct and alternating current, *Meas. Sci. Technol.* 33, 065012 (2022)
 10. M. Kruskopf, D. K. Patel, C. I Liu, A. F. Rigosi, R. E. Elmquist, Y. Wang, S. Bauer, **Y. Yin**, K. Pierz, E. Pesel, M. Götz, J. Schurr, Graphene quantum Hall effect devices for AC and DC resistance metrology, *2020 Conference on Precision Electromagnetic Measurements (CPEM)*, Denver, CO, USA, 2020, pp. 1-2, doi: 10.1109/CPEM49742.2020.9191851.
 11. L. Callegaro, V. D'Elia, M. Marzano, N. T. M. Tran, M. Ortolano, J. Kucera, K. Pierz, S. Bauer, M. Kruskopf, **Y. Yin**, Y. Pimsut, F. Schopfer, O. Thevenot, B. Jeanneret, F. Overney, T. Bergsten, K. Cedergren, A. Manninen, J. Nissilä, A. Michon, S. Sawatdiaree, D.-H. Chae, The EMPIR Project GIQS: Graphene Impedance Quantum Standard, *2020 Conference on Precision Electromagnetic Measurements (CPEM)*, Denver, CO, USA, 2020, pp. 1-2, doi: 10.1109/CPEM49742.2020.9191743.
 12. **Y. Yin**, M. Kruskopf, O. Zheliuk, A. Chatterjee, M. Götz, F. Hohls, K. Pierz, U. Zeitler, R. J. Haug, and H. W. Schumacher, Phonon-mediated quantum Hall effect in epitaxial graphene, in preparation, (2024)
 13. **Y. Yin**, M. Kruskopf, O. Zheliuk, A. Chatterjee, M. Götz, F. Hohls, K. Pierz, U. Zeitler, R. J. Haug, and H. W. Schumacher, Breakdown of the strong Fermi-level pinning at filling factor $\nu = 2$ in n- and p-type molecularly doped monolayer epitaxial graphene, in preparation, (2024)

Acknowledgment

I would like to express my sincerest gratitude to all those who have helped/supported me throughout my studies and made this thesis possible. Without all of you, I would not have been able to achieve anything worthwhile in my studies.

I would like to express my deepest gratitude to Dr. Klaus Pierz, PD Dr. Frank Hohls, and PD Dr. Hans Werner Schumacher for offering me an excellent Ph.D. position on quantum resistance standards before I joined the PTB. I am grateful for this opportunity to continue my academic career in the fascinating world of quantum physics. While working at the Department of Semiconductor Physics and Magnetism, all of you always fully supported my research on experiment facility, knowledge, finance, and academic networking. When I have any new ideas for my research, you promptly provide me with internal and external academic resources to demonstrate my ideas. When I had questions, requests, or different viewpoints in my research, I received prompt answers, feedback, comments, and suggestions from you. This dissertation would not have been possible without unconditional support from you. It was truly a wonderful time to study my Ph.D. in the working group of Low-dimensional Electron Systems.

I would like to express my deepest appreciation to my supervisors, PD Dr. Hans Werner Schumacher and Prof. Dr. Rolf J. Haug for invaluable guidance and unwavering support throughout these years of academic research at the PTB and the Leibniz University Hannover. PD Dr. Hans Werner Schumacher, thank you for your guidance and for sharing your vision throughout my years at the PTB. Prof. Dr. Rolf J. Haug, your enthusiasm and patience in teaching students, your rigorous attitude towards research, your immense knowledge of all aspects of physics, and your passion for passing it on have always encouraged me to become a better academic and person. I am also extremely grateful to PD Dr. Uwe Siegner for supporting the projects and my position at the PTB.

I would like to express my gratitude to my mentor, Dr. Klaus Pierz, for always having an open door, his continuous support, the invaluable discussions we had, and his patience throughout my years at the PTB. I gained in-depth knowledge of graphene and material growth skills from you. You not only guided me in research at PTB but also took care of me in life in Germany. I would like to express my gratitude to PD Dr. Frank Hohls for always being enthusiastic when I discuss nanophysics with him. Your knowledge of physics has been an inspiration to me, and your passion for science has been a motivation to me.

The fruitful results of this dissertation benefited from the substantial, close, and harmonious collaborations between the departments of 2.5 and 2.6 at the PTB. The team in the department of 2.6 established one of the best advanced high-accuracy measurement facilities for quantum electrical unit metrology in the world. The high-accuracy measurements in this thesis were conducted in the department of 2.6. I appreciate the solid support and endless help from colleagues in the department of 2.6. Special thanks to PD Dr. Hansjörg Scherer, Dr. Mattias Kruskopf, Dr. Martin Götz, and Eckart Pesel for creating an inspiring and friendly working environment and providing invaluable technical support. It has been a great honor to work closely with all of you, and I am truly fortunate to have had the opportunity to learn metrological knowledge from all of you. Many thanks to Susanne Gruber and Eckart Pesel for their patience and dedication in repairing and maintaining the electronics setups for the high-accuracy measurements, and for manufacturing all the chip carriers used for the QHR devices. I would not have been able to run my experiment smoothly without support from Michael Busse, Torsten Stöcker, and Niklas Abraham with liquid helium supply. Many thanks to their professional management and efficient coordination, which ensured we always received sufficient liquid helium on time. In the past few years, I have heard from many universities and institutes that they were struggling with the shortage of liquid helium for their experiments. We have been fortunate at the PTB to have a reliable liquid helium supply for our experiments.

I would like to extend my gratitude to my amazing colleagues at the PTB for their invaluable expertise, support, and collaboration. I would like to thank Stefan Wundrack for his excellent work on DFT simulation, Raman, and AFM measurements and for his enthusiasm and dedication. I greatly enjoyed discussing and learning about surface science and physics with you. I am grateful for the excellent support I received from the working group of Nanostructuring and Clean Room Center Infrastructure, led by Dr. Thomas Weimann. I would like to thank Dr. Thomas Weimann, Cristiano Cognolato, Kathrin Störr, Bert Egeling, Rolf Gerdau, Judith Felgner, and Peter Hinze for their help and support in the cleanroom. I am grateful to our cleanroom team for their support whenever I have questions or requirements. I would like to thank Thorsten Dziomba and Andre Felgner for always being flexible whenever the confocal microscopy was needed. It was a great time working with all of you.

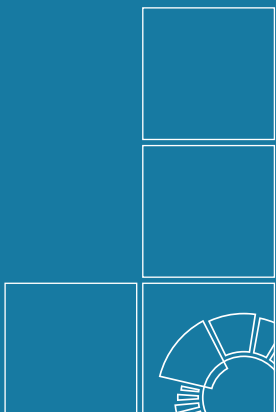
I am grateful for all the colleagues at the department of 2.5. I would like to express my gratitude to Holger Marx for maintaining and repairing the cryogenic setup and growth furnace in Department 2.5. Your contributions have been invaluable, ensuring that our experiment setups run smoothly and efficiently in our laboratory. Special thanks go to Dr. Marcelo Jaime for the invaluable comments, suggestions, and discussions on my paper and dissertation. Many thanks

to Manfred Kitschke for the help in the workshop. Many thanks to the software experts Victor Rogala and Dr. Jinni Lee for their help in identifying and resolving the bugs and problems in the Modulab system. I would like to express my gratitude to Dr. Davood Momeni, Dr. Atasi Chatterjee, Dr. Teresa Marie Tschirner, and Julia Guse for the support to graphene growth, device fabrication, transport measurement, and endless discussions on scientific questions. I would also like to thank Dr. Alexander Fernández Scarioni for the help on the Vector cryostat. It was a great time working with all of you.

I am deeply indebted to my collaborators for their help, support, and important contributions. This dissertation would not have been possible without my collaborators over the past years. Special thanks go to Dr. Pierre Gournay and Benjamin Rolland from the BIPM, France. They spend a lot of effort performing high-accuracy measurements from our graphene QHR standards and verifying the high performance of our devices at the BIPM. We work together to promote the transition from GaAs- to graphene-based QHR standards, and to shape the future of QHR standards. I would like to extend my gratitude to Prof. Dr. Uli Zeitler and Dr. Oleksandr Zheliuk from the High Field Magnet Laboratory, Radboud University, the Netherlands. They kindly offered me the opportunity to measure our graphene devices in the high magnetic field facility in Nijmegen. Over the course of many long hours spent doing measurements day and night, we obtained a wealth of interesting results from epitaxial graphene in high magnetic fields.

I greatly acknowledge the funding and foundation that supported this dissertation. Thanks to the Heidenhain Foundation for their financial support, which made it possible for me to attend the international conference. This work was supported by the joint Research Project GIQS (18SIB07). This work received funding from the European Metrology Programme for Innovation and Research co-financed by the Participating States and from the European Union's Horizon 2020 research and innovation program. This work was supported by the Deutsche Forschungsgemeinschaft Project Te386/21-1 and Pi385/3-1 within the Research Unit FOR5242. The work was also co-funded by the Deutsche Forschungsgemeinschaft under Germany's Excellence Strategy – EXC-2123 Quantum Frontiers (390837967).

My final thanks go to my parents for their unwavering support and encouragement throughout my journey, for their unconditional love, and for millions of other things. Thank you for always believing in me and supporting me in my decisions, even when it meant living thousands of kilometers away.



Herausgeber:

Physikalisch-Technische Bundesanstalt

ISNI: 0000 0001 2186 1887

Presse und Öffentlichkeitsarbeit

Bundesallee 100

38116 Braunschweig

Telefon: (05 31) 592-93 21

Telefax: (05 31) 592-92 92

www.ptb.de